

AD-A166 414

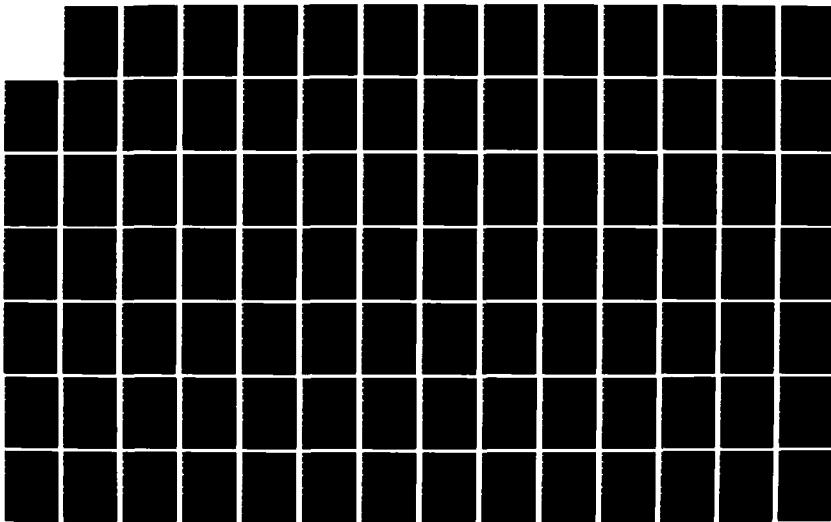
TRANSFER COEFFICIENT MEASUREMENT STUDY(U) MICHIGAN UNIV
ANN ARBOR RADIATION LAB V V LIEPA 19 FEB 85 016303-1-F
DNA-TR-85-70 DNA001-78-C-0361

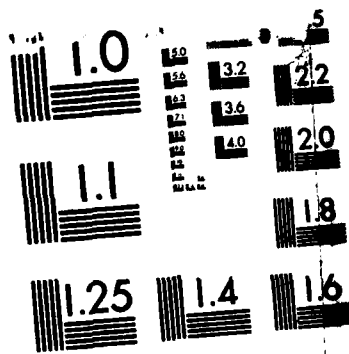
1/2

UNCLASSIFIED

F/G 20/14

NL





MICROCOPY RESOLUTION TEST CHART
NATIONAL BUREAU OF STANDARDS-1963-A

12

AD-A166 414

DNA-TR-85-70

TRANSFER COEFFICIENT MEASUREMENT STUDY

**Valdis V. Liepa
The University of Michigan
Research Security Office
Division, Research & Development
West Engineering Building, Room 247B
550 E. University Avenue
Ann Arbor, MI 48109-1092**

19 February 1985

Technical Report

CONTRACT No. DNA 001-78-C-0361

**Approved for public release;
distribution is unlimited.**

**THIS WORK WAS SPONSORED BY THE DEFENSE NUCLEAR AGENCY
UNDER RDT&E RMSS CODE B323078464 R99QAXEB20238 H2590D.**

**Prepared for
Director
DEFENSE NUCLEAR AGENCY
Washington, DC 20305-1000**

**DTIC
ELECTE
APR 10 1986
S D
E**

DTIC FILE COPY

Destroy this report when it is no longer needed. Do not return to sender.

PLEASE NOTIFY THE DEFENSE NUCLEAR AGENCY,
ATTN: STTI, WASHINGTON, DC 20305-1000, IF YOUR
ADDRESS IS INCORRECT, IF YOU WISH IT DELETED
FROM THE DISTRIBUTION LIST, OR IF THE ADDRESSEE
IS NO LONGER EMPLOYED BY YOUR ORGANIZATION.



UNCLASSIFIED

SECURITY CLASSIFICATION OF THIS PAGE

AD-A166414

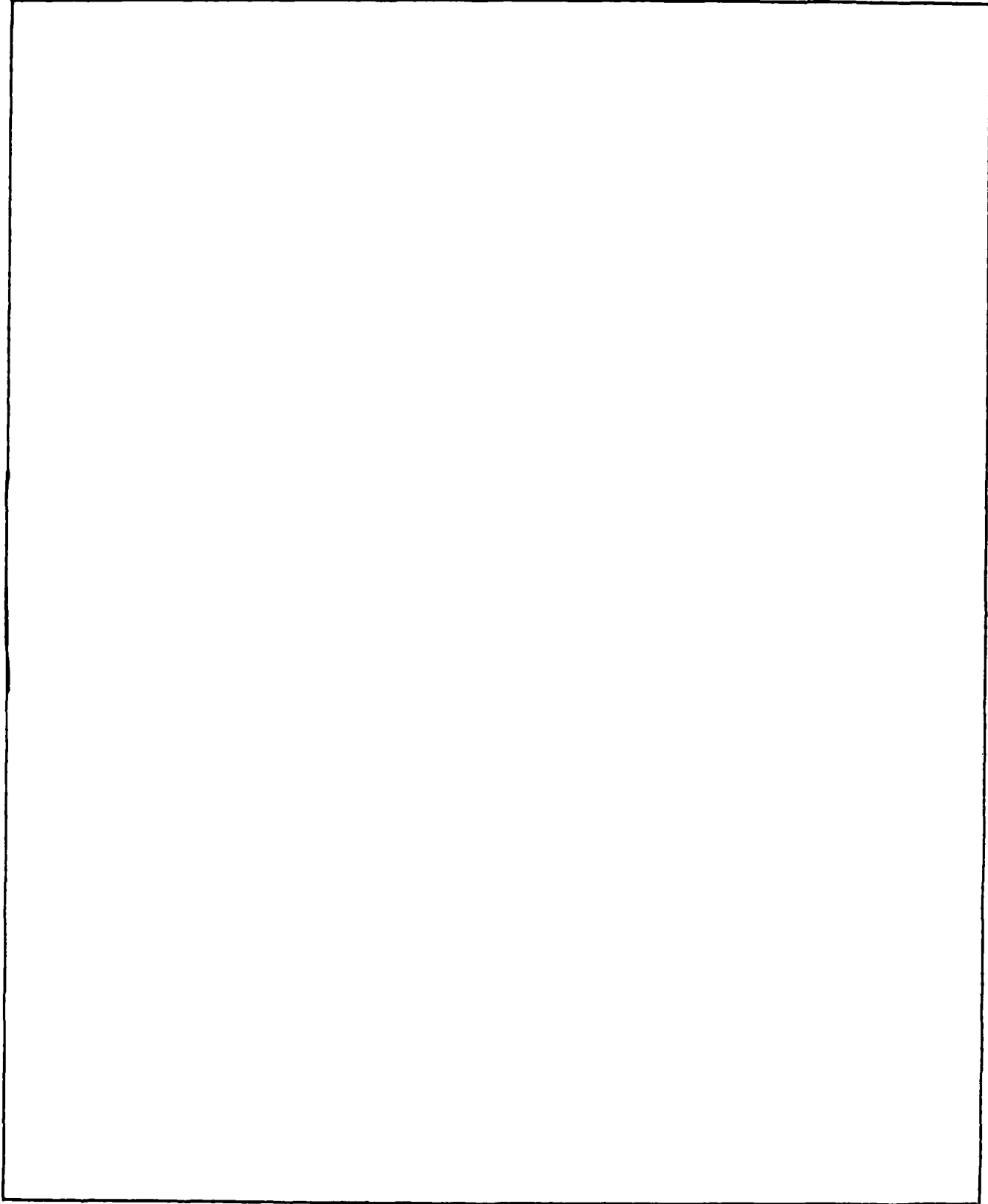
Form Approved
OMB No. 0704-0188
Exp. Date: Jun 30, 1986

REPORT DOCUMENTATION PAGE

1a. REPORT SECURITY CLASSIFICATION UNCLASSIFIED		1b. RESTRICTIVE MARKINGS	
2a. SECURITY CLASSIFICATION AUTHORITY N/A since Unclassified		3. DISTRIBUTION/AVAILABILITY OF REPORT Approved for public release; distribution is unlimited.	
2b. DECLASSIFICATION/DOWNGRADING SCHEDULE N/A since Unclassified			
4. PERFORMING ORGANIZATION REPORT NUMBER(S) 016303-1-F		5. MONITORING ORGANIZATION REPORT NUMBER(S) DNA-TR-85-70	
6a. NAME OF PERFORMING ORGANIZATION The University of Michigan Research Security Office Div. Research & Development	6b. OFFICE SYMBOL (if applicable) Rad. Lab.	7a. NAME OF MONITORING ORGANIZATION Director Defense Nuclear Agency	
6c. ADDRESS (City, State, and ZIP Code) West Engineering Bldg. Room 247B 550 E. University Ave Ann Arbor, MI 48109-1092		7b. ADDRESS (City, State, and ZIP Code) Washington, DC 20305-1000	
8a. NAME OF FUNDING / SPONSORING ORGANIZATION	8b. OFFICE SYMBOL (if applicable)	9. PROCUREMENT INSTRUMENT IDENTIFICATION NUMBER DNA 001-78-C-0361	
8c. ADDRESS (City, State, and ZIP Code)		10. SOURCE OF FUNDING NUMBERS	
		PROGRAM ELEMENT NO. 62715H	PROJECT NO. R99QAXE
		TASK NO. B	WORK UNIT ACCESSION NO. DH003877
11. TITLE (Include Security Classification) TRANSFER COEFFICIENT MEASUREMENT STUDY			
12. PERSONAL AUTHOR(S) Valdis V. Liepa			
13a. TYPE OF REPORT Technical Report	13b. TIME COVERED FROM 780701 TO 781231	14. DATE OF REPORT (Year, Month, Day) 850219	15. PAGE COUNT 106
16. SUPPLEMENTARY NOTATION This work was sponsored by the Defense Nuclear Agency under RDT&E RMSS Code B323078464 R99QAXEB20238 H2590D.			
17. COSATI CODES		18. SUBJECT TERMS (Continue on reverse if necessary and identify by block number)	
FIELD 20	GROUP 14	Transfer Coefficients, EMP Interaction Surface Field Measurements, Experimental Study	
19. ABSTRACT (Continue on reverse if necessary and identify by block number) This report presents an experimental study that was initiated to verify transfer coefficient concepts proposed by Maurice I. Sancer of R&D Associates who postulated that voltages and currents inside a body can be related to exterior surface currents and charges when the apertures are shorted. A cylindrical model was selected with cylindrical interior cavity and a wire stretched along its axis. Interior (voltage) and exterior (field) measurements were performed for the cylinder near a perfectly conducting ground plane to demonstrate the transfer coefficient dependence on the environment. Measurements were made in the frequency domain of 118 to 4400 MHz. Keywords: <i>increase in the pub e interaction</i>			
20. DISTRIBUTION/AVAILABILITY OF ABSTRACT <input type="checkbox"/> UNCLASSIFIED/UNLIMITED <input checked="" type="checkbox"/> SAME AS RPT. <input type="checkbox"/> DTIC USERS		21. ABSTRACT SECURITY CLASSIFICATION UNCLASSIFIED	
22a. NAME OF RESPONSIBLE INDIVIDUAL Betty L. Fox		22b. TELEPHONE (Include Area Code) (202)325-7042	22c. OFFICE SYMBOL DNA/STI

UNCLASSIFIED

SECURITY CLASSIFICATION OF THIS PAGE



UNCLASSIFIED

SECURITY CLASSIFICATION OF THIS PAGE

Table 1. Conversion factors for U.S. customary to metric (SI) units of measurement.

To Convert From	To	Multiply By
angstrom	meters (m)	1.000 000 X E -10
atmosphere (normal)	kilo pascal (kPa)	1.013 25 X E +2
bar	kilo pascal (kPa)	1.000 000 X E +2
barn	meter ² (m ²)	1.000 000 X E -28
British thermal unit (thermochemical)	joule (J)	1.054 350 X E +3
calorie (thermochemical)	joule (J)	4.184 000
cal (thermochemical)/cm ²	mega joule/m ² (MJ/m ²)	4.184 000 X E -2
curie	*giga becquerel (GBq)	3.700 000 X E +1
degree (angle)	radian (rad)	1.745 329 X E -2
degree Fahrenheit	degree kelvin (K)	$t_K = (t_F + 459.67)/1.8$
electron volt	joule (J)	1.602 19 X E -19
erg	joule (J)	1.000 000 X E -7
erg/second	watt (W)	1.000 000 X E -7
foot	meter (m)	3.048 000 X E -1
foot-pound-force	joule (J)	1.355 818
gallon (U. S. liquid)	meter ³ (m ³)	3.785 412 X E -3
inch	meter (m)	2.540 000 X E -2
jerk	joule (J)	1.000 000 X E +9
joule/kilogram (J/kg) (radiation dose absorbed)	Gray (Gy)	1.000 000
kilotons	terajoules	4.183
kip (1000 lbf)	newton (N)	4.448 222 X E +3
kip/inch ² (ksi)	kilo pascal (kPa)	6.894 757 X E +3
ktap	newton-second/m ² (N-s/m ²)	1.000 000 X E +2
micron	meter (m)	1.000 000 X E -6
mil	meter (m)	2.540 000 X E -5
mile (international)	meter (m)	1.609 344 X E +3
ounce	kilogram (kg)	2.834 952 X E -2
pound-force (lbs avoirdupois)	newton (N)	4.448 222
pound-force inch	newton-meter (N·m)	1.129 848 X E -1
pound-force/inch	newton/meter (N/m)	1.751 268 X E +2
pound-force/foot ²	kilo pascal (kPa)	4.788 026 X E -2
pound-force/inch ² (psi)	kilo pascal (kPa)	6.894 757
pound-mass (lbm avoirdupois)	kilogram (kg)	4.535 924 X E -1
pound-mass-foot ² (moment of inertia)	kilogram-meter ² (kg·m ²)	4.214 011 X E -2
pound-mass/foot ³	kilogram/meter ³ (kg/m ³)	1.601 846 X E +1
rad (radiation dose absorbed)	**Gray (Gy)	1.000 000 X E -2
roentgen	coulomb/kilogram (C/kg)	2.579 760 X E -4
shake	second (s)	1.000 000 X E -8
slug	kilogram (kg)	1.459 390 X E +1
torr (mm Hg, 0° C)	kilo pascal (kPa)	1.333 22 X E -1

*The becquerel (Bq) is the SI unit of radioactivity; 1 Bq = 1 event/s.

**The Gray (Gy) is the SI unit of absorbed radiation.

A more complete listing of conversions may be found in "Metric Practice Guide E 380-74," American Society for Testing and Materials.

PREFACE

Many students from the Radiation Laboratory contributed to this program both in experimental and theoretical phases. Special thanks go to Jeff Travis, who helped to modify the instrumentation and rewrite the software, to Ivan LaHaie who interfaced the instrumentation computer with the University's main facility (and a few times crashed them both), and to Hyun Yoon who made many of the tedious measurements.

Special appreciation goes also to Maurice Sancer for helping to design the experiments that relate to real situations, and to Mrs. Wanita Rasey for typing the manuscript.

Accession For	
NTIS GRA&I	<input checked="" type="checkbox"/>
DTIC TAB	<input type="checkbox"/>
Unannounced	<input type="checkbox"/>
Justification	
By	
Distribution/	
Availability Codes	
Dist	Avail and/or Special
A-1	



TABLE OF CONTENTS

	<u>Page</u>
Metric Conversion Table	1
Preface	2
List of Illustrations	4
List of Tables	6
Section 1. Introduction	7
2. Description of the Experimental Facility	12
3. Preliminary Measurements of EM Coupling into a Cylindrical Conducting Cavity Through a Circular Aperture	16
4. Test Model, Measurements, and Data	27
4.1 The Model	27
4.2 Measurements	31
4.3 Data	31
5. Cylinders Near the Ground Plane	43
5.1 Ground Plane	43
5.2 The Model	45
5.3 Experimental Arrangement	48
5.4 Measurements	51
6. Data	53
7. Some Afterthoughts	82
List of References	83
Appendix. Estimating the Junction Capacitance Between Two Coaxial Cables	85

LIST OF ILLUSTRATIONS

<u>Figure</u>	<u>Page</u>
2.1	13
3.1(a)	17
3.1(b)	17
3.1(c)	17
3.2(a)	19
3.2(b)	20
3.2(c)	21
3.2(d)	22
3.3	24
3.4(a)	25
3.4(b)	26
4.1	28
4.2(a)	29
4.2(b)	30
4.3	32
4.4	35
4.5	36
4.6	37
4.7	38

<u>Figure</u>		<u>Page</u>
4.8	Interior voltage, E-pol, $\phi = 0^\circ$.	39
4.9	Interior voltage, E-pol, $\phi = 90^\circ$.	40
4.10	Interior voltage, H-pol, $\phi = 90^\circ$.	41
5.1	Resistively loaded ground plane used in the measurements.	46
5.2	Pertinent dimensions of the second model.	47
5.3	Block diagram of the facility.	49
5.4	Schematic view of the experimental setup. (Insert shows the interior polarity.)	50
6.1	Surface field measurement at $\phi = 0^\circ$, $D = 1.5$ A.	55
6.2	Surface field measurement at $\phi = 0^\circ$, $D = 2.0$ A.	56
6.3	Surface field measurement at $\phi = 0^\circ$, $D = 5.0$ A.	57
6.4	Surface field measurement at $\phi = 90^\circ$, $D = 1.5$ A.	58
6.5	Surface field measurement at $\phi = 90^\circ$, $D = 2.0$ A.	59
6.6	Surface field measurement at $\phi = 90^\circ$, $D = 5.0$ A.	60
6.7	Surface field measurement at $\phi = 180^\circ$, $D = 1.5$ A.	61
6.8	Surface field measurement at $\phi = 180^\circ$, $D = 2.0$ A.	62
6.9	Surface field measurement at $\phi = 180^\circ$, $D = 5.0$ A.	63
6.10	Interior coupled-field measurement at $\phi = 0^\circ$, $D = 1.5$ A.	64
6.11	Interior coupled-field measurement at $\phi = 0^\circ$, $D = 2.0$ A.	65
6.12	Interior coupled-field measurement at $\phi = 0^\circ$, $D = 5.0$ A.	66
6.13	Interior coupled-field measurement at $\phi = 90^\circ$, $D = 1.5$ A.	67
6.14	Interior coupled-field measurement at $\phi = 90^\circ$, $D = 2.0$ A.	68
6.15	Interior coupled-field measurement at $\phi = 90^\circ$, $D = 5.0$ A.	69
6.16	Interior coupled-field measurement at $\phi = 180^\circ$, $D = 1.5$ A.	70
6.17	Interior coupled-field measurement at $\phi = 180^\circ$, $D = 2.0$ A.	71
6.18	Interior coupled-field measurement at $\phi = 180^\circ$, $D = 5.0$ A.	72

<u>Figure</u>		<u>Page</u>
6.19	Transfer coefficients for $\phi = 0^\circ$, $D = 1.5$ A.	73
6.20	Transfer coefficients for $\phi = 0^\circ$; $D = 2.0$ A.	74
6.21	Transfer coefficients for $\phi = 0^\circ$, $D = 5.0$ A.	75
6.22	Transfer coefficients for $\phi = 90^\circ$, $D = 1.5$ A.	76
6.23	Transfer coefficients for $\phi = 90^\circ$, $D = 2.0$ A.	77
6.24	Transfer coefficients for $\phi = 90^\circ$, $D = 5.0$ A.	78
6.25	Transfer coefficients for $\phi = 180^\circ$, $D = 1.5$ A.	79
6.26	Transfer coefficients for $\phi = 180^\circ$, $D = 2.0$ A.	80
6.27	Transfer coefficients for $\phi = 180^\circ$, $D = 5.0$ A.	81
A-1	Parallelepiped section.	85
A-2	Semicircular cylindrical sections.	86
A-3	Spherical quadrant sections.	87
A-4	Spherical shell sections.	88
A-5	Rectangular toroid sector.	89
A-6	Special cases of rectangular toroid.	90
A-7	Junction of dissimilar radii, $a > b$.	91
A-8	Junction of dissimilar radii, $a < b$.	94

LIST OF TABLES

<u>Table</u>		<u>Page</u>
4.1	Parallel polarization data.	33
4.2	Perpendicular polarization data.	34
6.1	Data matrix.	54

SECTION 1

INTRODUCTION

The objective of this study was to design and carry out an experimental program to determine source-independent transfer coefficients relating an external electromagnetic field to the voltages and currents inside a system when in a simulated EMP environment.

The vast majority, if not all, of the EMP coupling analyses pertaining to systems that are basically metallic enclosures (i.e., aircraft, missiles, ships, and tanks) have included the calculation of external coupling quantities (surface current and charge densities). It has always been a general underlying belief that these quantities could be used to determine voltages and currents driving critical subsystems contained within the enclosure.

Explicit demonstrations of the relationship between internal voltages and currents and external coupling quantities are contained in the works of Latham [1] and Lee and Baum [2]. These works are directed toward obtaining the voltages and currents associated only with a TEM mode excited within a simple enclosure. These works depend on small aperture assumptions as well as a knowledge of electric and magnetic polarizabilities associated with the apertures. The work of Tesche [3] also depends on small aperture assumptions and a knowledge of aperture polarizabilities in order to relate external coupling quantities to internal quantities. His work is of a more general nature than the previously cited works in that he allows both the

external and internal geometry to be quite complex; however, his work contains no explicit procedure or results. The least restrictive work related to transfer coefficients is contained in a relatively recent report by Baum [4]. Baum allows the more general concept of aperture to include apertures associated with antennas and he also eliminates the requirement that aperture polarizabilities be known. He lists the following assumptions for the validity of his approach:

- (a) Electrically and physically small apertures.
- (b) No significant interaction between penetrators.
- (c) Independent contributions from the different external coupling quantities at a given penetrator.

Baum's work was directed toward developing extrapolation techniques for interpreting the results of tests in EMP simulators in terms of EMP criteria. For that application, it is essential that the dependence of the transfer coefficients on the complete exterior system environment be appropriately accounted for. His "penetration extrapolation" can be related to somewhat remote radiating simulators, but not to proximate bounded wave simulators. The compensation for simulator/test object interactions requires two sets of transfer coefficients.

The new transfer coefficient theory advocated by Sancer [5] differs from Baum's theory in the elimination of the first two assumptions. The elimination of these assumptions requires experimental measurements which are the subject of this study.

To prove (or disprove) this theory an experimental program was designed to measure transfer coefficients relating the external electromagnetic field quantities to voltages and currents inside a relatively

simple cavity. The model studied was a cylinder of finite length having either hemispherical end caps or flat end plates. The interior of the structure was a cylindrical cavity with a single wire running through the center, shorted at one end and terminated in 50 ohms at the other. The excitation of the interior is through a small hole in the side of the cavity.

For the case of a cylindrical model with a single aperture, as the case studied here, the voltage V_R induced in the interior is written as

$$V_R = T_z J_z + T_\phi J_\phi + T_n E_n \quad (1)$$

where J_z = the longitudinal component of current density induced by the exterior source on a metallic seal placed over the aperture,

J_ϕ = the circumferential component of current density induced by the exterior source on a metallic seal placed over the aperture,

E_n = the normal component of electric field induced by the exterior source on a metallic seal placed over the aperture.

The coefficients T_z, T_ϕ and T_n are so-called transfer coefficients to be determined. All quantities in Eq. (1) are functions of frequency.

To make these measurements the facility and procedures developed and used for measurements of external electromagnetic fields induced by plane electromagnetic waves on scale model aircraft such as the F-111, F-14A, F-16A etc [6] were adapted. This is a sweep frequency measurement facility that provides a plane-wave incident source and measures amplitude and phase of given circuit response. The coverage is 118 to 4400 MHz.

Section 2 of this report describes the facility in more detail. Section 3 describes some of the preliminary studies that were carried out to get a "feel" for the problem and obtain the design criterion for the cylindrical model such as the size of the model, the size of the coupling hole, etc.).

There were two basic experimental studies carried out. In the first one the measurements were performed on the cylinder in free space with the coupling aperture located at one quarter distance from one end of the cylinder. In such a case all three field quantities (c.f. Eq. (1)) are present at the (shorted) aperture and hence sufficient data were taken to determine the three transfer coefficients T_z , T_ϕ and T_n . The model, the measurements, and data are presented in Section 4.

In the other study a situation was selected to demonstrate the transfer coefficient dependence on the exterior environment. The experiment consisted of the cylinder in front of a metallic ground plane. The aperture this time was cut at the center of the cylinder and the cylinder was excited with E^{inc} parallel to the axis. In such a case Eq. (1) reduces to

$$V_R = T_z J_z, \quad (2)$$

and only one coefficient T_z needs to be determined. However, the T_z is now also dependent on the ground plane spacing from the cylinder. This study and the results are presented in Sections 5 and 6.

All the measured data was also forwarded to R&D Associates and their analysis of the data have been reported in [5].

The appendix of this report contains a study of junction capacitance at the load end of the wire in a cylindrical cavity. Such results would be needed in the theoretical modelling of the cavity circuit.

SECTION 2

DESCRIPTION OF THE EXPERIMENTAL FACILITY

The facility utilized in making the swept-frequency measurements for this contract is an anechoic chamber operated over a frequency range of 118-4400 MHz. The data acquisition instrumentation for the chamber is fully automated and digitally controlled by a desktop computer. Data is acquired in digital form over three frequency bands: 118 to 1000 MHz, 940 to 2100 MHz, and 2000 to 4400 MHz. Both the amplitude and phase of the signals are measured, and the results are normalized to an incident plane EM wave.

A block diagram of the measurement system is shown in Fig. 2.1. Control of the instrumentation is accomplished via an HP-9830 desktop computer. In the first part of the data acquisition process, the sweep generator is programmed by the HP-9830 to output one of several discrete frequencies equally spaced throughout each frequency band. This signal is amplified by the power amplifiers, and a portion of it is sampled and fed into an EIP Model 371 source-locking frequency counter, which was purchased under this contract. By itself, the sweep oscillator can produce an RF signal within approximately 5.0 MHz of the frequency for which it is programmed, and this signal can vary over several MHz during a 24 hour period. However, with the addition of the source-locking capability of the EIP-371 counter, the output of the sweep oscillator can be stabilized to within a few Hz of the desired frequency. Since this locking process is controlled by the 9830, the exact same frequencies can be generated on a day-to-day basis, without the drift previously encountered. This is important since calibration measurements are often made on

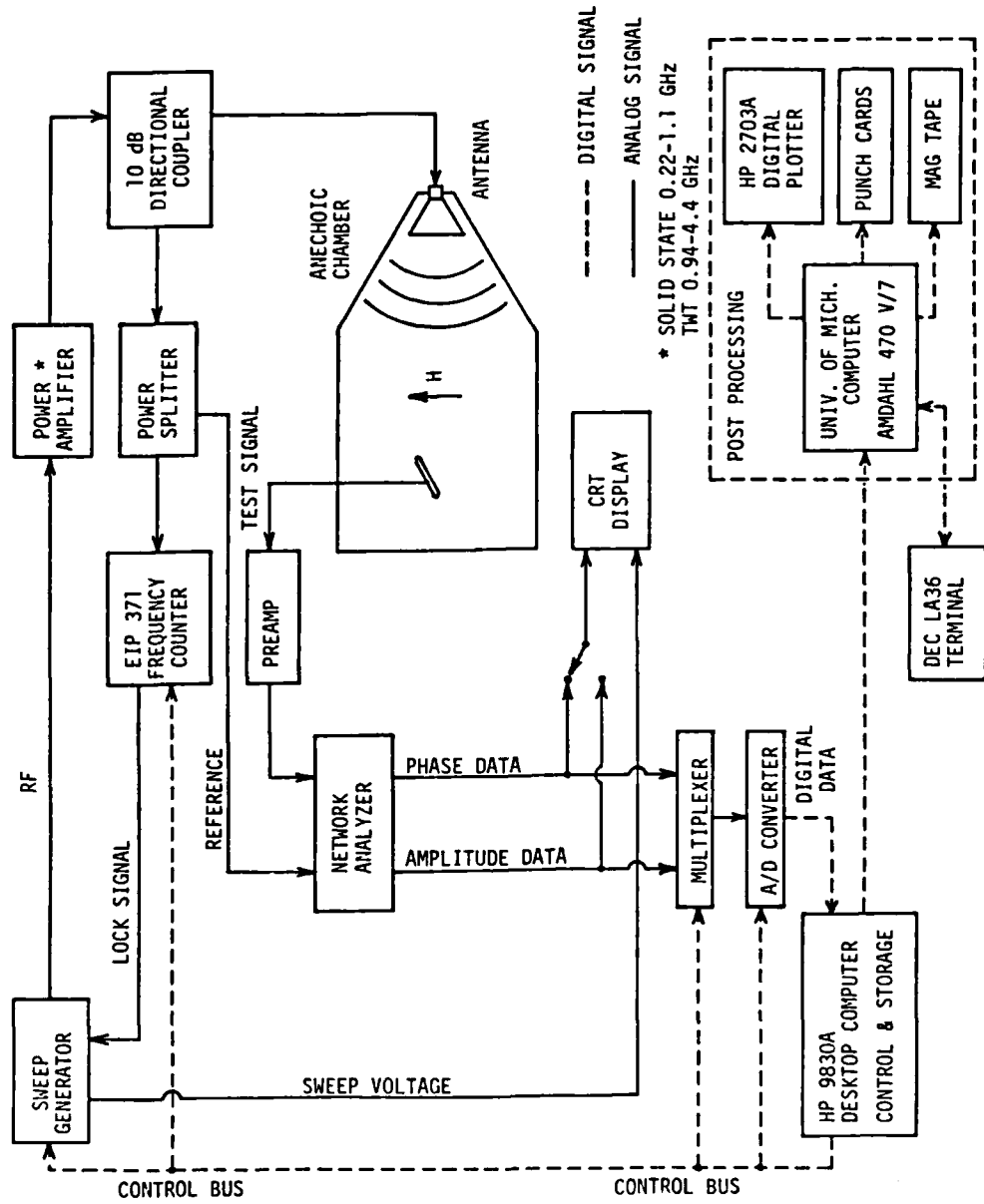


Figure 2.1. Block diagram of the facility.

different days than the test measurements. Also, measurements can be accurately repeated if necessary.

The now stable RF signal, after amplification, is fed to a wide-band antenna at the front of the anechoic chamber, which illuminates the body being measured. A directional coupler and power splitter at the input to the antenna provide reference RF signals for the frequency counter and an HP-8410B network analyzer.

Inside the chamber, small probes mounted on or inside the object under test measure the current and/or charge distributions induced by the field from the antenna. The probe leads are positioned for minimum interaction with the test model and the incident field. The signal from the probe is then preamplified and input to the network analyzer. The network analyzer outputs analog voltages which are proportional to the amplitude and phase of the probe signal relative to the amplitude and phase of the reference signal. These voltages are sent to a CRT display where they can be monitored by the operator, and to a multiplexer under control of the 9830, which alternately switches the amplitude and phase voltages into an analog-to-digital converter. The amplitude and phase data, now in digital form, is read into the 9830 and stored there in memory.

The entire procedure described above is repeated at equally spaced intervals throughout each frequency band. Thus a discrete sampling of the amplitude and phase of the probe signal is obtained directly in digital form in the 9830 memory. This data is copied on magnetic tape at the completion of each frequency band, and is thus available for subsequent processing. The processing of the data takes place initially on the 9830, and then it is transferred to the

University of Michigan computer system for final reduction and plotting, as shown in the figure. In order to accommodate the large amount of data encountered in these measurements, the memory capacity of the 9830 was extended to 6K bytes with the purchase of a 4K byte add-on memory under this contract.

SECTION 3

PRELIMINARY MEASUREMENTS OF EM COUPLING INTO A CYLINDRICAL CONDUCTING CAVITY THROUGH A CIRCULAR APERTURE

Measurements were made of the electromagnetic coupling into a conducting right circular cylinder through a small circular aperture under E- and H-polarized incident fields. The cylinder was 45 cm (17.7 inches) long with a radius of 2.775 cm (1.1 inches). A 1.27 cm (0.5 inch) diameter circular aperture was located 15 cm (5.9 inch) from one end of the cylinder.

Two types of field probes were used in the measurements, as illustrated in Figs. 3.1(a) and 3.1(b). The first probe consisted of a long wire running the length of the cylinder down its axis. The wire was shorted to the cavity at the end nearest the aperture, while at the other end it was fed through an SMA chassis mount female connector to the center conductor of a 50 ohm cable.

For the second probe, the axial wire was shorted to both ends of the cavity and a rectangular wire loop 2.0 cm x 0.5 cm was placed near one extreme of the shorted wire. Figure 3.1(c) is a closeup view of the loop, one end of which was shorted to the endcap of the cavity, while the other end was fed through the SMA connector to the center conductor of a 50 ohm cable in a manner similar to the first probe. The effect of the two probes is to produce a loaded (low-Q) and unloaded (high-Q) resonant cavity respectively.

The measurements were made in an anechoic chamber over a frequency range of 200 to 1100 MHz using an experimental setup similar to that shown in Fig. 2.1. For all measurements, the cylinder was oriented such that the excitation field was incident normal to the center of the aperture.

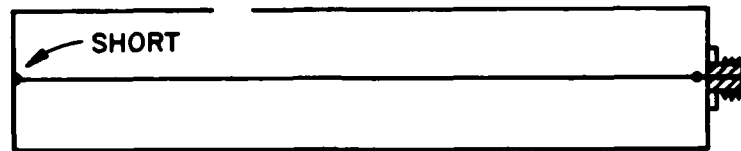


Figure 3.1(a). Low-Q probe mounted in cylinder (not to scale).

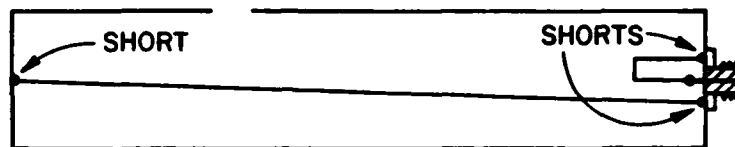


Figure 3.1(b). High-Q probe mounted in cylinder (not to scale).

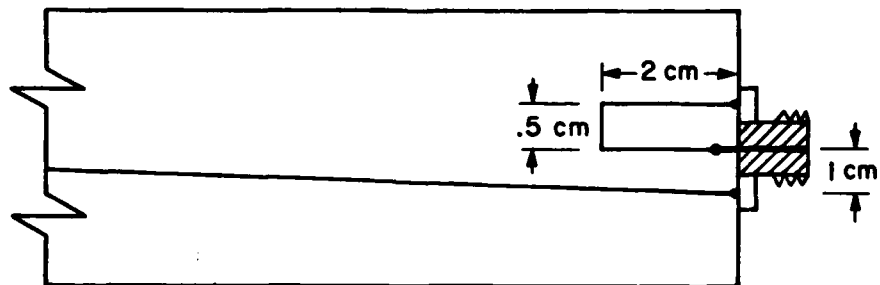


Figure 3.1(c). Full-scale view of high-Q probe mount (not to scale).

Four experiments were carried out on the cylinder:

1. Incident E-field parallel to the axis of the cylinder, low-Q probe.
2. Incident H-field parallel to the axis of the cylinder, low-Q probe.
3. Incident E-field parallel to the axis of the cylinder, high-Q probe.
4. Incident H-field parallel to the axis of the cylinder, high-Q probe.

Each experiment consisted of two measurements; first with the aperture covered with conducting tape, and the second with the tape removed. The resulting signal excited on the probe for the four experiments are shown in Figs. 3.2(a) through 3.2(d).

An examination of the resonant frequencies in plots 3.2(a) and 3.2(c) indicates they correspond to TEM modes (cavity length = $n \lambda / 2$). It is also obvious from 3.2(b) and 3.2(d) that energy from these modes is coupled to both probes only under E-polarization. Because of this fact, a new probe was designed to couple energy into the TEM modes under both E- and H-polarizations. This new probe is discussed below.

In order to cross-couple energy from the H-polarized incident field to the TEM modes normally excited under E-polarization, a probe was needed in which a circumferentially excited current on the probe (H-polarization) could be converted into an axial current (TEM mode). To accomplish this, the straight axial wire of the high-Q probe was replaced by a straight wire with a single turn spiral

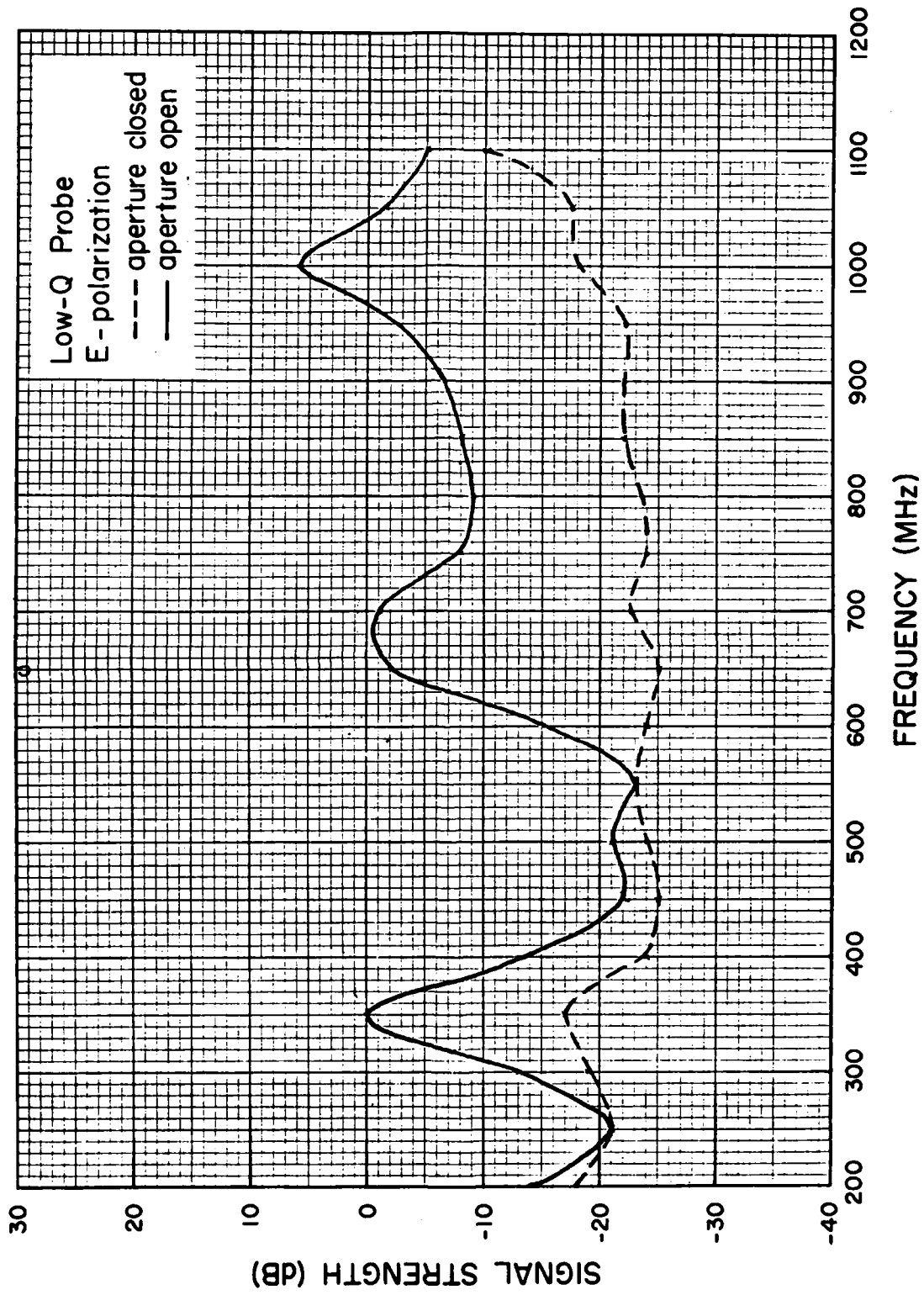


Figure 3.2(a). Interior response of the cylinder; Low-Q probe, E-polarization.

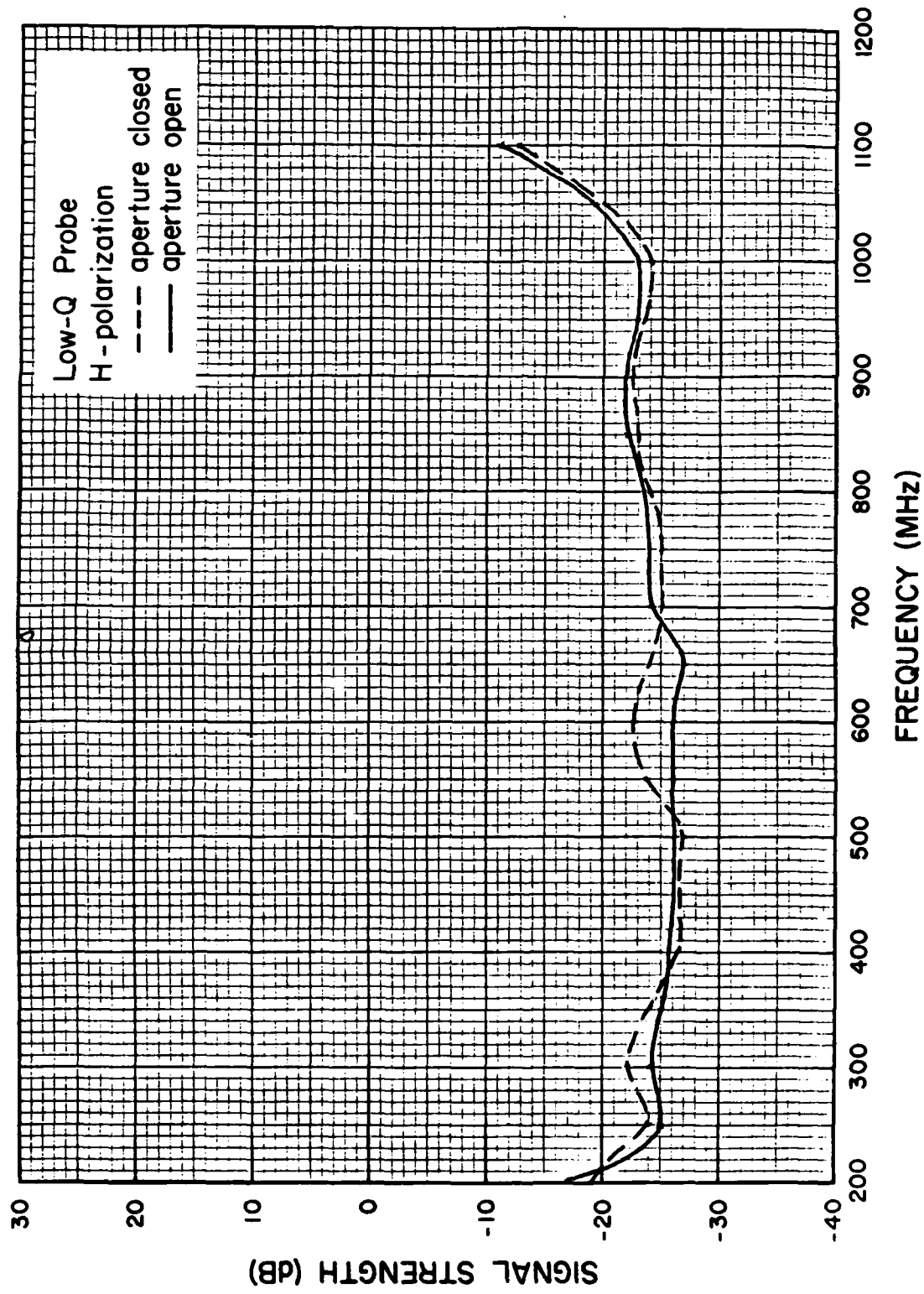


Figure 3.2(b). Interior response of the cylinder; low-Q probe, H-polarization.

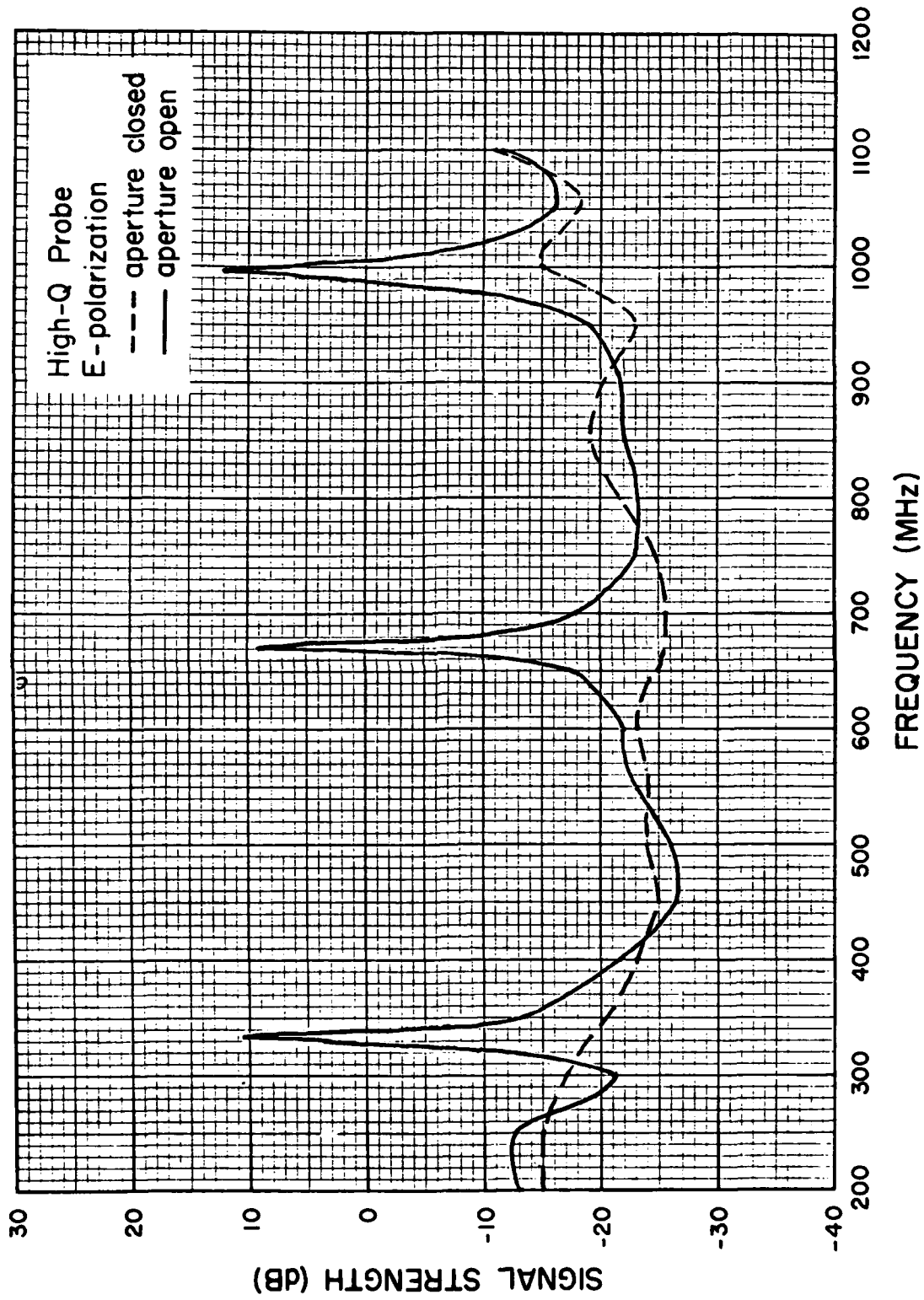


Figure 3.2(c). Interior response of the cylinder; high-Q probe, E-polarization.

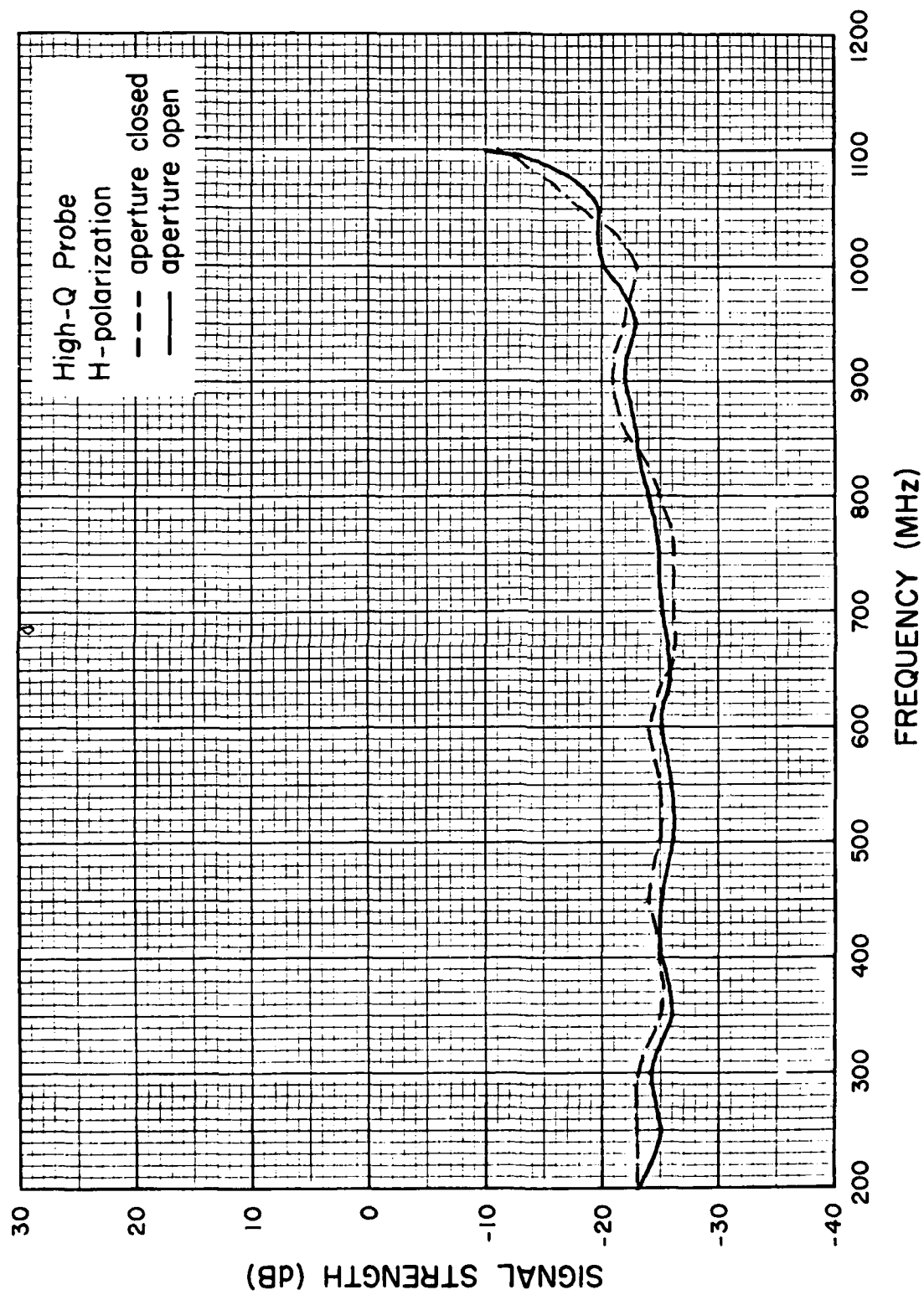


Figure 3.2(d). Interior response of the cylinder; high-Q probe, H-polarization.

centered below the aperture. A diagram of the wire and its dimensions are shown in Fig. 3.3. Under H-polarization, the circumferential field from the aperture has a component which excites a current in the spiral. This current travels down the axial portion of the wire and in turn excites the TEM modes. The small loop then picks up the signal from these modes.

The cylinder was placed in an anechoic chamber and oriented in the same manner as in Part I. The frequency range used was extended to cover 200 to 4400 MHz. The resulting relative signal amplitude is shown in Figs. 3.4(a) and 3.4(b) under E- and H-polarizations, respectively. Both plots show the equally spaced TEM resonant peaks throughout the entire band. The difference between the relative heights of the peaks is due to a lack of resolution in the digitally acquired data (frequency increment being too large), as well as the generally higher coupling under E-polarization. The irregularly spaced peaks above 3200 MHz are higher-order cavity modes (TE and TM).

Signal-to-noise ratio under both polarizations for this probe was 25 to 30 dB nominally, and 40 dB maximum.

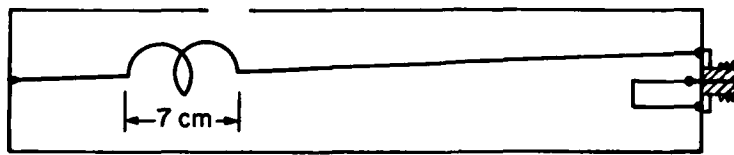


Figure 3.3. Spiral probe, spiral radius = 1.15 cm.

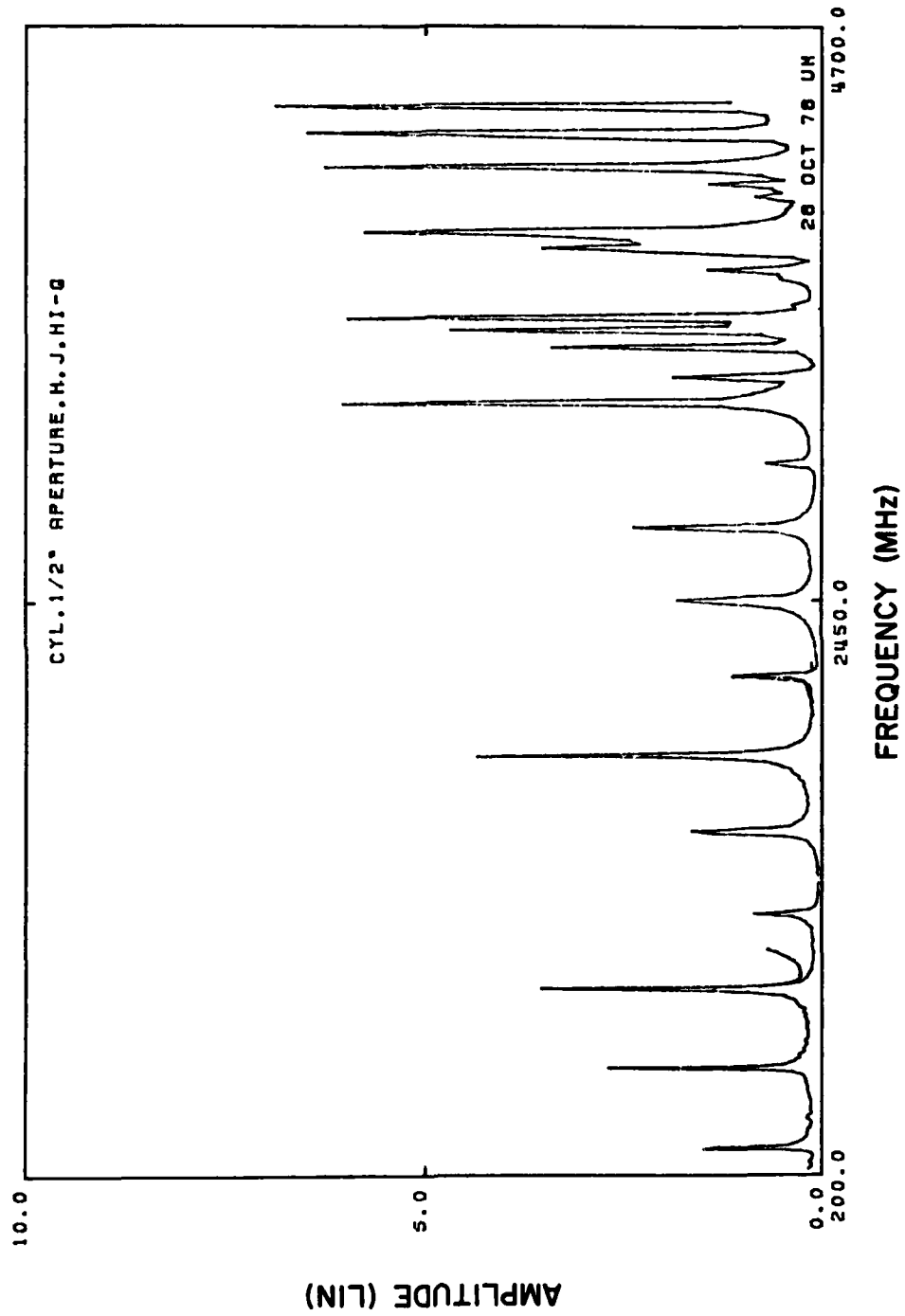


Figure 3.4(a). Spiral probe, E-polarization.

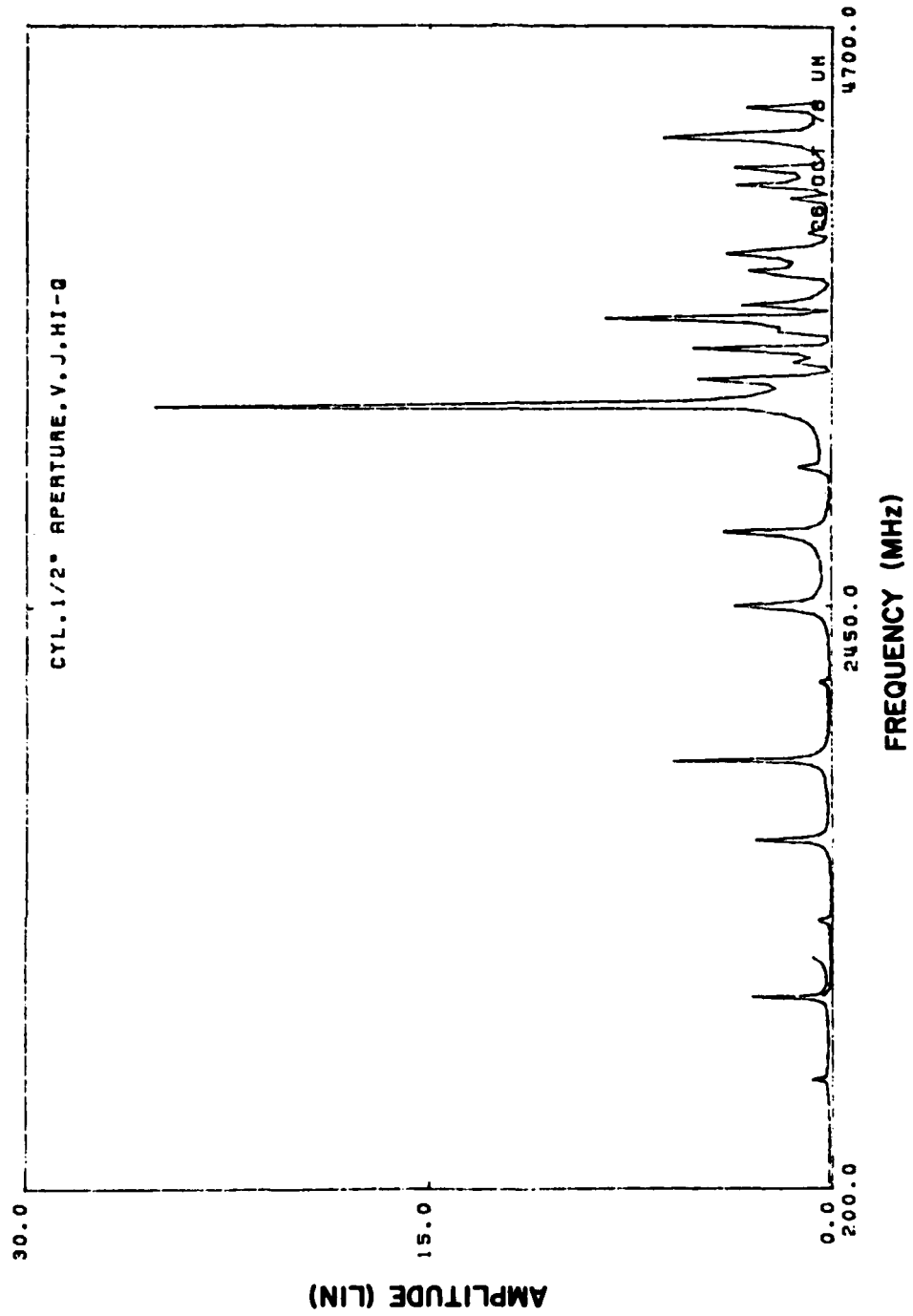


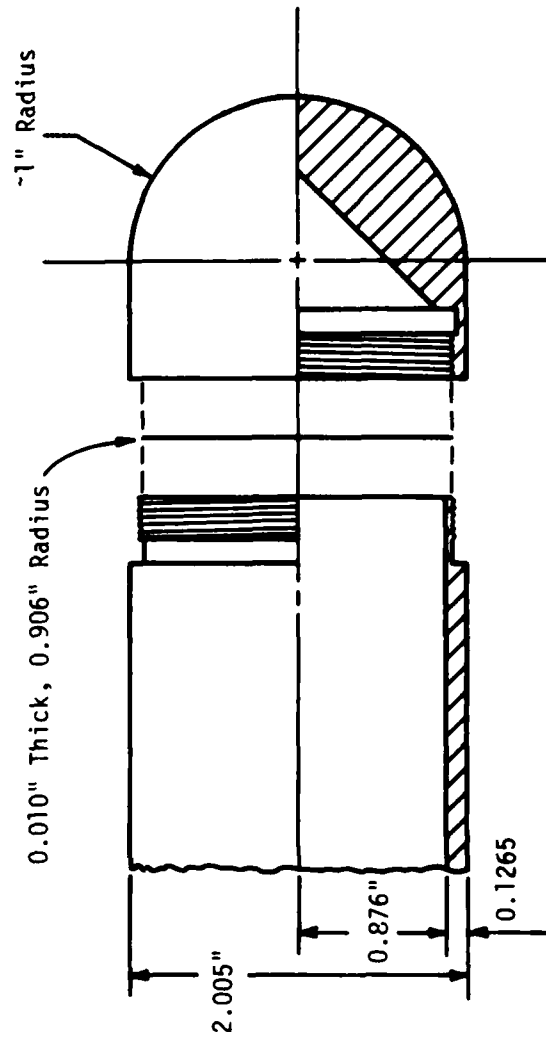
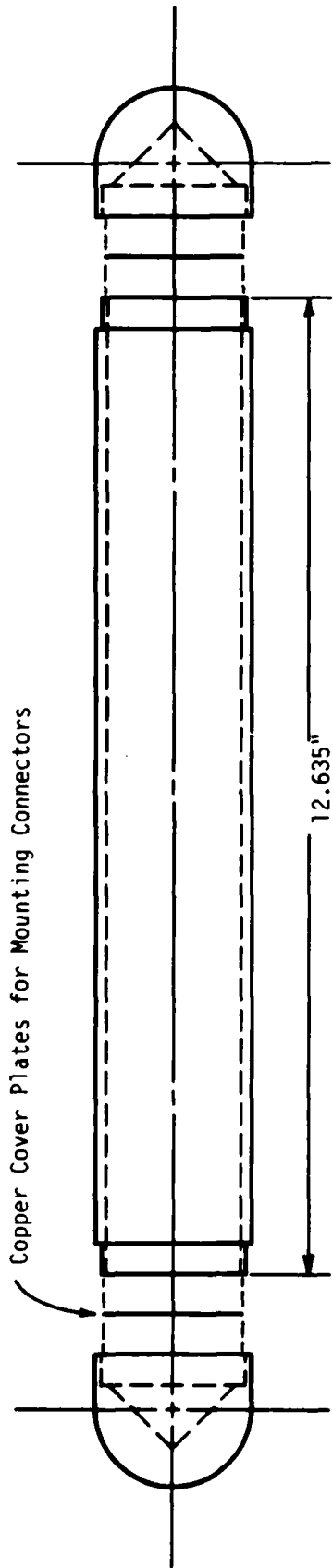
Figure 3.4(b) Spiral probe, H-polarization.

SECTION 4

TEST MODEL, MEASUREMENTS, AND DATA

4.1 The Model. The model used in obtaining the data presented in this section is a modified version of the one described in Section 3 of this report. It consists of a right circular cylinder terminated by two hemispherical caps as shown in Fig. 4.1. The entire model is made of machined brass, with a diameter of 2.005 inch and an overall length of 15.20 inches. The hemispherical caps are threaded on the cylinder so that they may be removed in order to mount sensors inside the cavity. As shown in Fig. 4.1, two small cover plates are inserted between the cylinder and the caps. These serve to truncate the interior of the model in the shape of a right cylindrical cavity of length 12.635 inches, as well as to provide a surface for mounting the interior sensor and its associated connectors. In order to provide coupling between the exterior surface fields on the model and the interior cavity, a circular hole $3/8$ inch in diameter was drilled at a distance of 3.8 inches from one end of the model as shown in Fig. 4.2(a). This hole was also used for mounting the probes used in measuring the exterior surface current and charge distributions.

Measurements on the interior of the model were made with the sensor illustrated in Fig. 4.2(b). The sensor consisted of a length of 0.030 inch diameter wire running axially down the cavity. The wire was shorted at the end of the cavity nearest the $3/8$ inch hole (end B) and terminated in a 50-ohm load at the other end (end A). It was across this 50-ohm load that the internal signal was measured.



Overall Length - 15.200"
 Assembly Drawing - Half Scale
 Half Section - Full Scale

Figure 4.1. Mechanical design.

Case I: Center conductor terminated in a 50-ohm load.

(a)

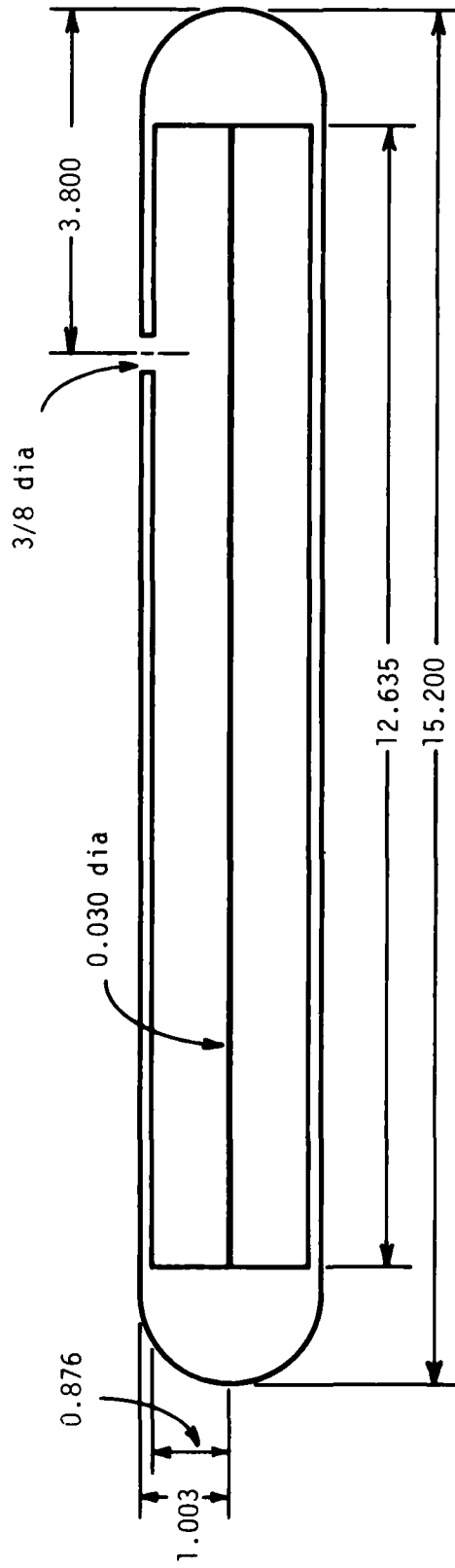
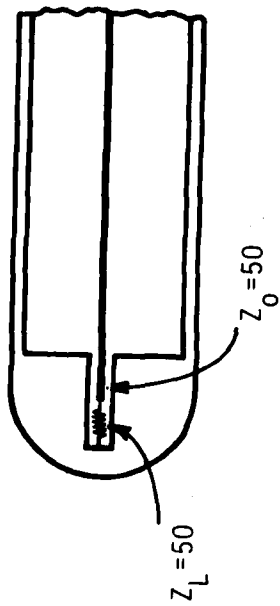


Figure 4.2(a). "Electrical" dimensions.



Internal signal measured across a 50-ohm load.

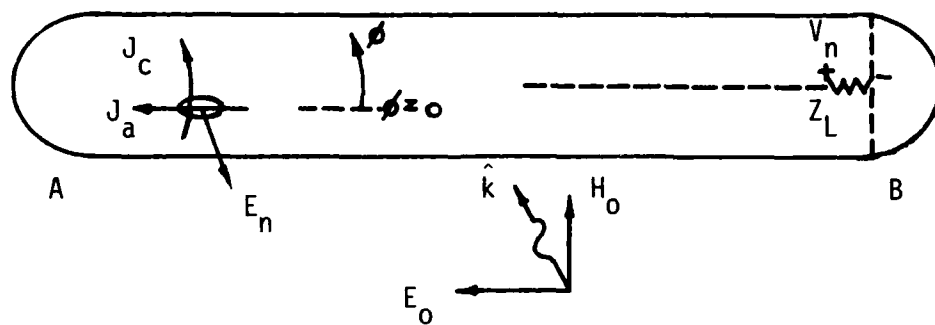
$$\frac{V_{loop}}{H_{inc}} = T_z \frac{J_z}{H_{inc}} + T_\phi \frac{J_\phi}{H_{inc}} + T_n \frac{E_n}{E_0}$$

Figure 4.2(b). Details of the internal load.

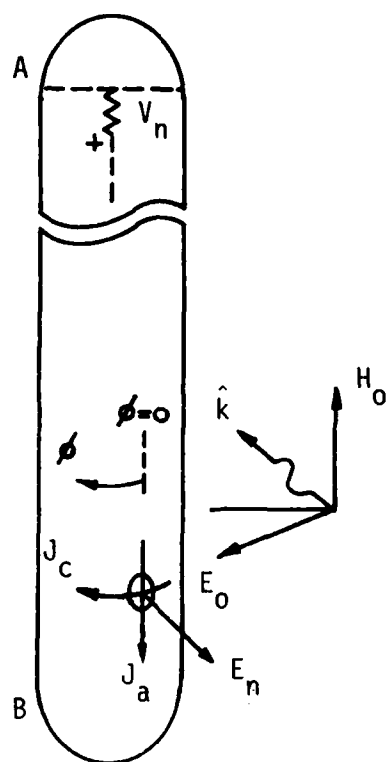
4.2 Measurements. The exterior and interior measurements were performed using procedures and techniques developed for scale model aircraft measurements related to studies of external EMP coupling. Figure 4.3 shows the orientation of the cylinder and the measurement point with respect to the incident electromagnetic field. The exterior data measured were the axial and circumferential currents, J_a and J_c , and the normal electric field (charge) E_n . Note that for parallel polarization (also referred to as horizontal orientation because the cylinder was horizontally mounted in the anechoic chamber) the incident electric field vector is in a direction toward end B (the end nearest the hole) and for the perpendicular polarization (vertical orientation) the incident magnetic field vector is toward end A.

4.3 Data. The data that has been measured is summarized in Table 4.1 and Table 4.2 for parallel and perpendicular polarization respectively. The J_a , J_c , and E_n are the exterior (short circuit) measurements and V is the interior measurement. All the exterior data are normalized to the incident fields, i.e., J_a/H_0 , J_c/H_0 , and E_n/E_0 and the incident field phase reference is the front of the cylinder ($\phi = 0$). For the interior measurements it took some doing, but eventually we were able to obtain a normalized measurement for the amplitude with respect to the incident electric vector E_0 . The phase is within a constant kd (e^{-ikd}) where k is the wavenumber and d is an unknown displacement, and is the same for all interior measurements.

Figures 4.4 through 4.10 show samples of amplitude data measured. As can be seen from Tables 4.1 and 4.2, there are 36 such plots generated with corresponding phase plots.



(a) Parallel polarization (horizontal).



(b) Perpendicular polarization (vertical).

Figure 4.3. Convention for illumination and the measured field components.

Table 4.1. Parallel polarization data.

ϕ , deg	J_a , ext.	J_c , ext.	E_n , ext.	V, int
0	CYLHA000*	CYLHC000	CYLHQ000*	CYLHN000*
45	CYLHA045	CYLHC045	CYLHQ045	CYLHN045
90	CYLHA090	CYLHC090	CYLHQ090*	CYCHN090*
135	CYLHA135	CYLHC135	CYLHQ135	
180	CYLHA180	CYLHC180	CYLHQ180	

* data plotted herein

Table 4.2. Perpendicular polarization data.

ϕ , deg	J_a , ext	J_c , ext	E_n , ext	V, int
0	CYLVA000	CYLVC000*	CYLVQ000	CYLVN000
45	CYLVA045	CYLVC045	CYLVQ045	
90	CYLVA090	CYLVC090	CYLVQ090	CYLVN090*
135	CYLVA135	CYLVS135	CYLVQ135	
180	CYLVA180	CYLVC180	CYLVQ180	
270				CYLVN270

* data plotted herein

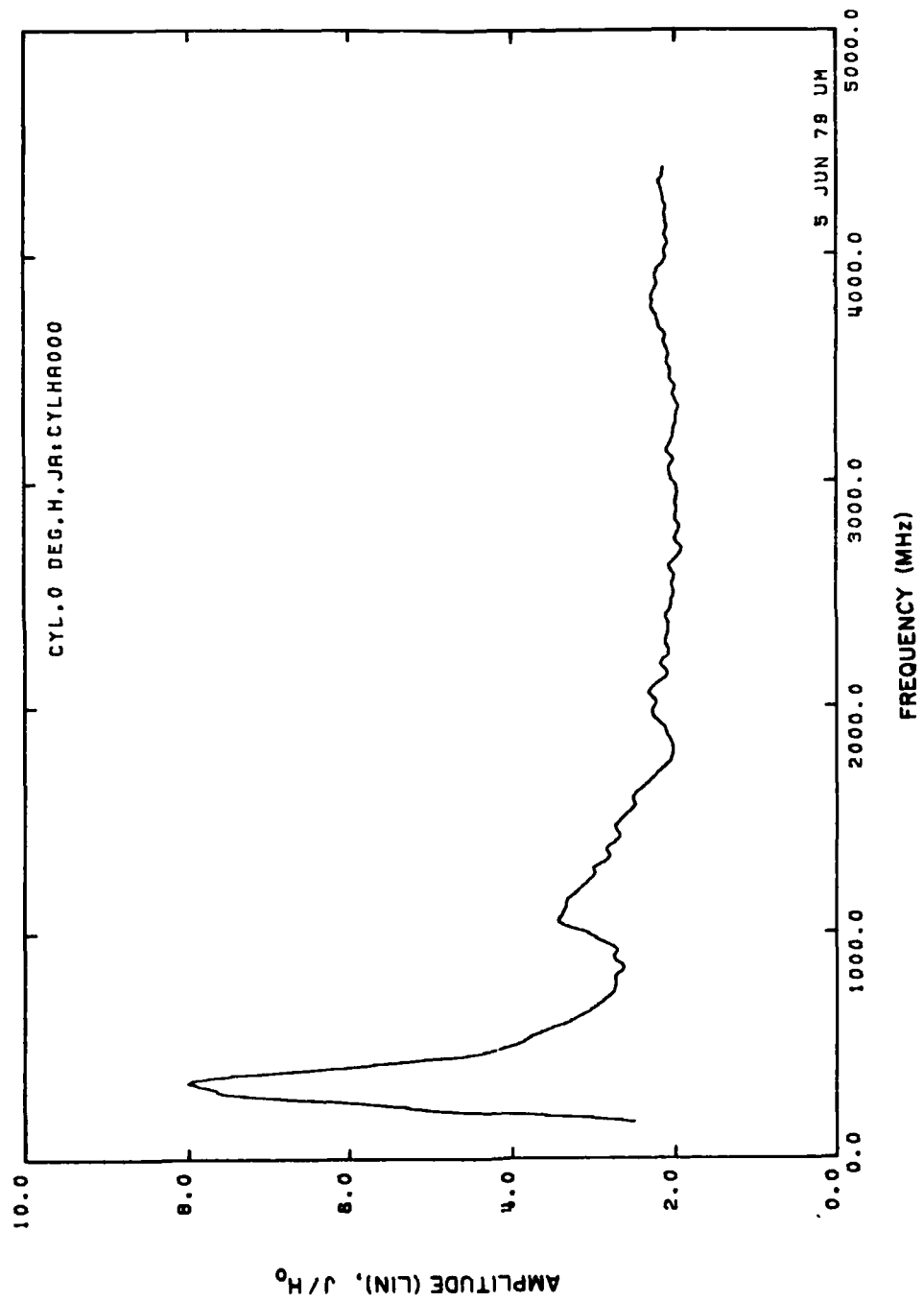


Figure 4.4. Exterior axial current density, $\psi = 0^\circ$.

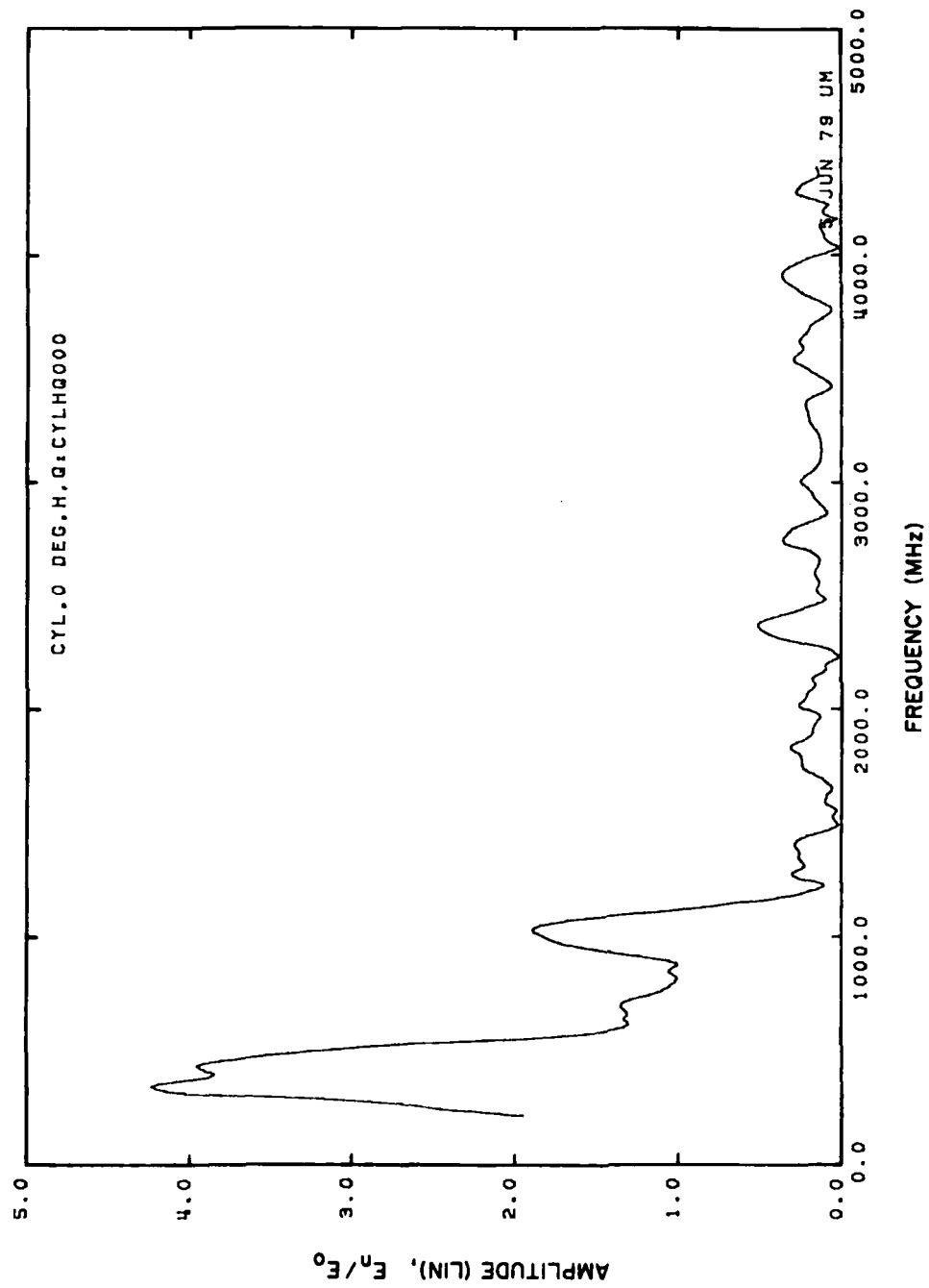


Figure 4.5. Exterior surface charge density, E-pol, $\phi = 0^\circ$.

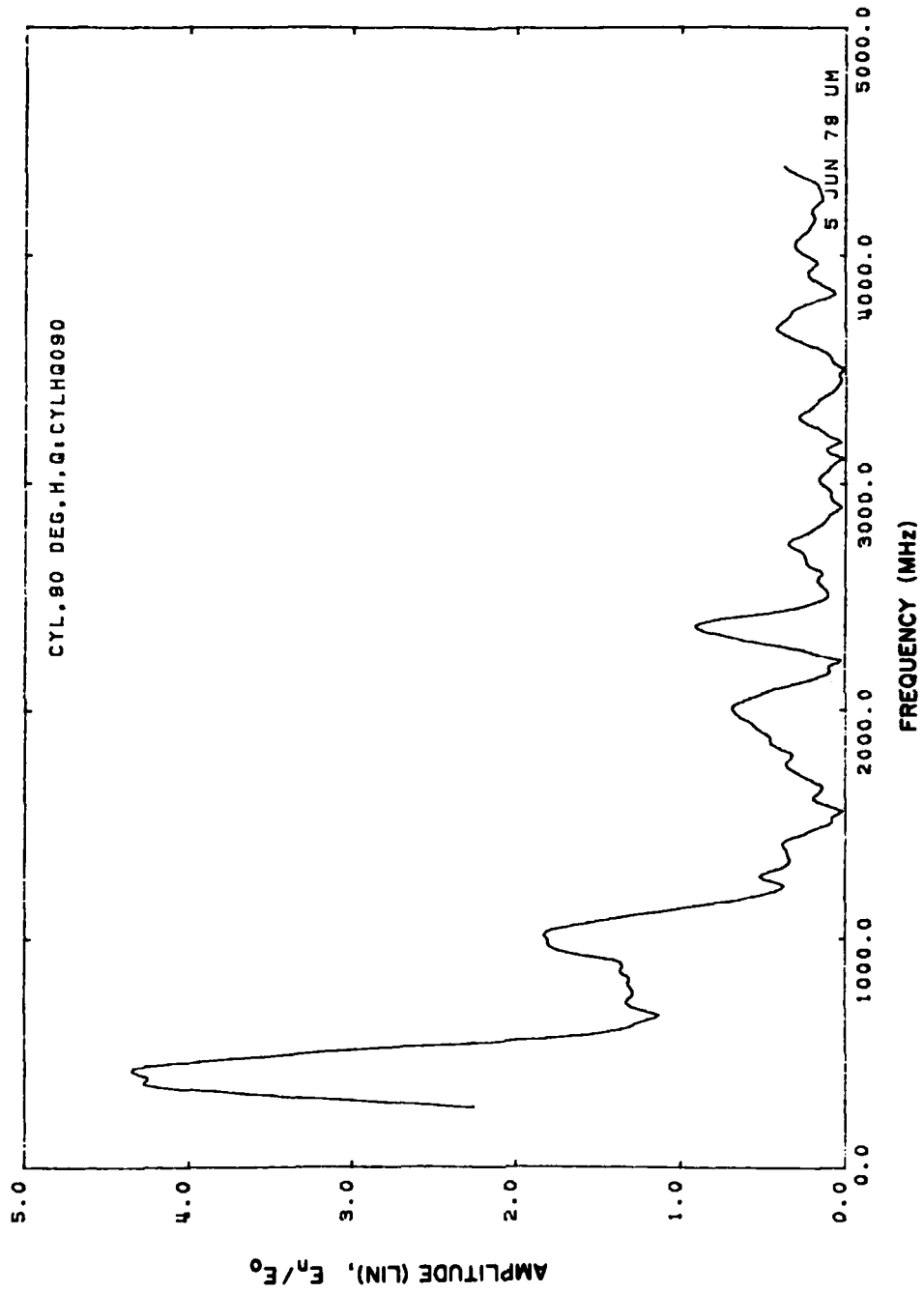


Figure 4.6. Exterior surface charge density, E-pol, $\phi = 90^\circ$.

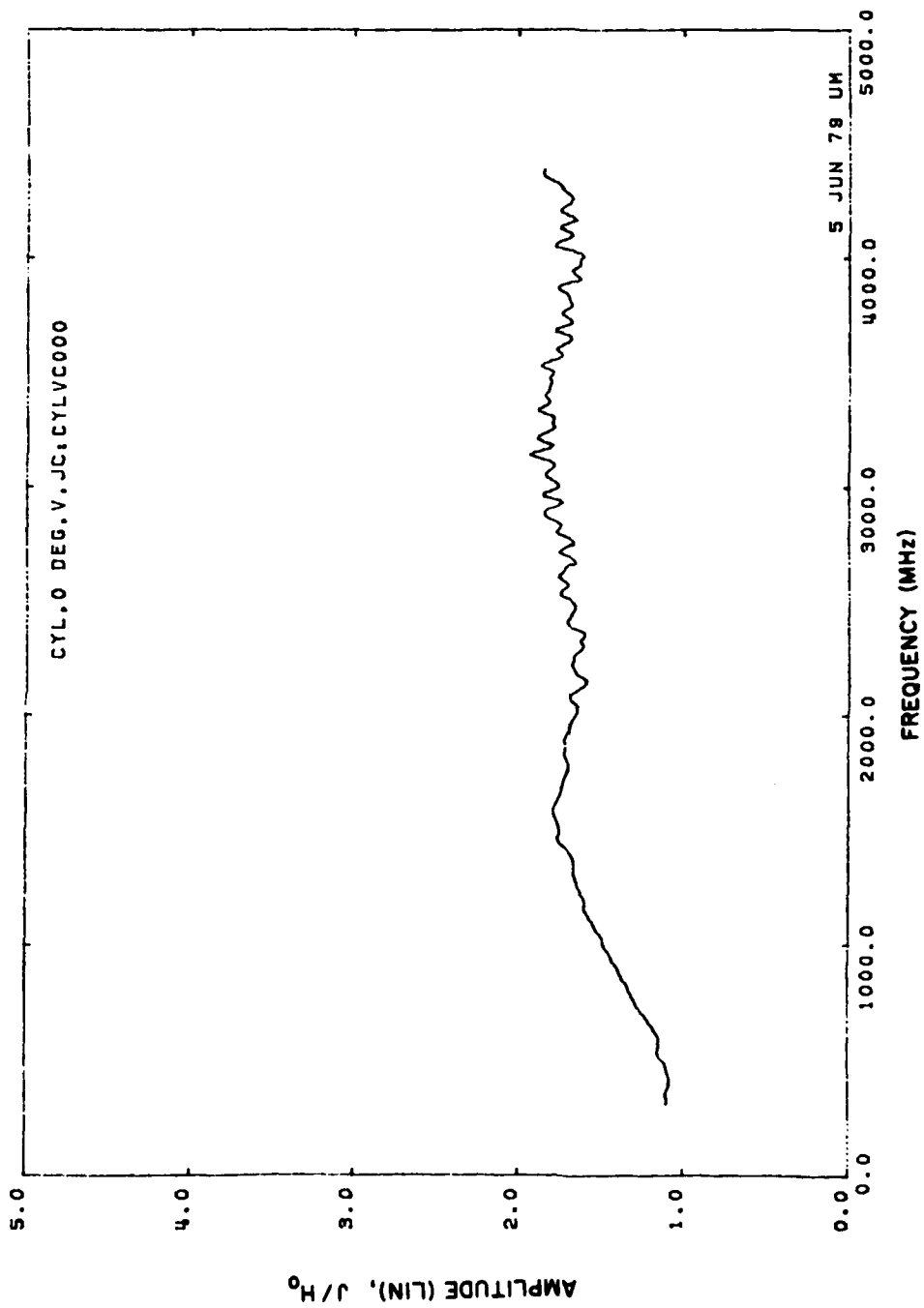


Figure 4.7. Exterior circumferential current density, H-pol, $\phi = 0^\circ$.

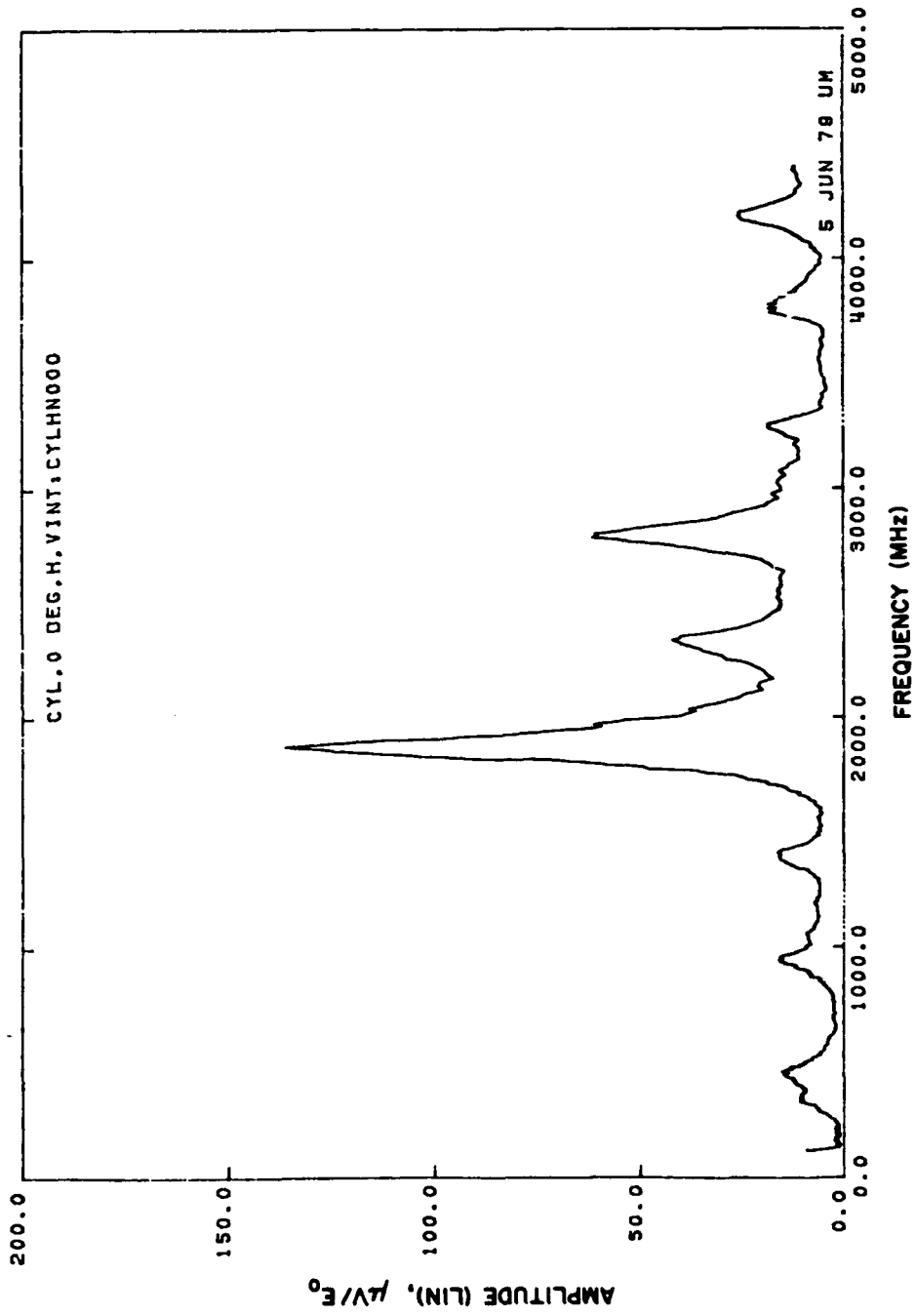


Figure 4.8. Interior voltage, E-pol, $\phi = 0^\circ$.

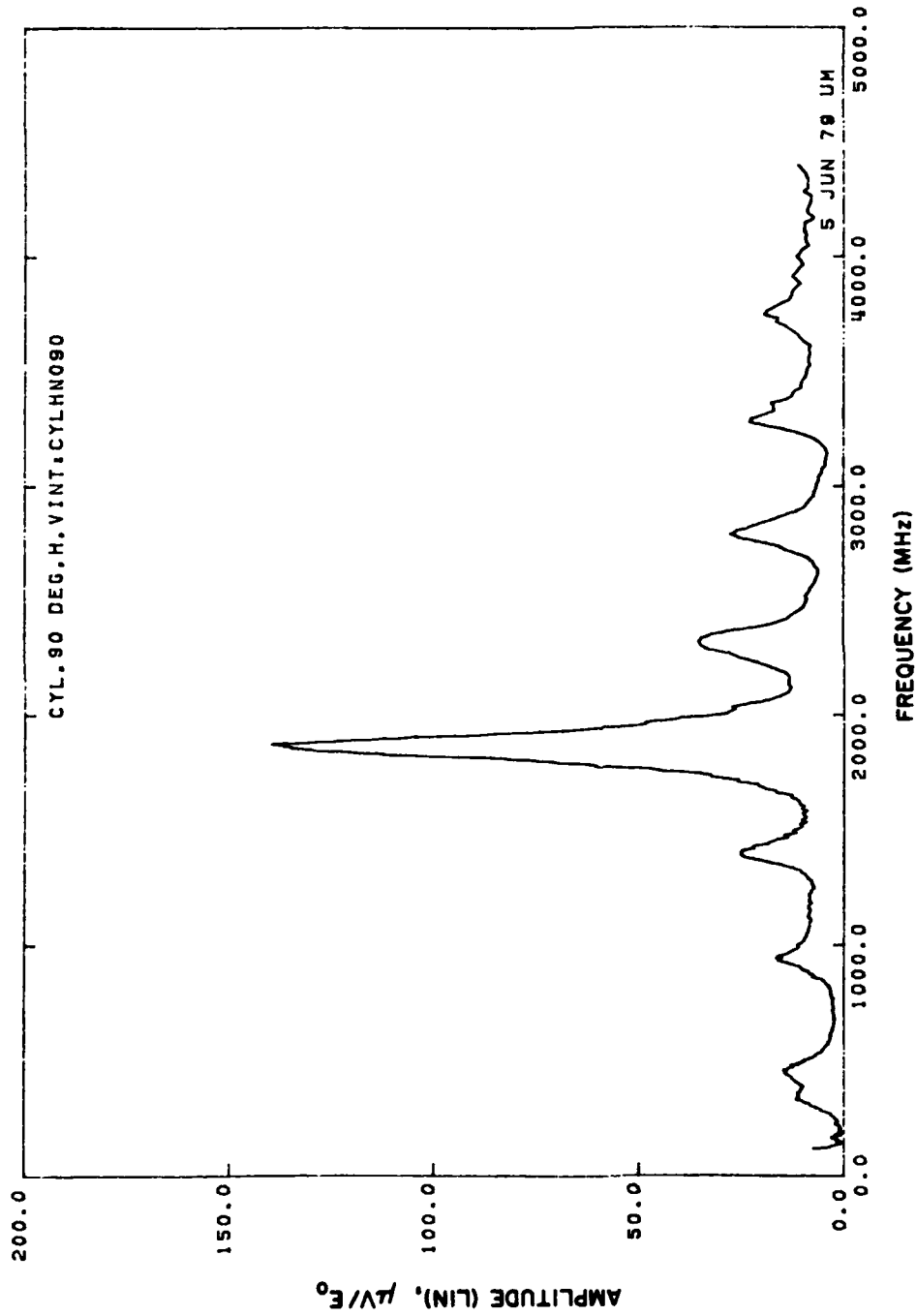


Figure 4.9. Interior voltage, E-pol, $\phi = 90^\circ$.

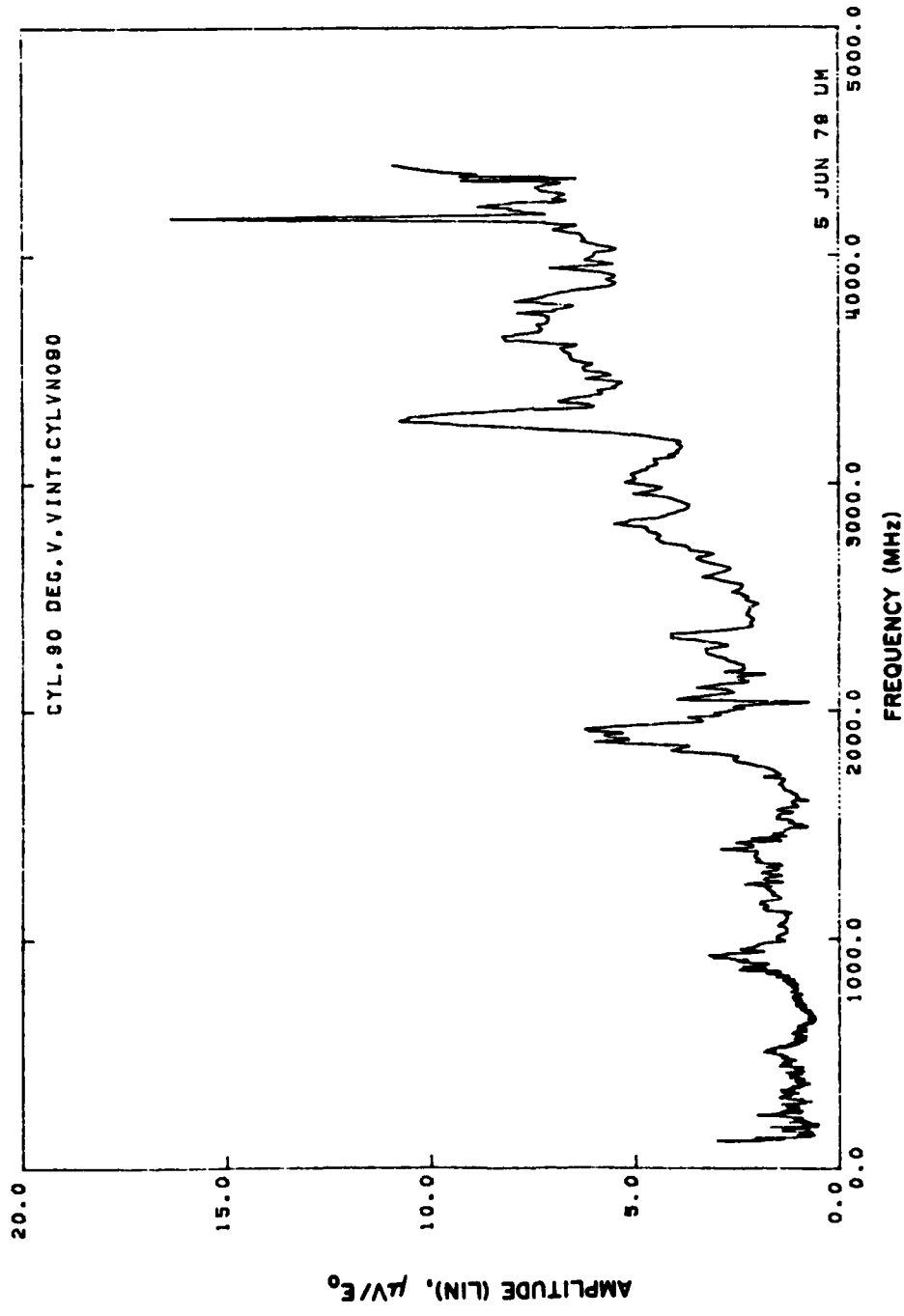


Figure 4.10. Interior voltage, H-pol, $\phi = 90^\circ$.

The data measured was forwards as plots and on digital tape to Dr. Maurice I. Sancer of R&D Associates. They processed and analyzed the data and their findings are presented in reference [5].

SECTION 5

CYLINDERS NEAR THE GROUND PLANE

Judging from the difficulties encountered in processing the data we recognized that perhaps in those measurements we were too ambitious when we tried to provide numerous answers from a single study. Pulling out the transfer coefficients (see Eq. (1)), by solving three simultaneous equations for three unknowns seemed like a straightforward task, but we underestimated the impact the noise would have in the processing of the data. Consequently, a simpler experiment was conceived, where only the axial current would couple into the interior of the cylinder. Also, this experiment would demonstrate the transfer coefficient dependence on the exterior environment (i.e., the ground plane). To do this, the coupling hole on the test cylinder was moved to the center and only E-polarization was used. In such a case the transfer coefficient can simply be obtained by taking the ratios of the interior voltages to the short circuited exterior fields. To make the study more applicable to the real situation (such as an aircraft sitting on the ground), the measurements were performed on the cylinder in the presence of a ground plane. This then can provide answers to the questions of the transfer coefficient sensitivity when the model is in the presence of another body. Again, data from this study was delivered to Dr. Sancer for further analysis [5].

This study in most respects follows the previous measurements, but where applicable, we improved the experimental setup and the measurement procedures.

5.1 Ground Plane. Ideally, the ground plane should be infinite in extent, but such requirements create enormous difficulties

even if infinite means the size of the anechoic chamber. To make measurements in an anechoic chamber on a ground plane, immediate reactions would be to construct a ground plane over the entire wall (or the floor) as the case may be and bury the metal edges in the absorber to simulate an infinite extent. For a geometry of a cylinder near a ground plane with perpendicular incidence to the sheet, this would require an erection of a metal wall to replace the absorber on the back wall with a metal plate. In addition to being difficult to implement and also very costly, such a ground plane, however, would not work well in the sweep frequency measurement mode as used for these measurements. The signal reflected by the plane would interact with the illuminating antenna causing large oscillatory signal behavior as a function of frequency. One could avoid this interaction by tilting the ground plane away from the normal incidence, but such would not be a simple task when a ground plane is, (say), 18 feet wide and 12 feet high.

Instead, we chose to work with a finite size portable ground plane that can be assembled inside the chamber and easily tilted in case the need existed to do so. A consequence of using a finite size ground plane is that due to the effect of the edge diffraction the surface fields on it depart from an infinite plane value. For normal incidence on a rectangular ground plane several wavelengths in dimension the departures are primarily due to the edges perpendicular to the incident electric vector. As a result a standing wave pattern across the plate is set up. The influence of the other edges (when the incident electric field is parallel to the edge) is confined to a distance of a wavelength (or less) from the edge [7].

To reduce the surface field perturbation created by the vertical edges, resistive sheets were added as shown in Fig. 5.1. Each sheet was shaped like a quarter cylinder of radius 25.5 inches and had a resistivity which increased quadratically as a function of the surface distance from the metallic plane. The effect of different resistivity variations was determined by numerical experiments carried out using codes for scattering by resistive sheets and the resistivity that was finally selected started with zero at the edge, increasing quadratically to about 1000 ohms/square at the rear.

The sheets were fabricated by spraying thin layers of resistive material on stiff art paper. After each treatment the resistivity was measured with an ohmmeter and the process repeated until the appropriate resistivity profile was achieved. The final product had a resistivity which started at about 10 ohms/square and increased to the designed value of 1000 ohms/square at the outer edge. Although the surface fields on the metallic part of the resulting ground plane have not been measured, it is inferred from the numerical experiments that over a central portion of the plane, at least, the fields are virtually identical to those on an infinite metal plane.

5.2 The Model. The model for these measurements was made by taking the center section from the model used in the previous measurements and drilling a new 3/8 inch diameter hole in the center. (The previous hole was closed by applying a conductive adhesive tape over the outer and inner surfaces of the cylinder.) New cylinder end pieces were cut, this time with flat ends. Figure 5.2 shows the dimensions of the new cylinder. Overall, the cylinder is 15.120 inches long and 2.005 inches in diameter. The interior cavity

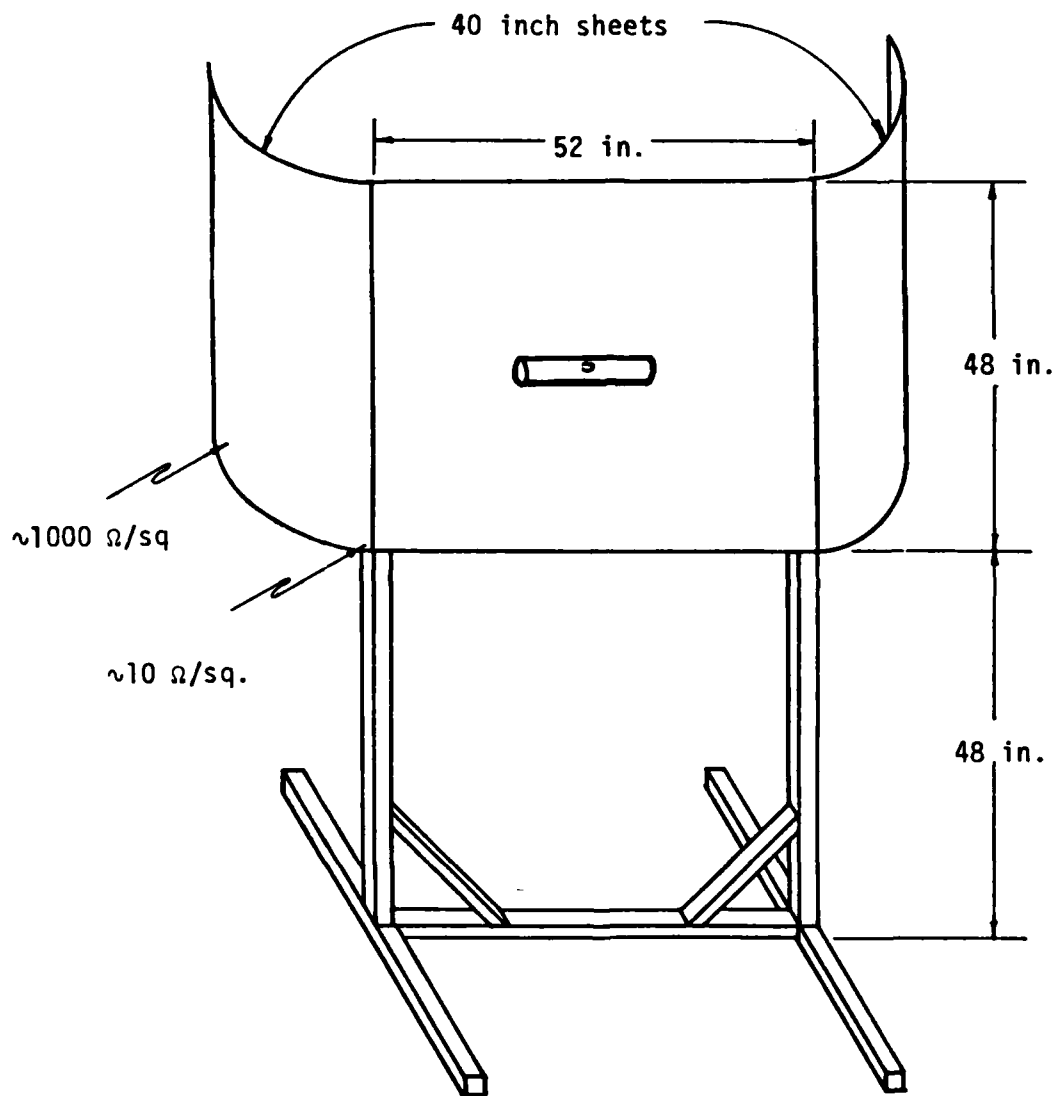


Figure 5.1. Resistively loaded ground plane used in the measurements.

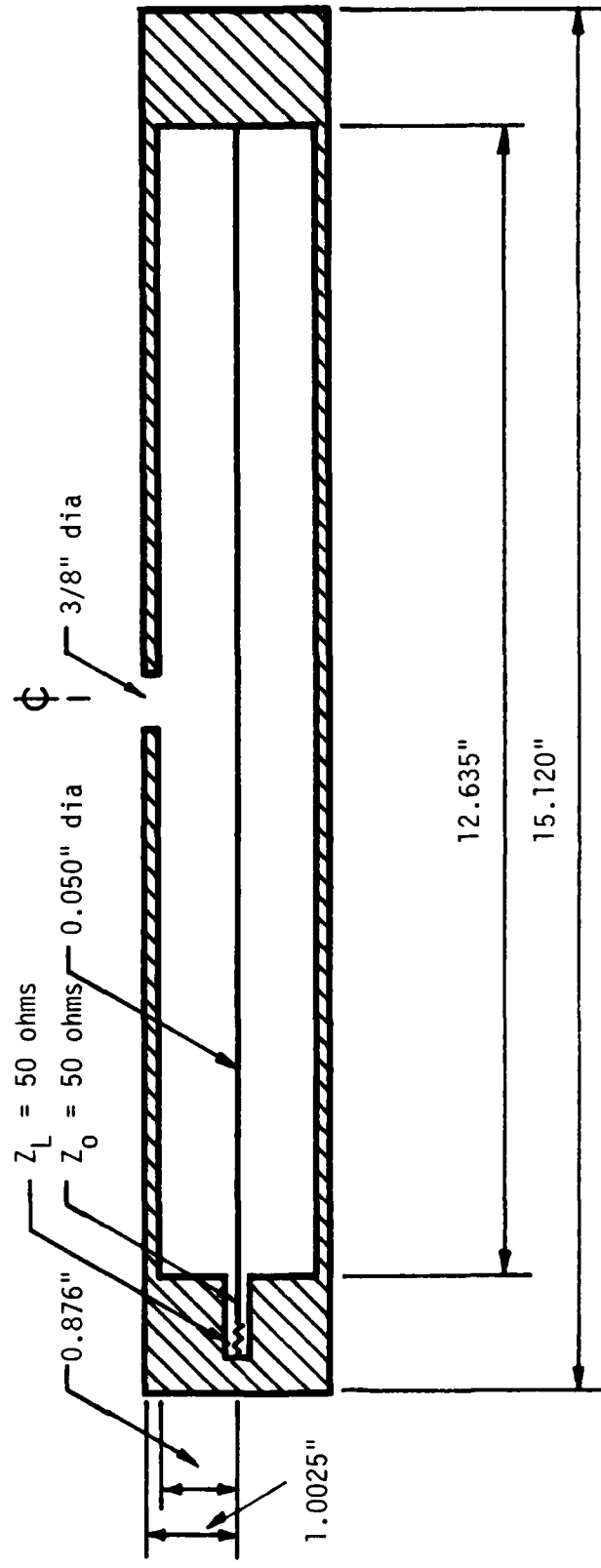


Figure 5.2. Pertinent dimensions of the second model.

dimensions are 12.635 inches long and 1.752 inches diameter. The diameter of the center wire is 0.030 inch which is shorted at one end and terminates into 50 ohms at the other end. In actuality the wire feeds a 50-ohm coaxial cable that goes to the network analyzer to measure the signal. The cylinder and its ends are made of brass, except for the center wire which is copper.

5.3 Experimental Arrangement. For the measurements, the ground plane was set up in the chamber as shown in the center of the equipment block diagram (Fig. 5.3). To put the reader in perspective, recall that in the chamber a horizontally polarized signal is transmitted from the right and impinges the ground plane at normal incidence. The cylinder is supported horizontally by strings and hung down from the top edge of the ground plane. It is spaced from the ground plane by styrofoam spacers. Figure 5.4 shows the geometry from the side and defines the pertinent parameters. The positions of the aperture and the short circuit measurements are defined by ϕ . When $\phi = 0$, the hole is on the illuminated side and when $\phi = 180$ degrees, the hole is facing the ground plane. The spacing from the ground plane to the center of the cylinder is D , but in presentation the spacing has been designated by D/A where A is the radius of the cylinder. Because of the difficulty of routing the signal lead from the cylinder, the symmetric property of the field in ϕ is employed and in certain instances measurements were made, say, for $\phi = -90$ degrees rather than the scheduled $\phi = 90$ degrees.

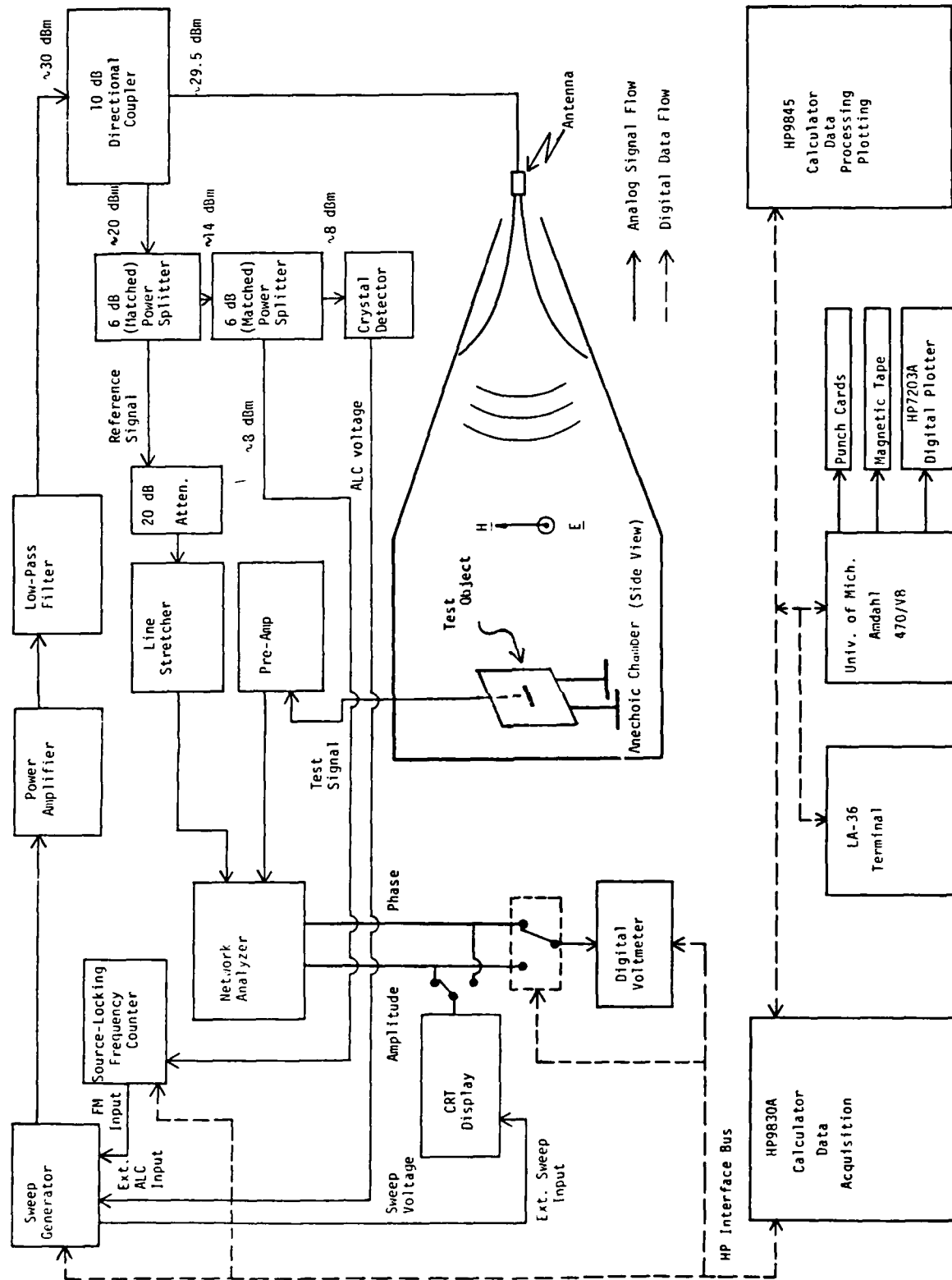


Figure 5.3. Block diagram of the facility.

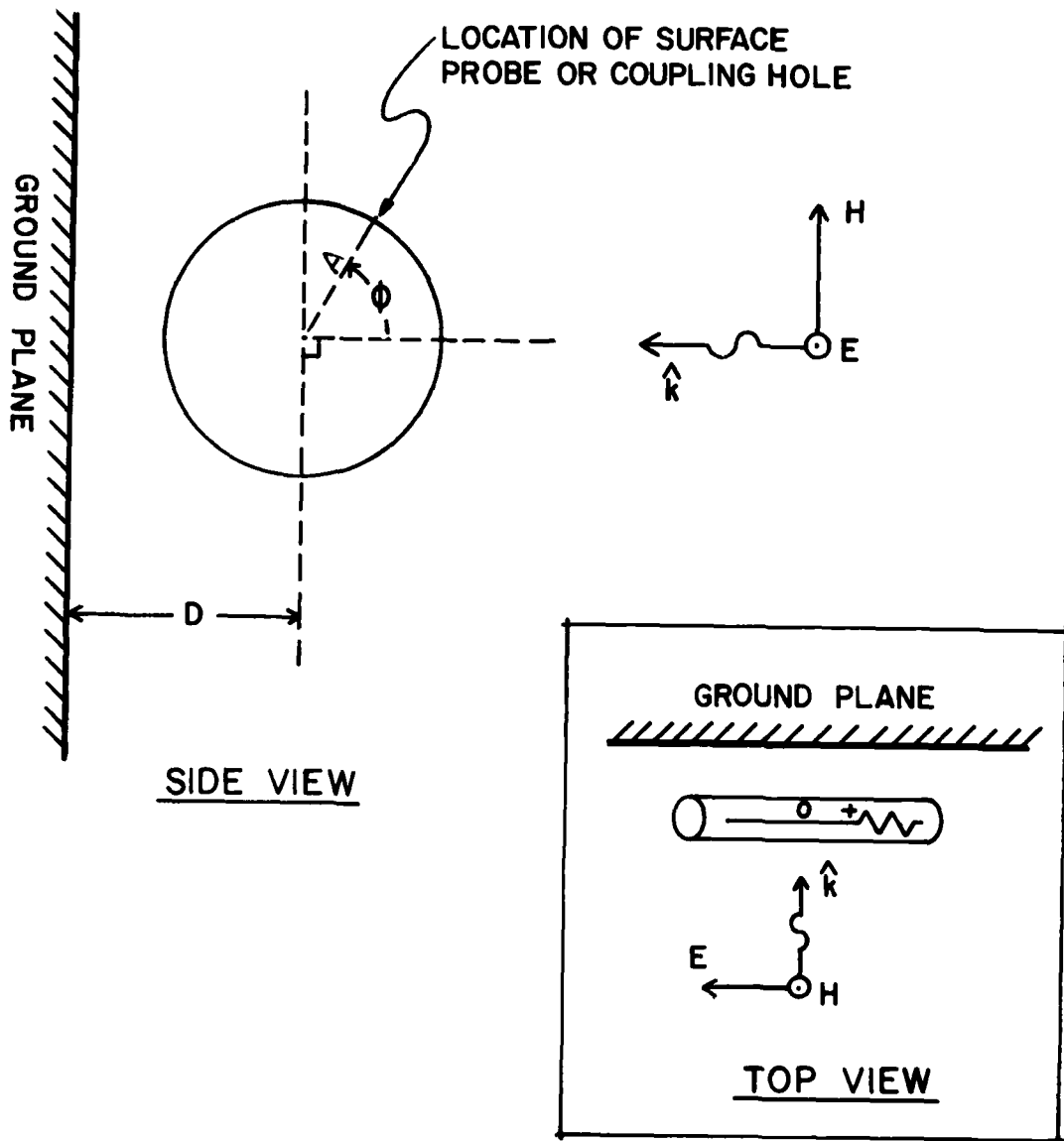


Figure 5.4. Schematic view of the experimental setup. (Insert shows the interior polarity)

5.5 Measurements. The measurements were carried out in two parts: (1) the exterior measurements and (2) the interior measurements. As mentioned previously, the geometry and the illumination were chosen such that only one exterior field component (the axial current) is excited. To measure this an EG&G MGL-8A(R) magnetic field sensor was used. This is a surface current sensor with the output connector feeding through the mounting surface. A 1/2 inch diameter hole in the surface is required to accommodate the sensor. Since this is larger in diameter than that of the coupling hole, on the cylinder, a 1/2 inch diameter hole was drilled in the wall on the side opposite the coupling hole. When making measurements the unused hole is always closed up with a conducting metallic tape. The exterior current on the cylinder was measured at $\phi = 0$ degrees, 90 degrees (or -90 degrees depending on convenience of routing the signal lead), and 180 degrees for ground plane-to-cylinder spacing of $D/A = 1.5, 2.0, \text{ and } 5.0$. After the cylinder measurements, the MGL sensor with exactly the same cabling was mounted on the ground plane and the ground plane current ($2 H_0$) was measured. The ratios of the cylinder measurement to the ground plane measurement gives surface current values relative to the ground plane current and simply by multiplying this result by a factor of two produces the surface current relative to the incident magnetic field. Note that via this calibration technique the ground plane is the phase reference of the incident field, i.e., the phase of the incident magnetic field, H_0 , is zero at the ground plane.

The interior measurements were carried out in a similar manner. In this case the cable that was previously attached to the MGL sensor was now connected to the end of the interior wire (Fig. 5.2). The measurements were repeated with the aperture locations in the same orientations where the MGL sensor was previously located. For the calibration measurements, the signal cable was disconnected from the cylinder (interior) connection and connected to the MGL-8 sensor mounted on the ground plane (without the cylinder present). Whereas for surface field measurements the actual sensor response need not be known (since it cancelled out in the calibration process), here the actual response

$$V(f) = A_{eq} \cdot j\omega\mu H \quad (3)$$

was used [8]. By taking the ratio of the interior measurements to the ground plane measurement and correcting for the probe response, the data in terms of V/H_0 is obtained.

The data are presented in the next section.

SECTION 6

DATA

Table 6.1 summarizes the data measured with the cylinder near the ground plane. The table consists of three parts: (A) Surface Field Measurement, (B) Interior Coupled-Field Measurements, and (C) Computed Transfer Coefficients. The latter is obtained by dividing the interior data (B) by the exterior data (A) and multiplying by 1000 to obtain units of mV/amp/m. The designations such as 'CYL1S' in the table refer to data plots and the filenames where the data have been stored on tapes.

All data have been recorded and processed over 118 to 4400 MHz, but since there is little meaningful information contained at higher frequencies, the data plots that follow have been plotted to 2500 MHz to show in more detail the resonance regions.

Table 6.1. Data matrix.

A. Surface Field Measurements, (A).

$\phi \backslash D$	1.5 A	2.0 A	5.0 A
0°	CYL1S	CYL2S	CYL3S
90°	CYL4S	CYL5S	CYL6S
180°	CYL7S	CYL8S	CYL9S

B. Interior Coupled-Field Measurements, (B).

$\phi \backslash D$	1.5 A	2.0 A	5.0 A
0°	CYL1I	CYL2I	CYL3I
90°	CYL4I	CYL5I	CYL6I
180°	CYL7I	CYL8I	CYL9I

C. Transfer Coefficients, (B/A) x 1000

$\phi \backslash D$	1.5 A	2.0 A	5.0 A
0°	CYL1IS	CYL2IS	CYL3IS
90°	CYL4IS	CYL5IS	CYL6IS
180°	CYL7IS	CYL8IS	CYL9IS

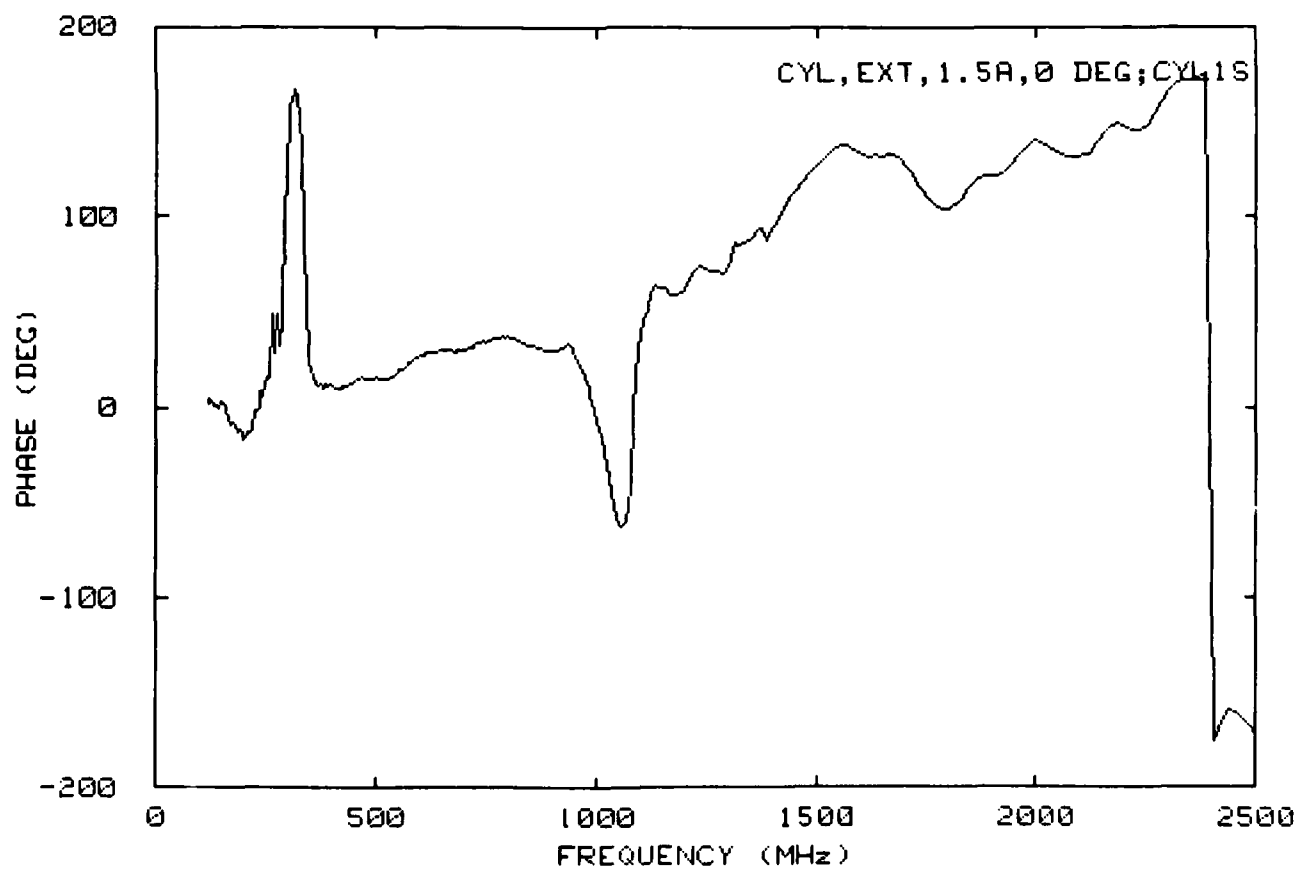
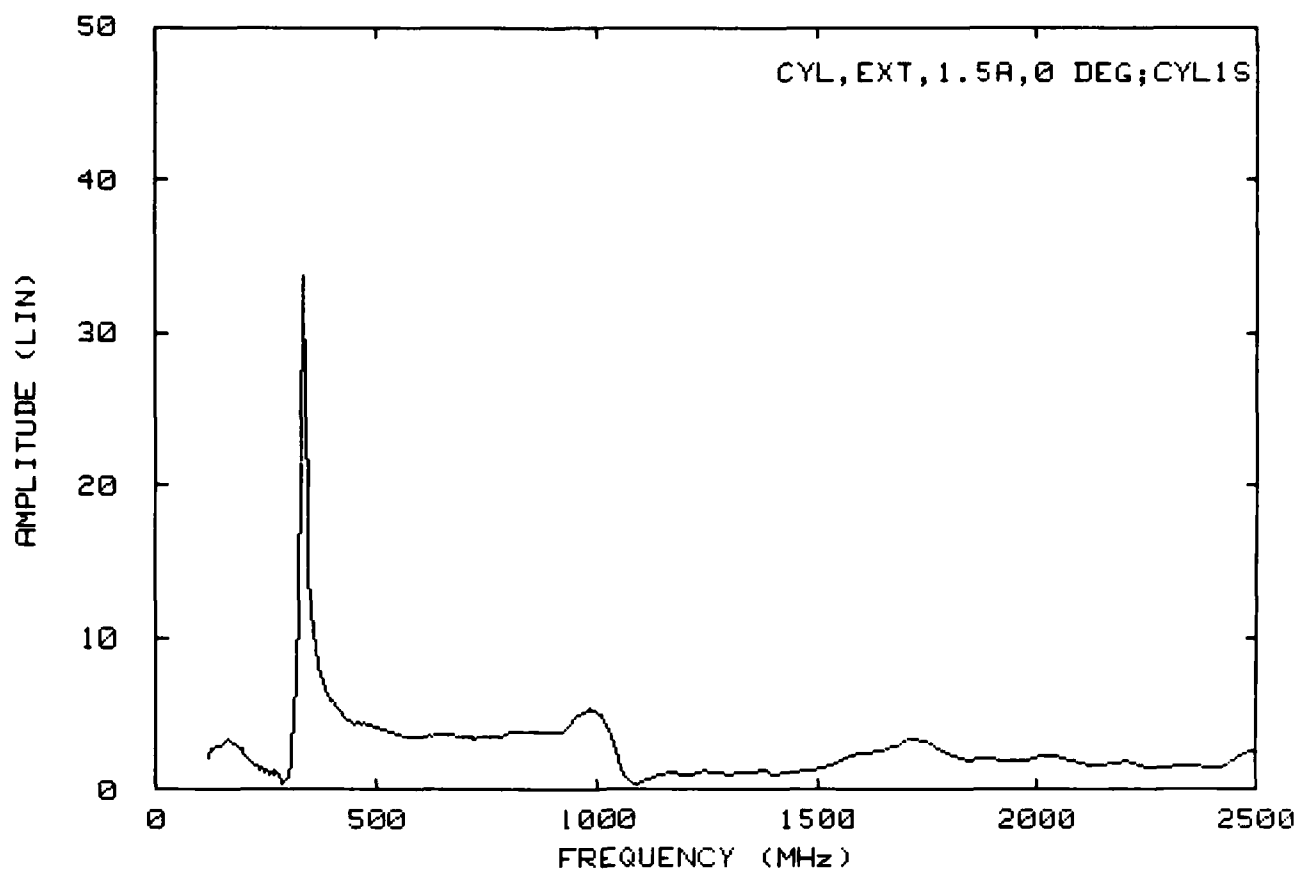


Figure 6.1. Surface field measurement at $\phi = 0^\circ$, $D = 1.5$ A.

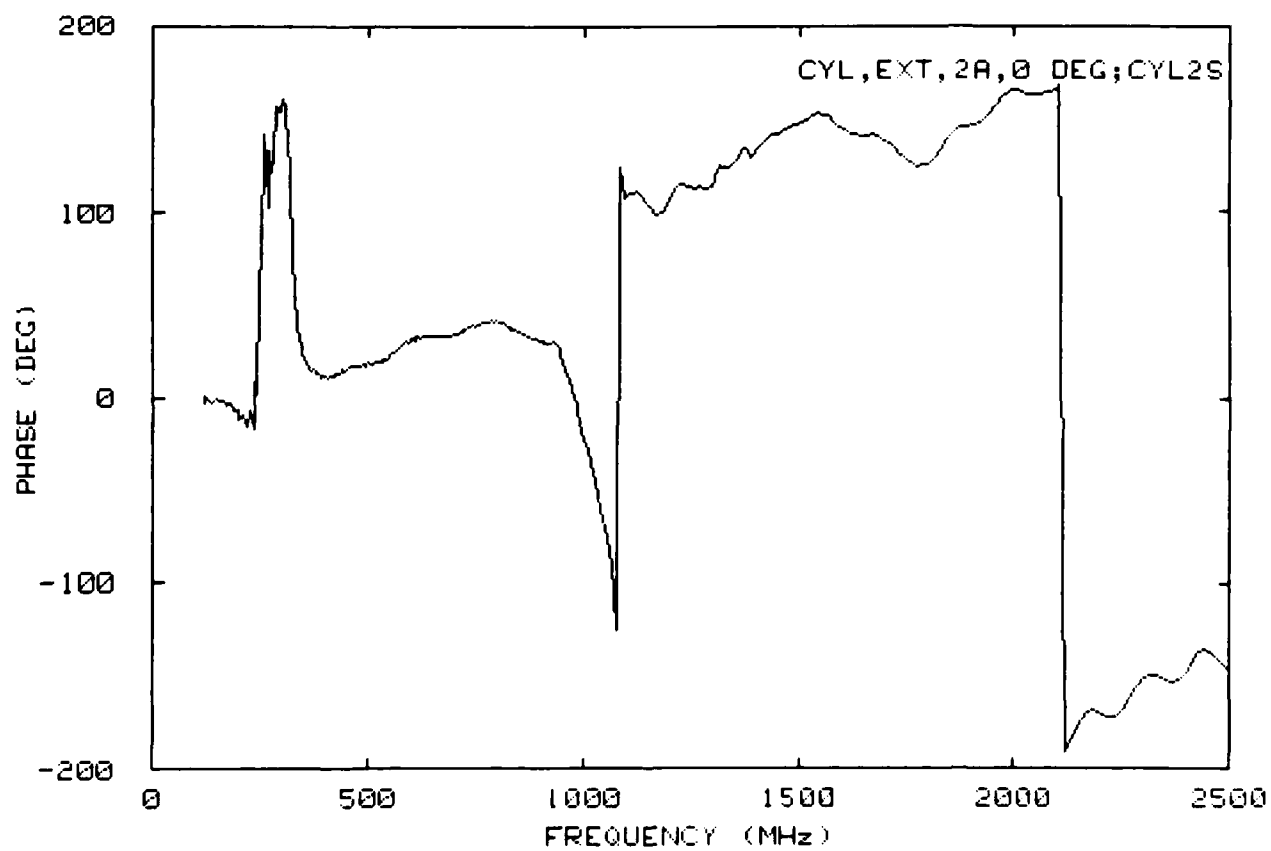
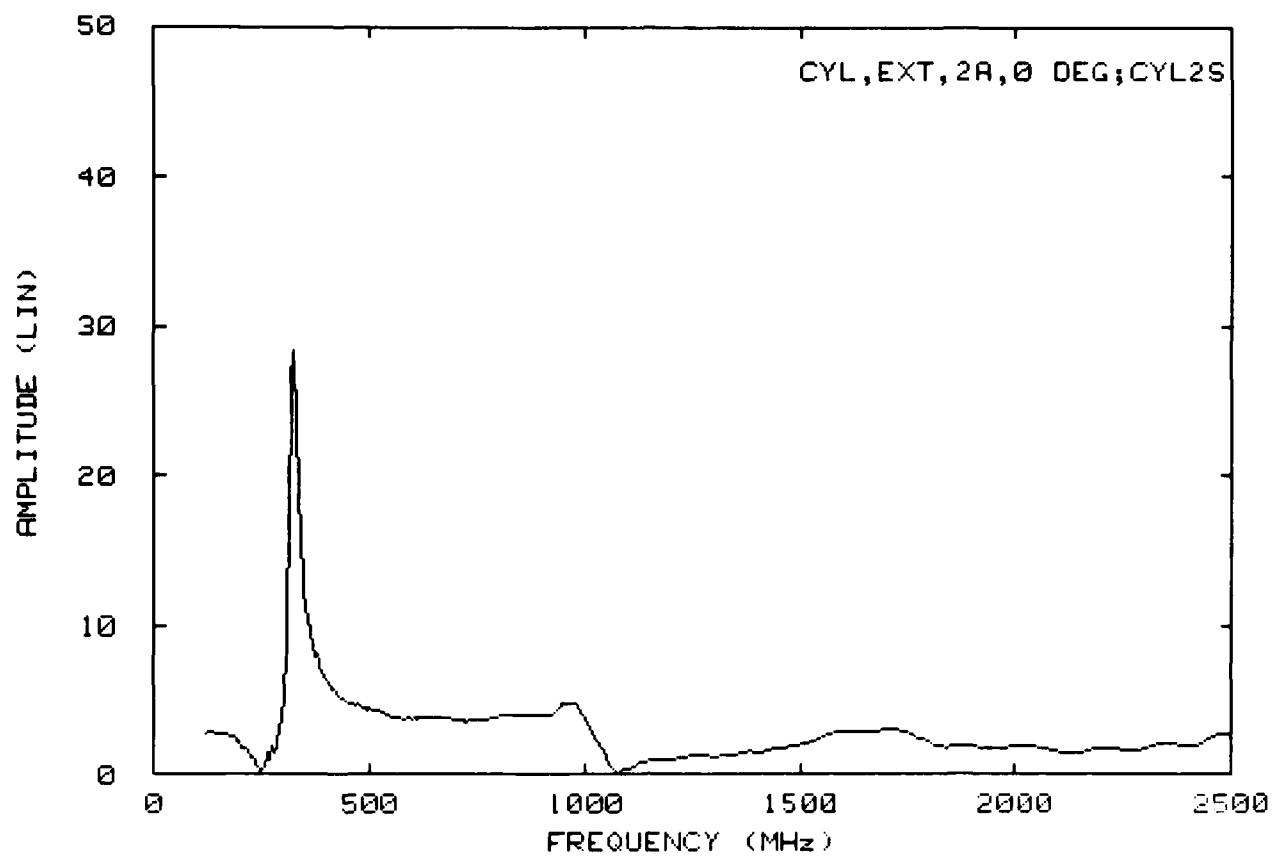


Figure 6.2. Surface field measurement at $\phi = 0^\circ$, $D = 2.0$ A.

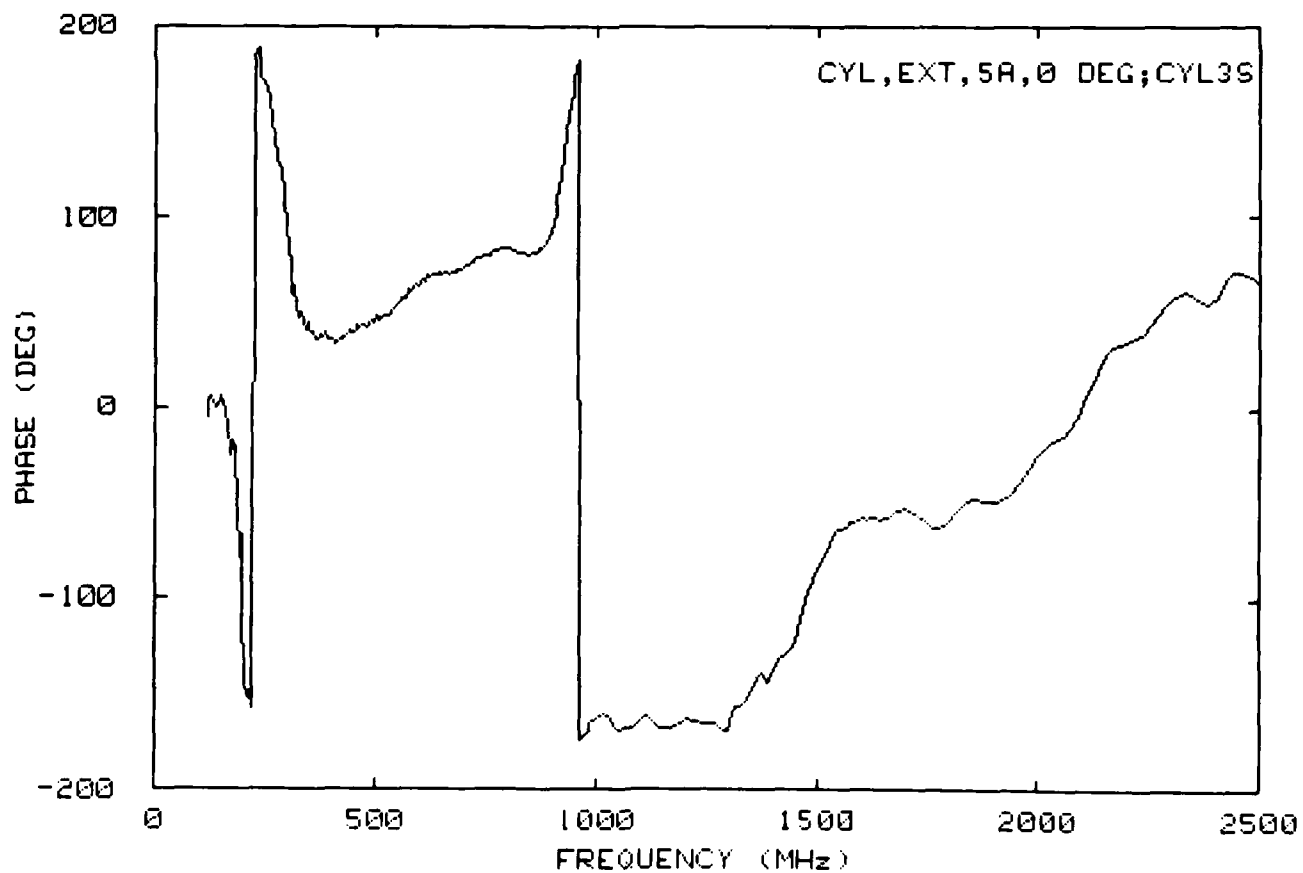
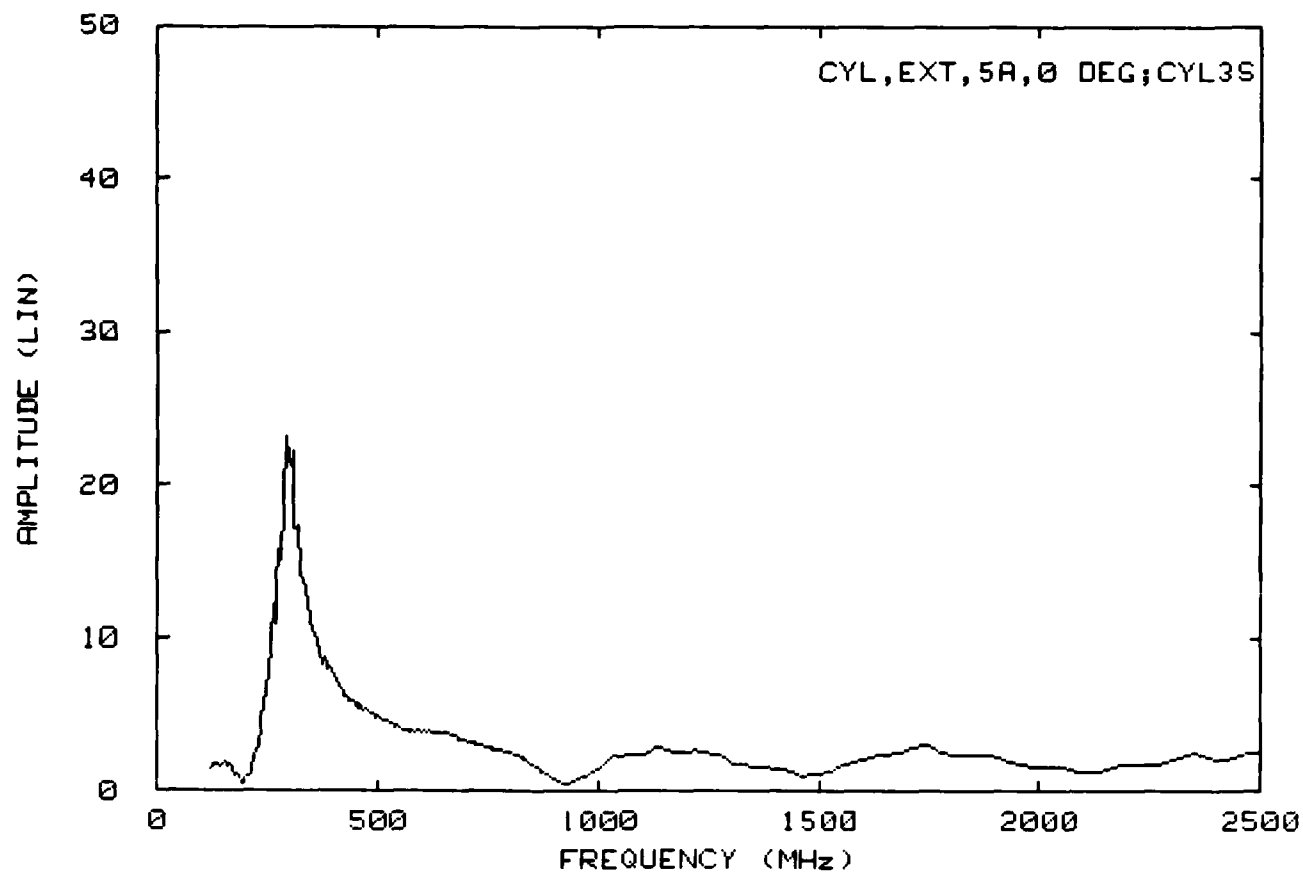


Figure 6.3. Surface field measurement at $\phi = 0^\circ$, $D = 5.0$ A.

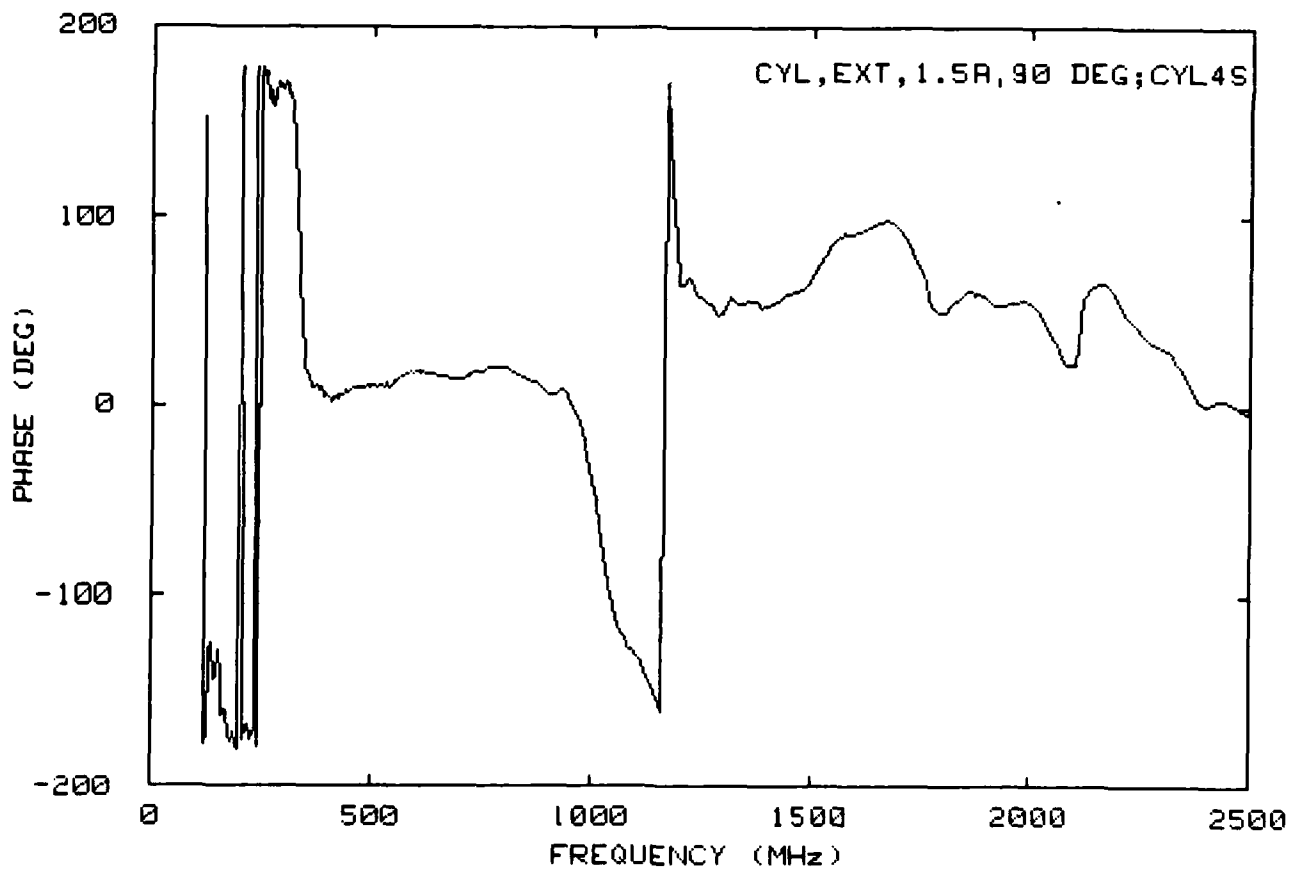
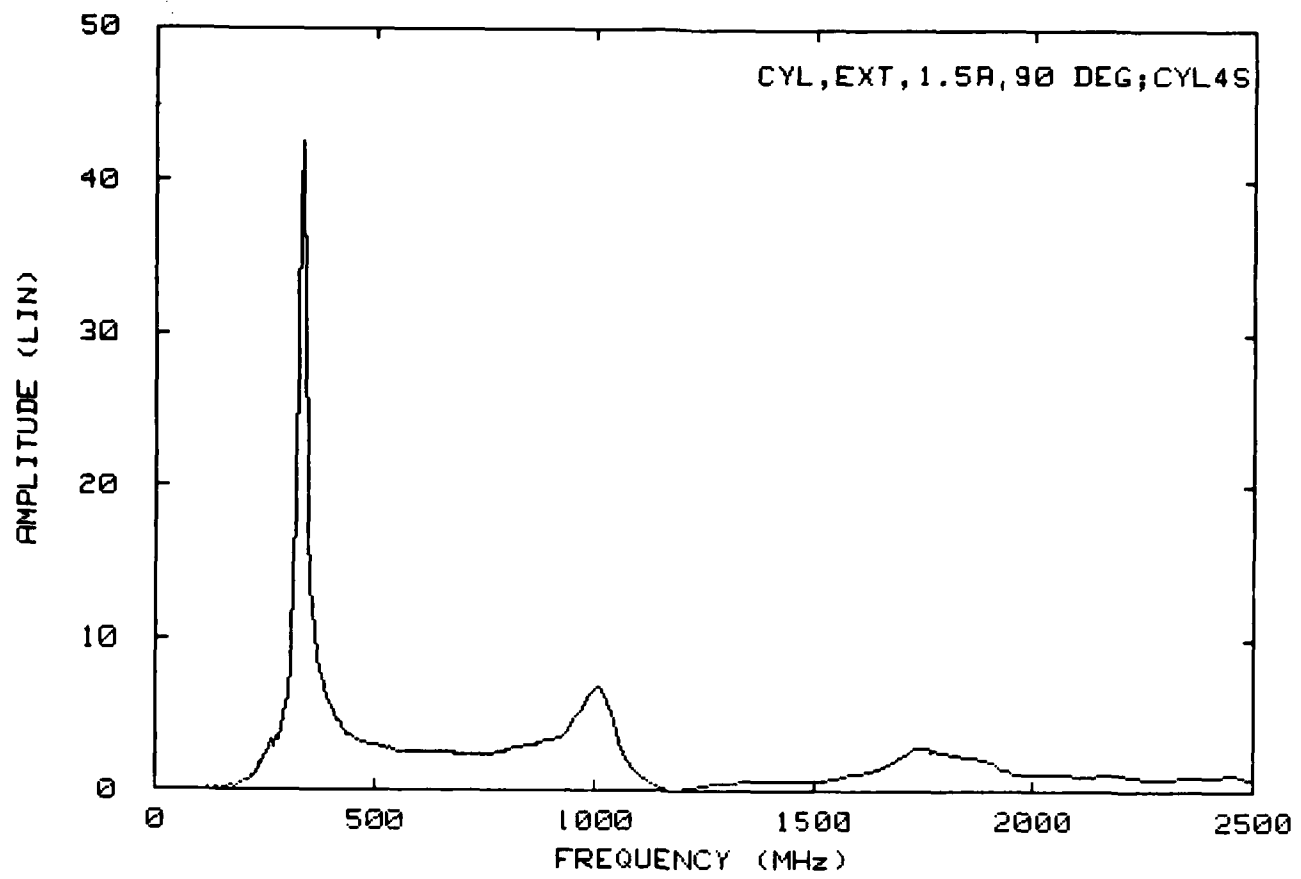


Figure 6.4. Surface field measurement at $\phi = 90^\circ$, $D = 1.5$ A.

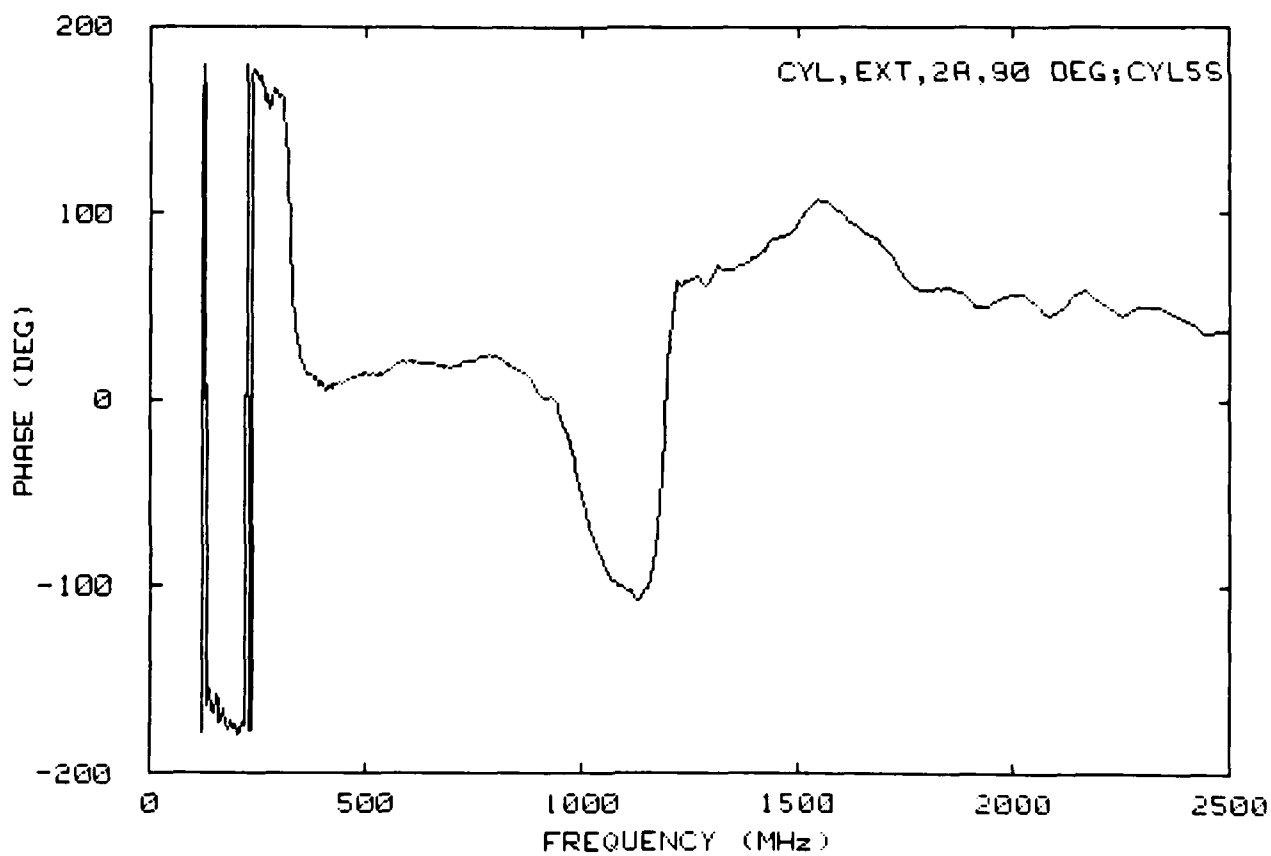
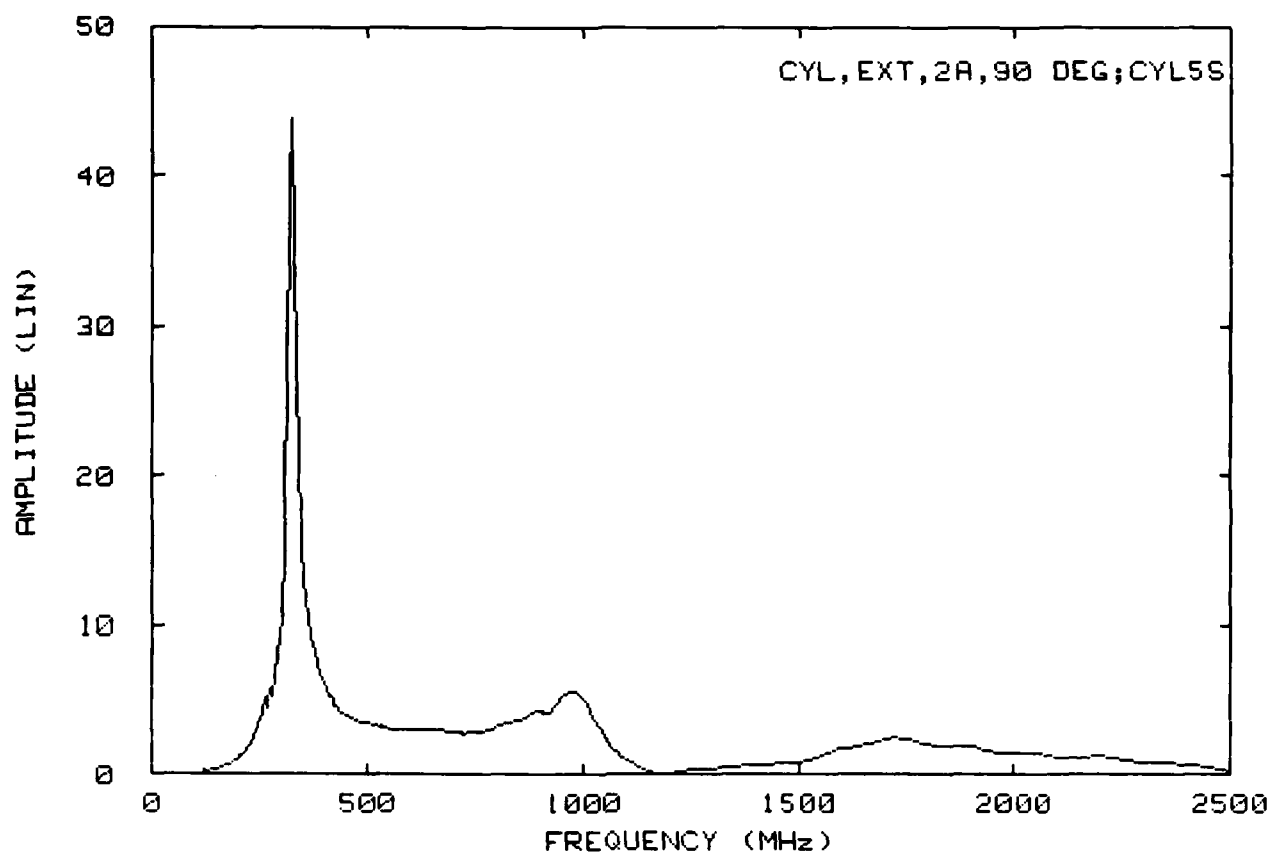


Figure 6.5. Surface field measurement at $\phi = 90^\circ$, $D = 2.0$ A.

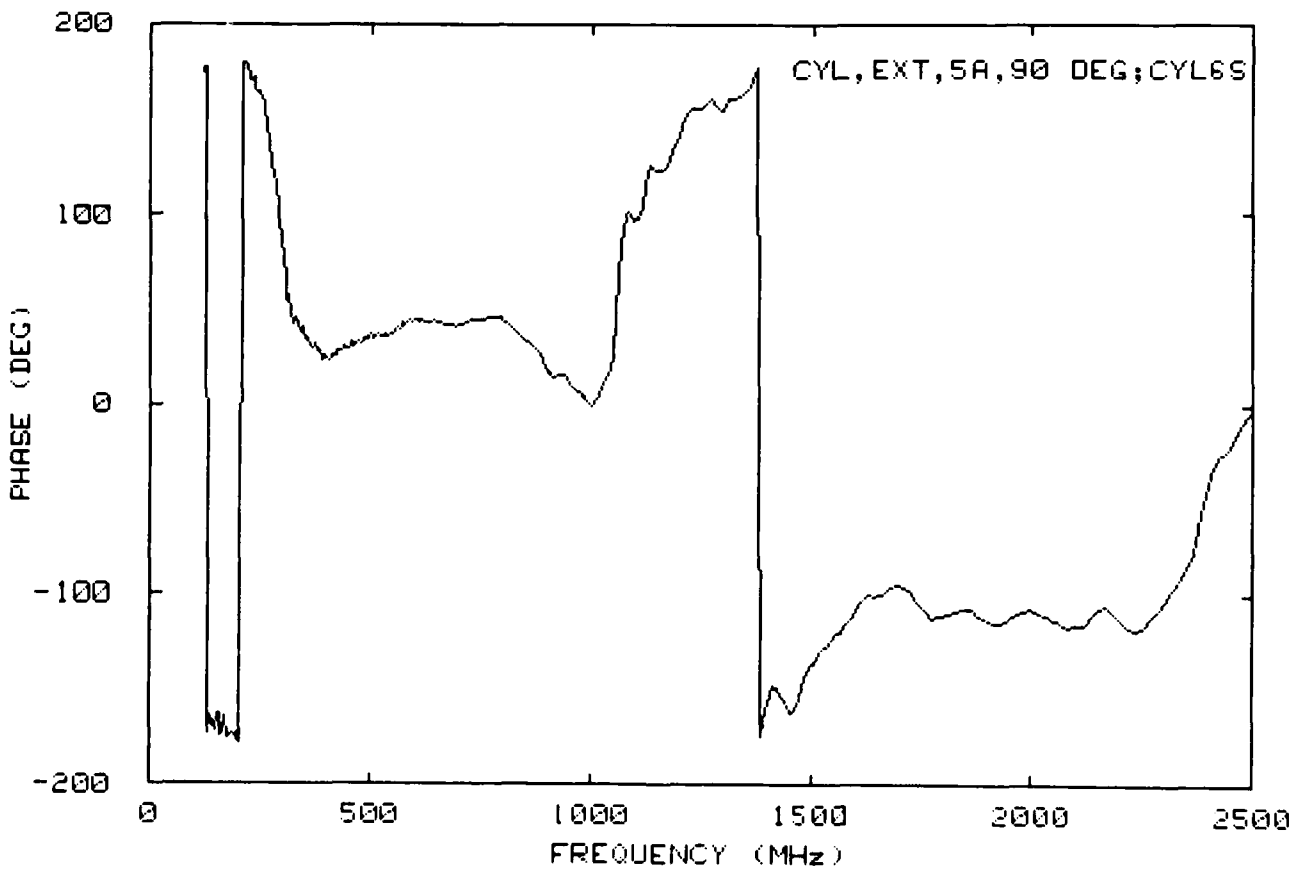
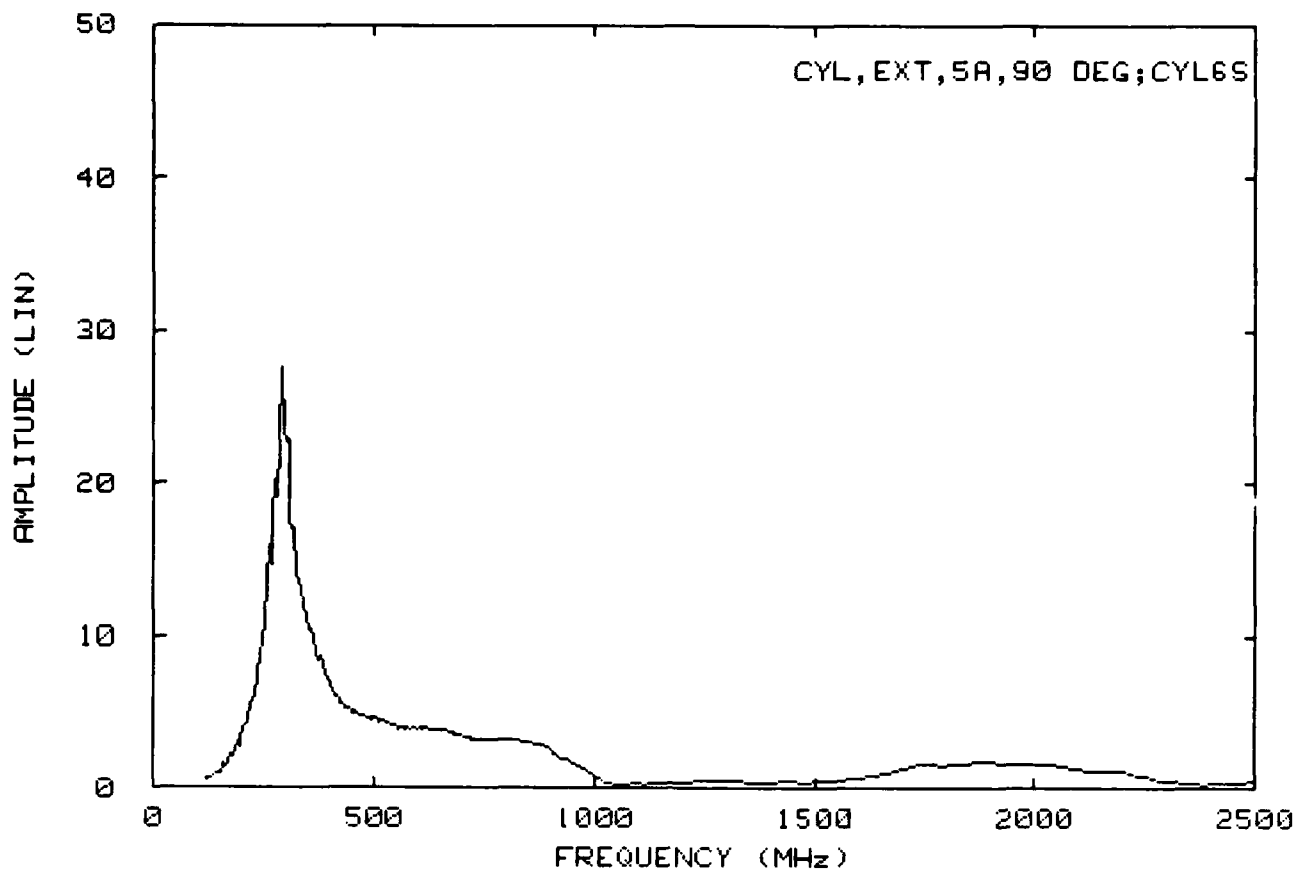


Figure 6.6. Surface field measurement at $\phi = 90^\circ$, $D = 5.0$ A.

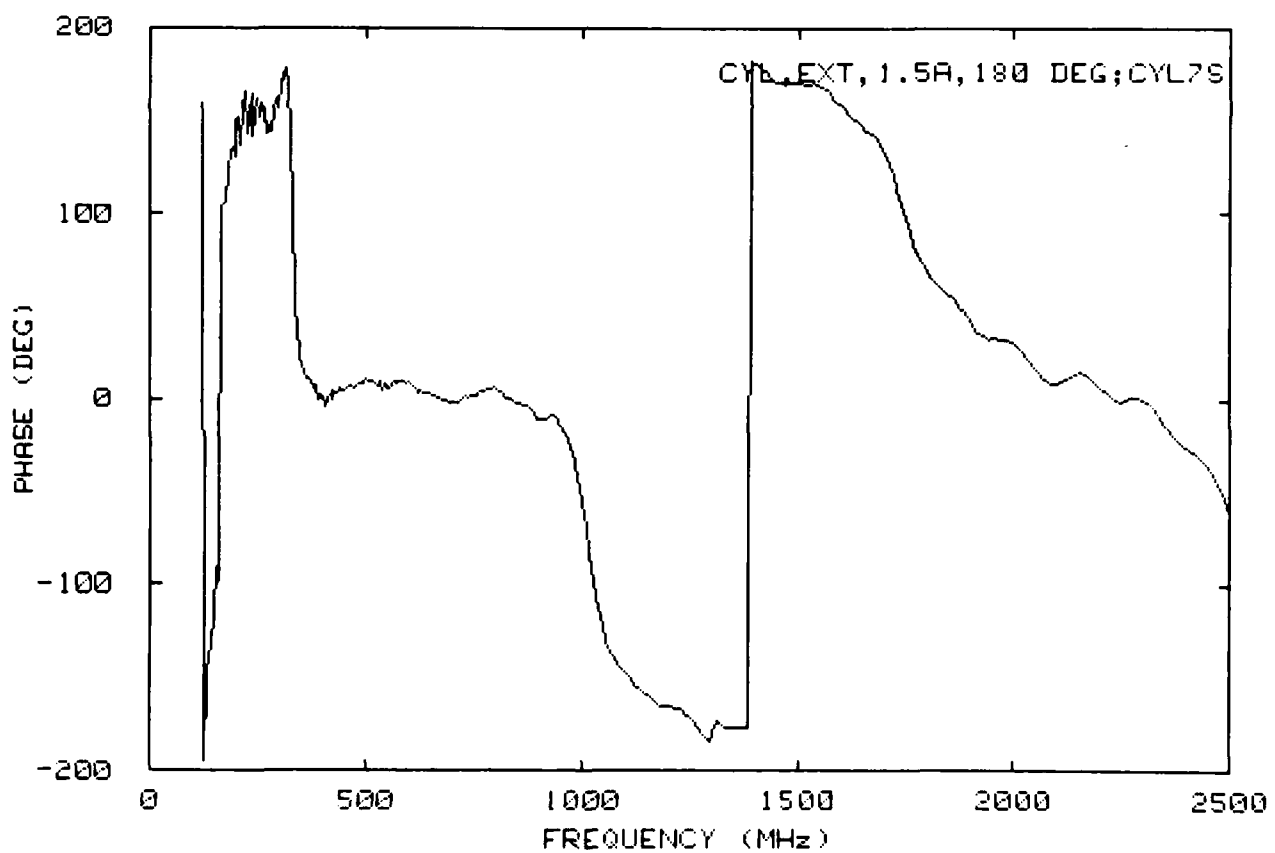
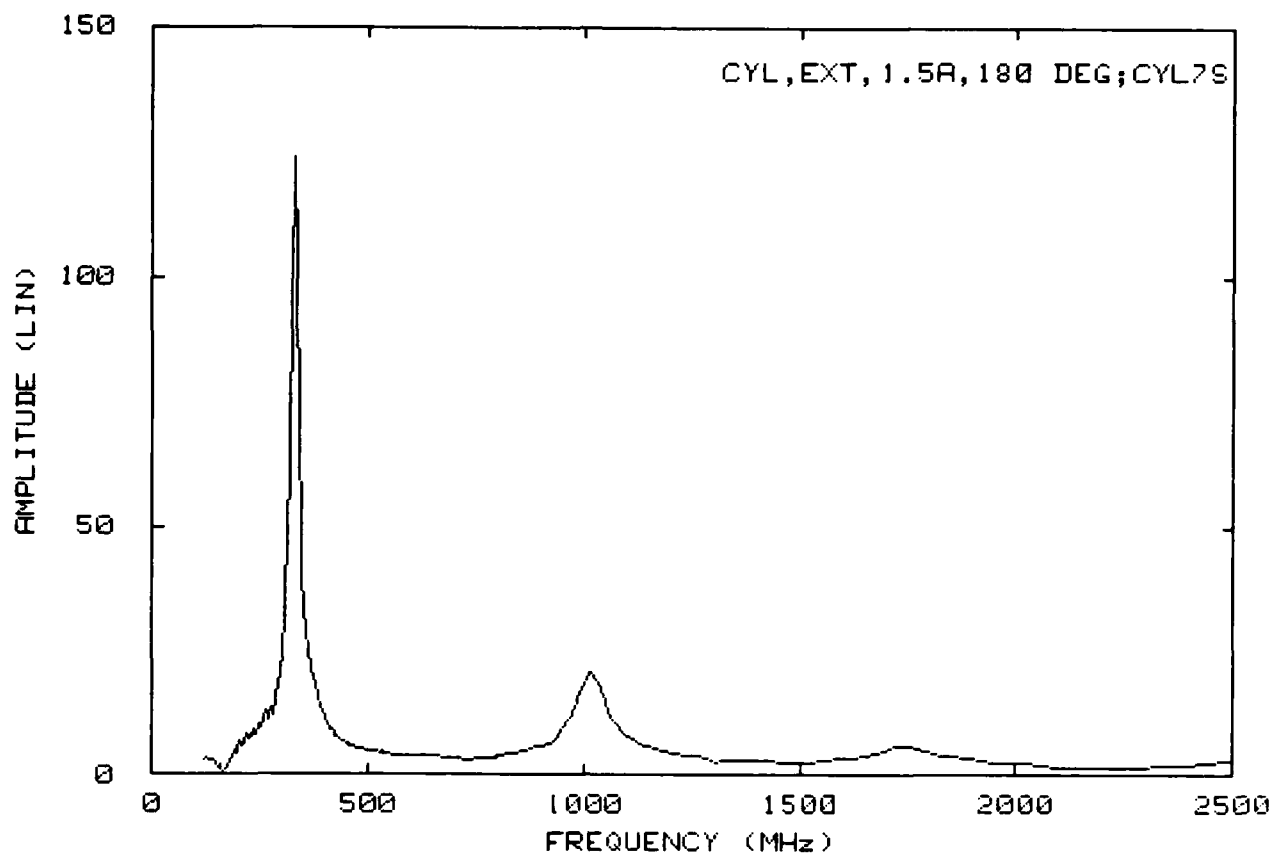


Figure 6.7. Surface field measurement at $\phi = 180^\circ$, $D = 1.5$ A.

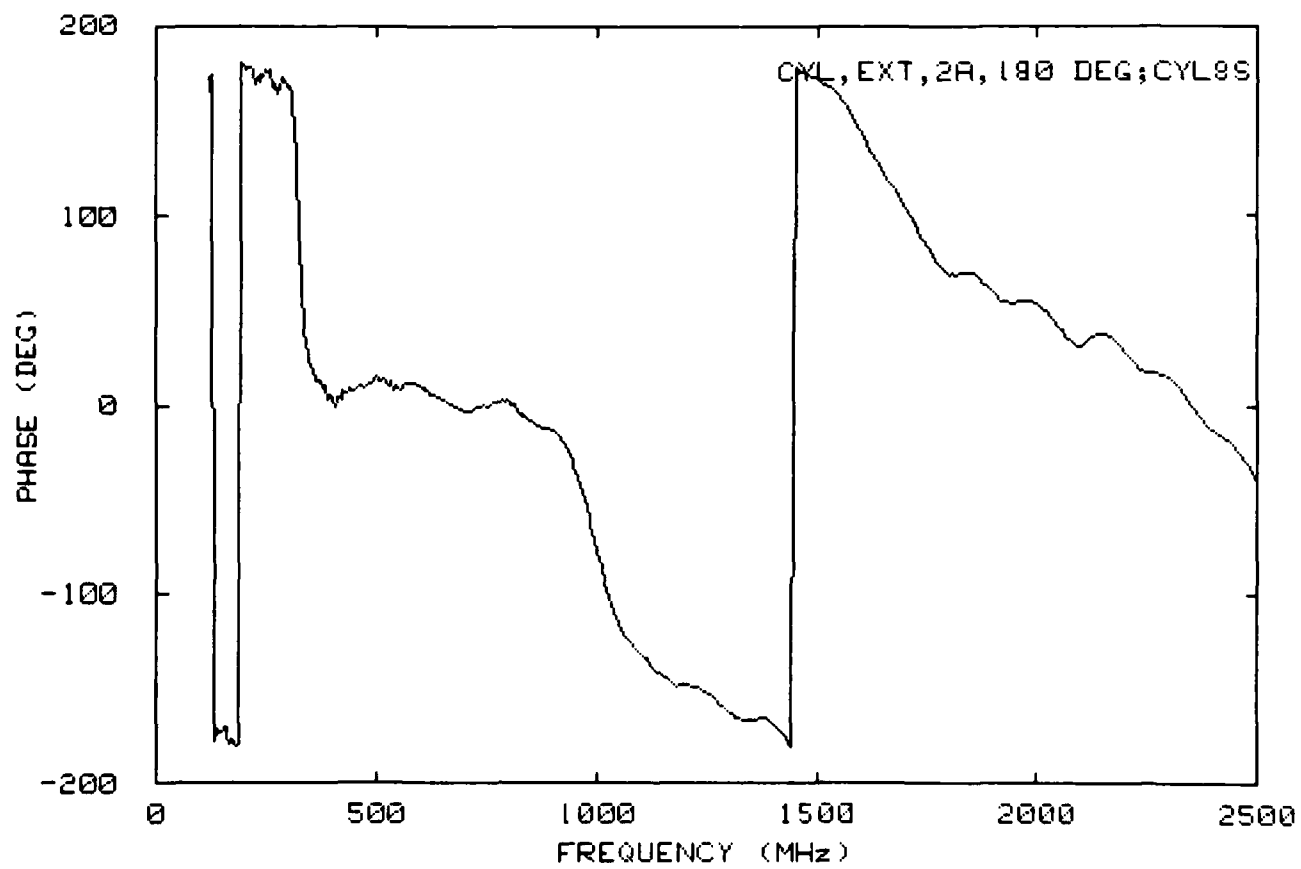
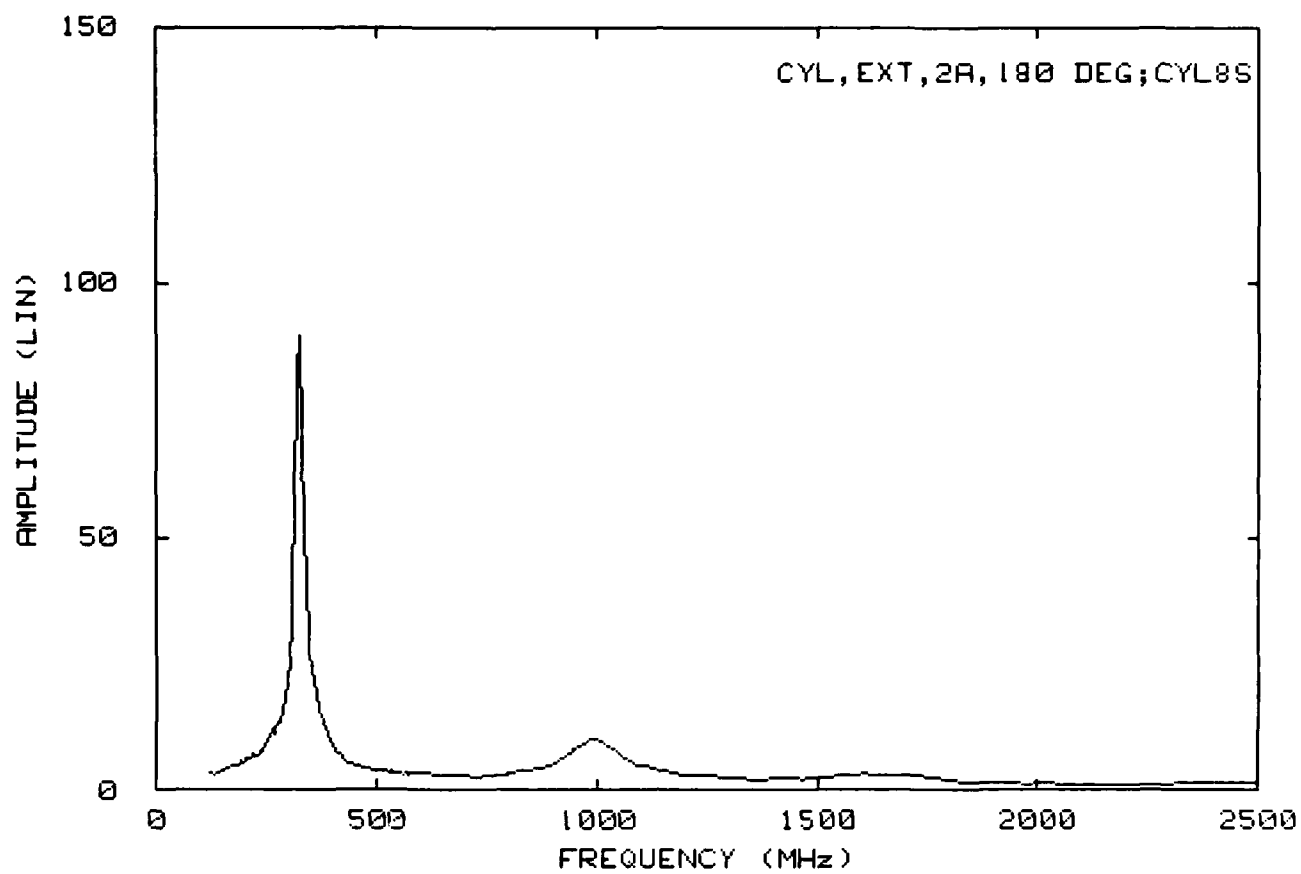


Figure 6.8. Surface field measurement at $\phi = 180^\circ$, $D = 2.0$ A.

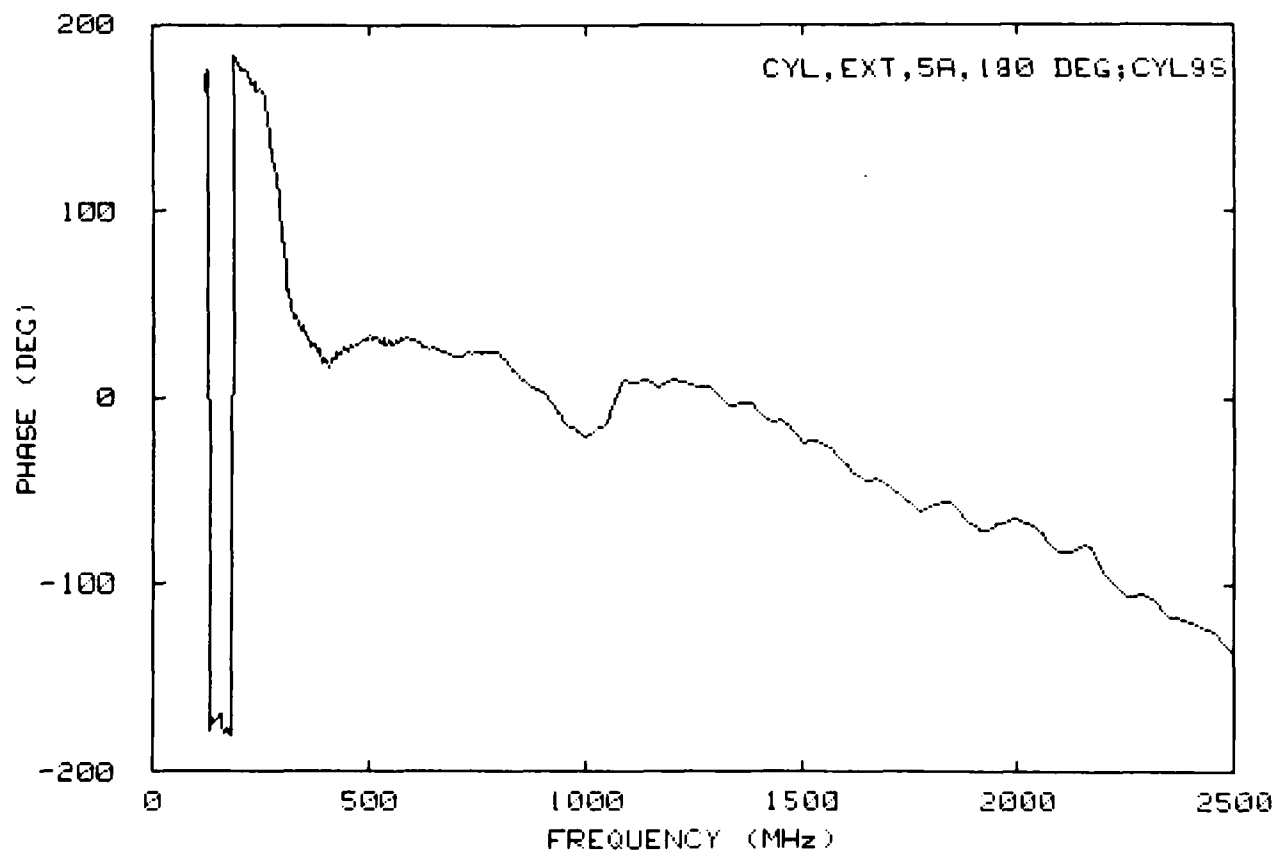
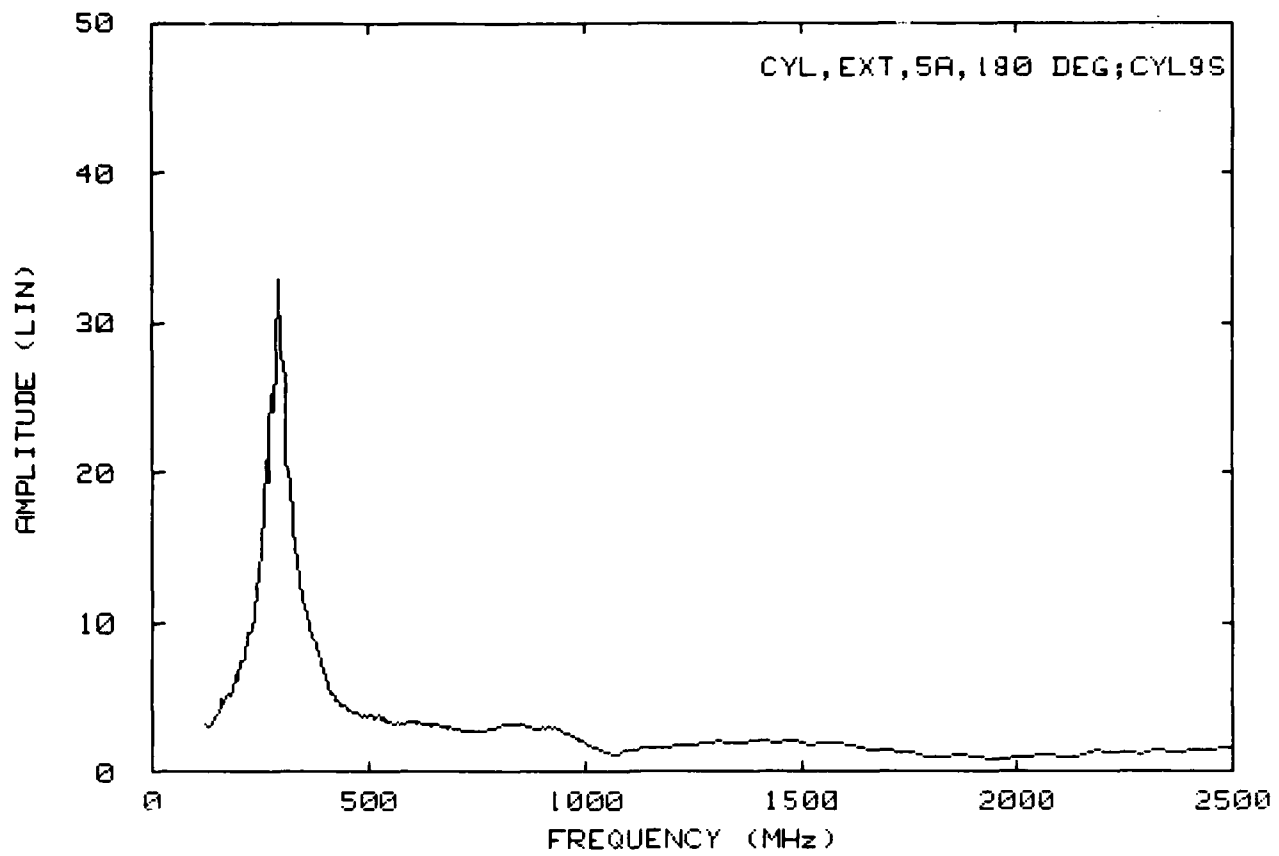


Figure 6.9. Surface field measurement at $\phi = 180^\circ$, $D = 5.0$ A.

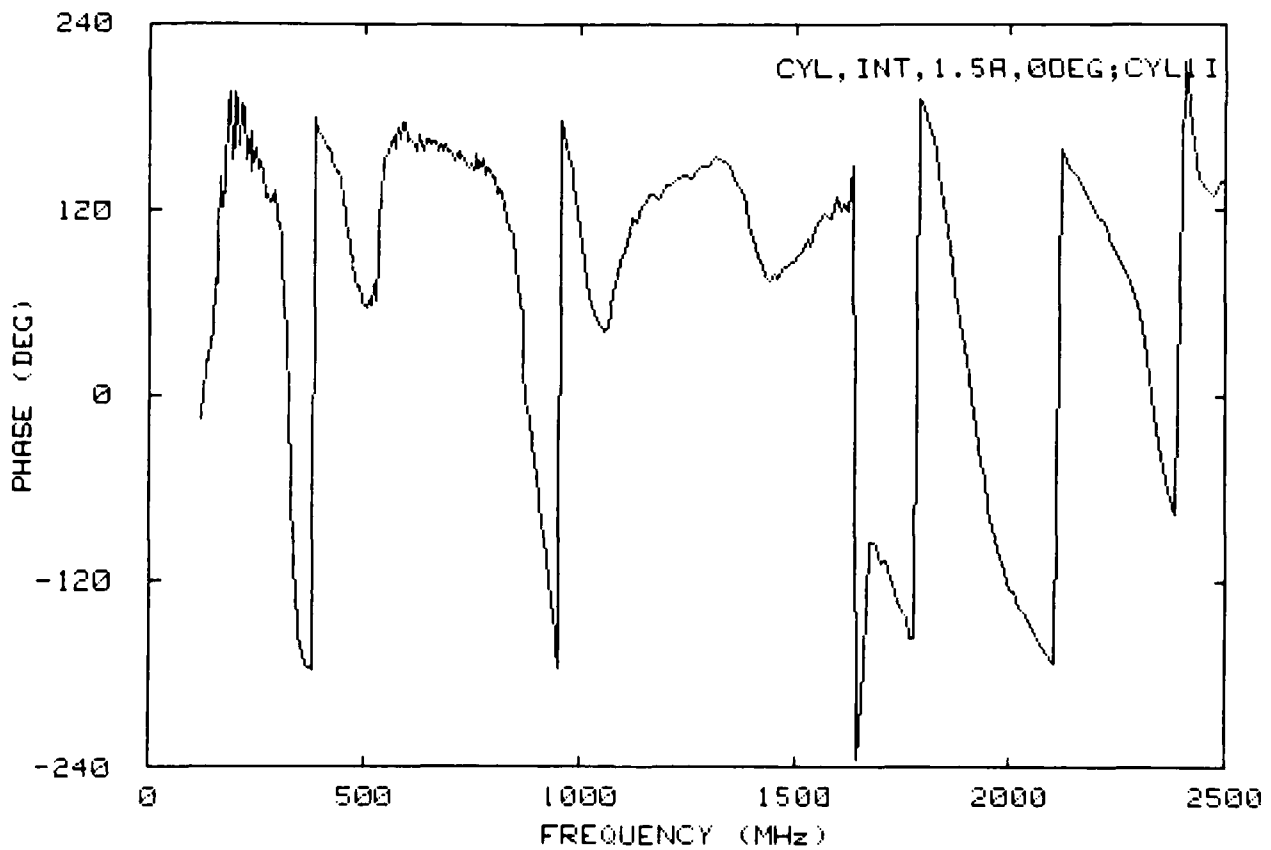
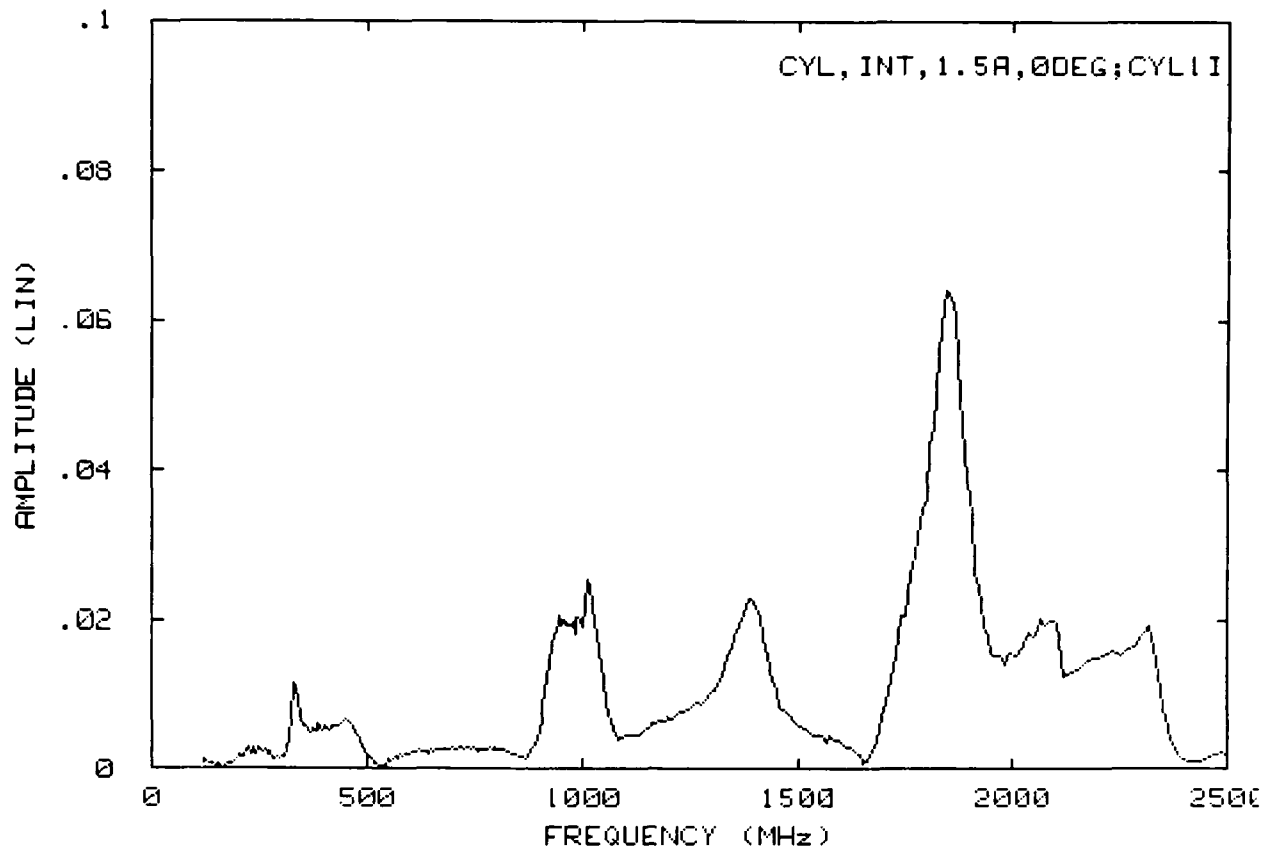


Figure 6.10. Interior coupled-field measurement at $\phi = 0^\circ$, $D = 1.5$ A.

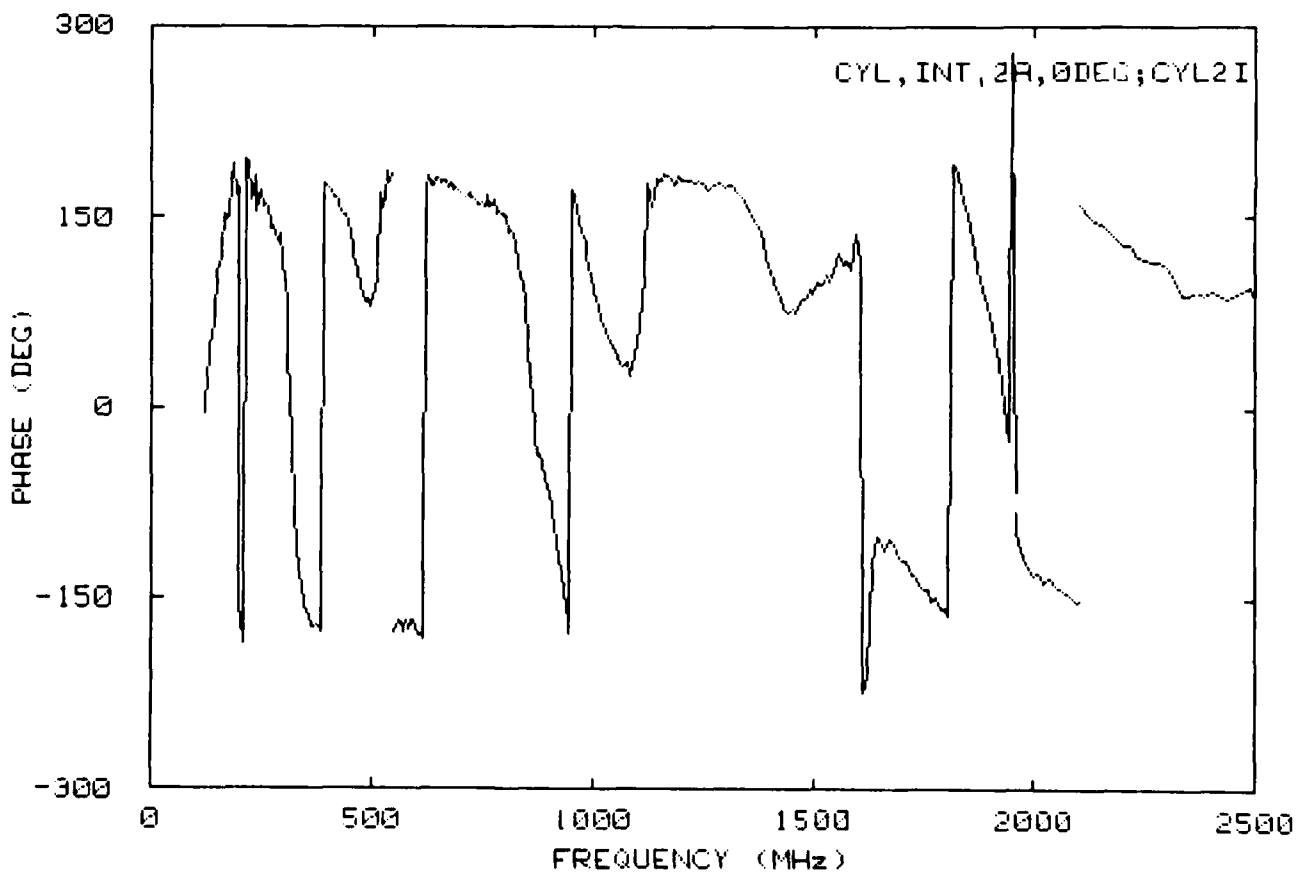
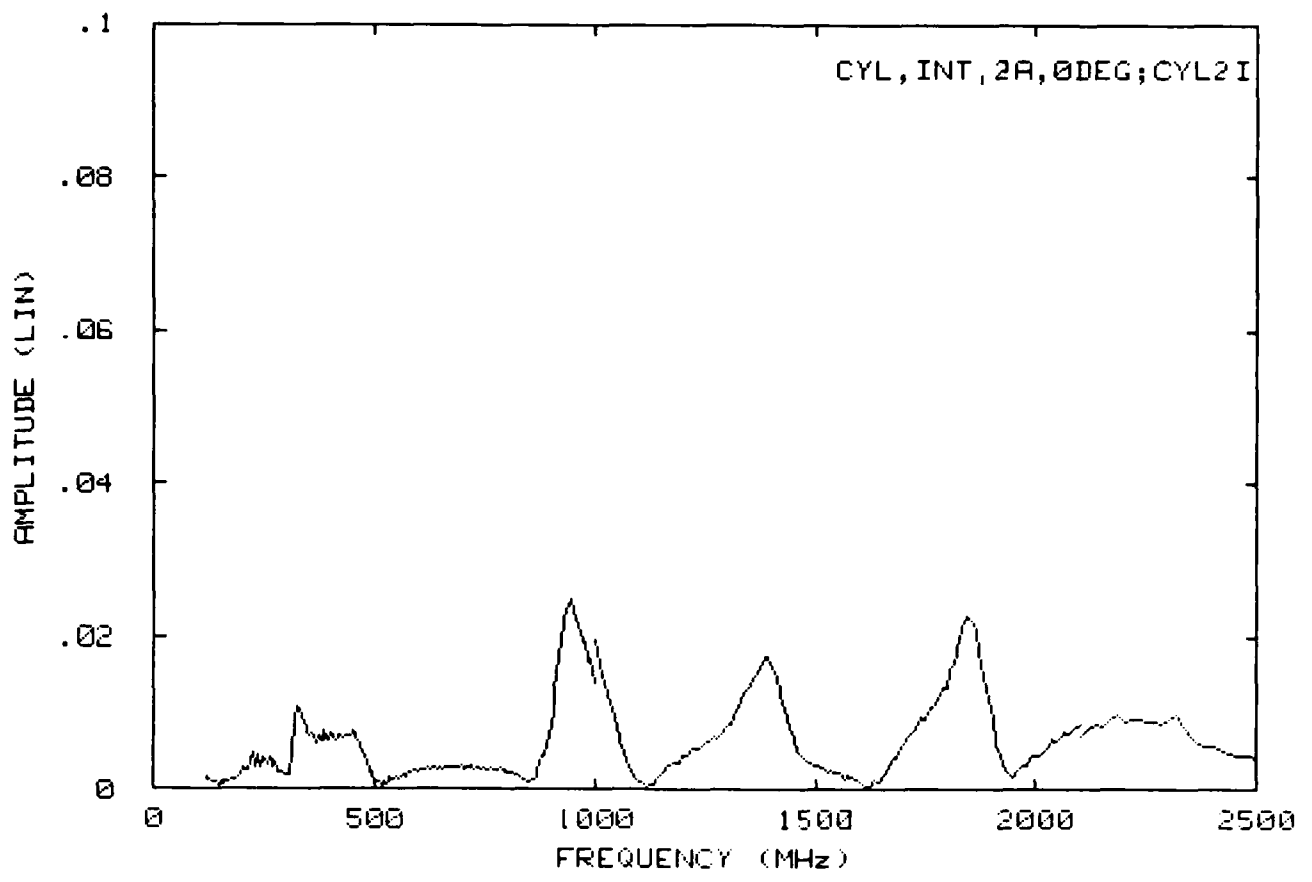


Figure 6.11. Interior coupled-field measurement at $\phi = 0^\circ$, $D = 2.0$ A.

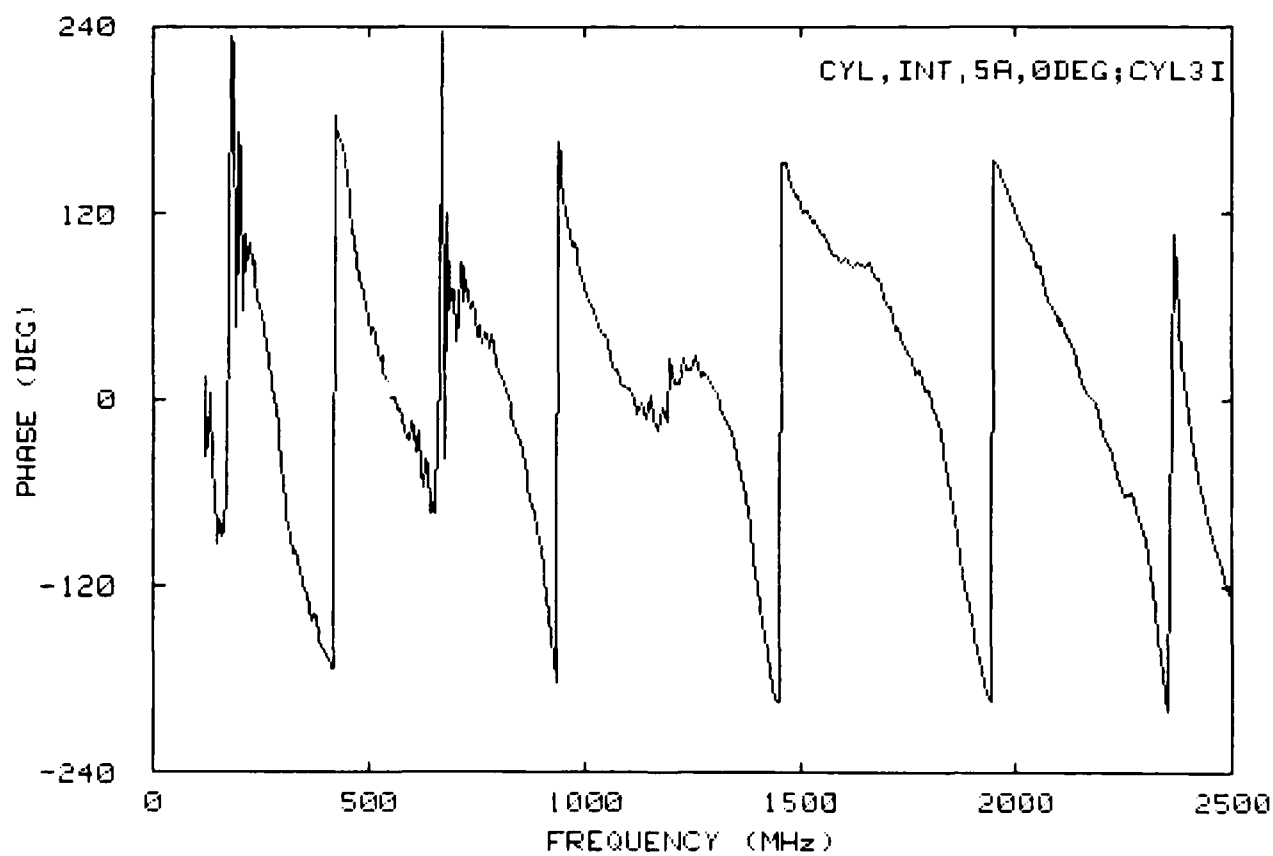
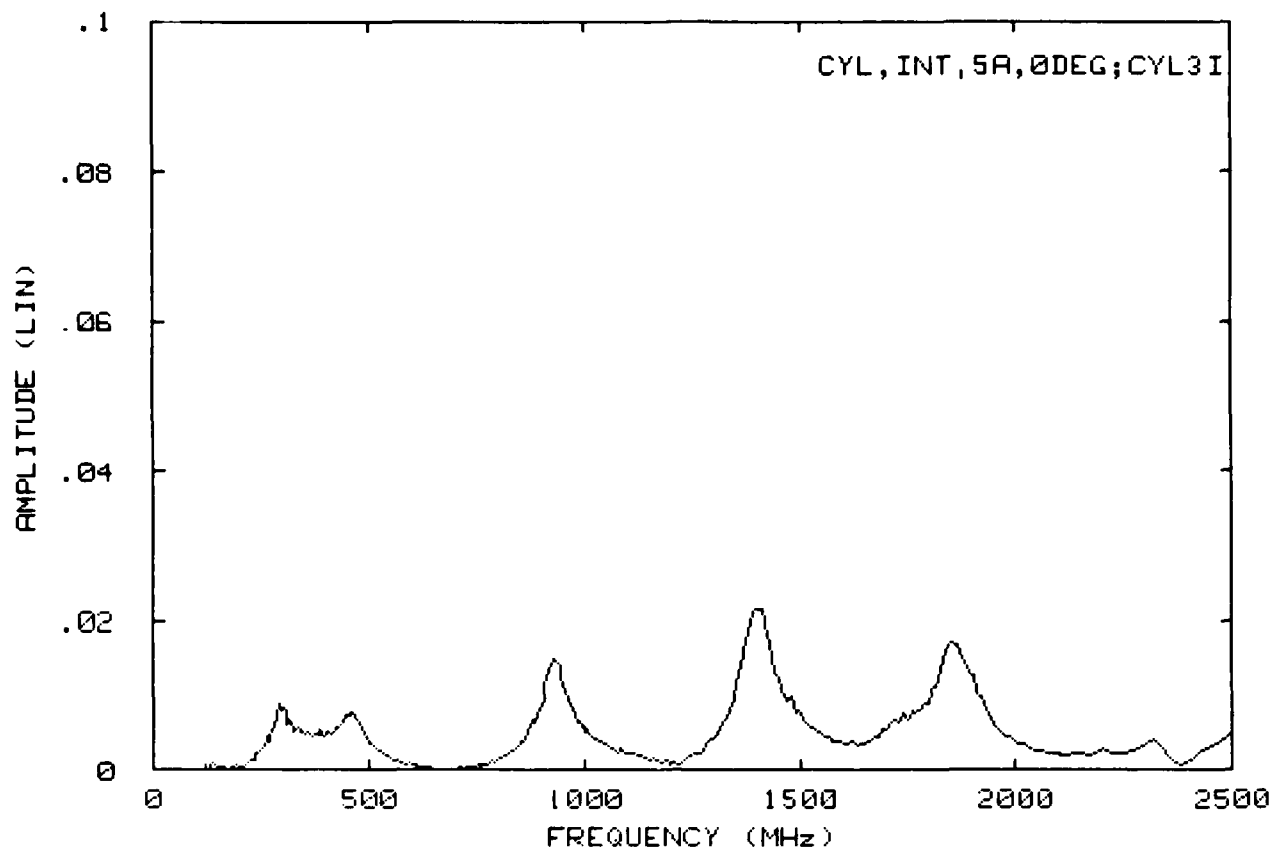


Figure 6.12. Interior coupled-field measurement at $\phi = 0^\circ$, $D = 5.0$ A.

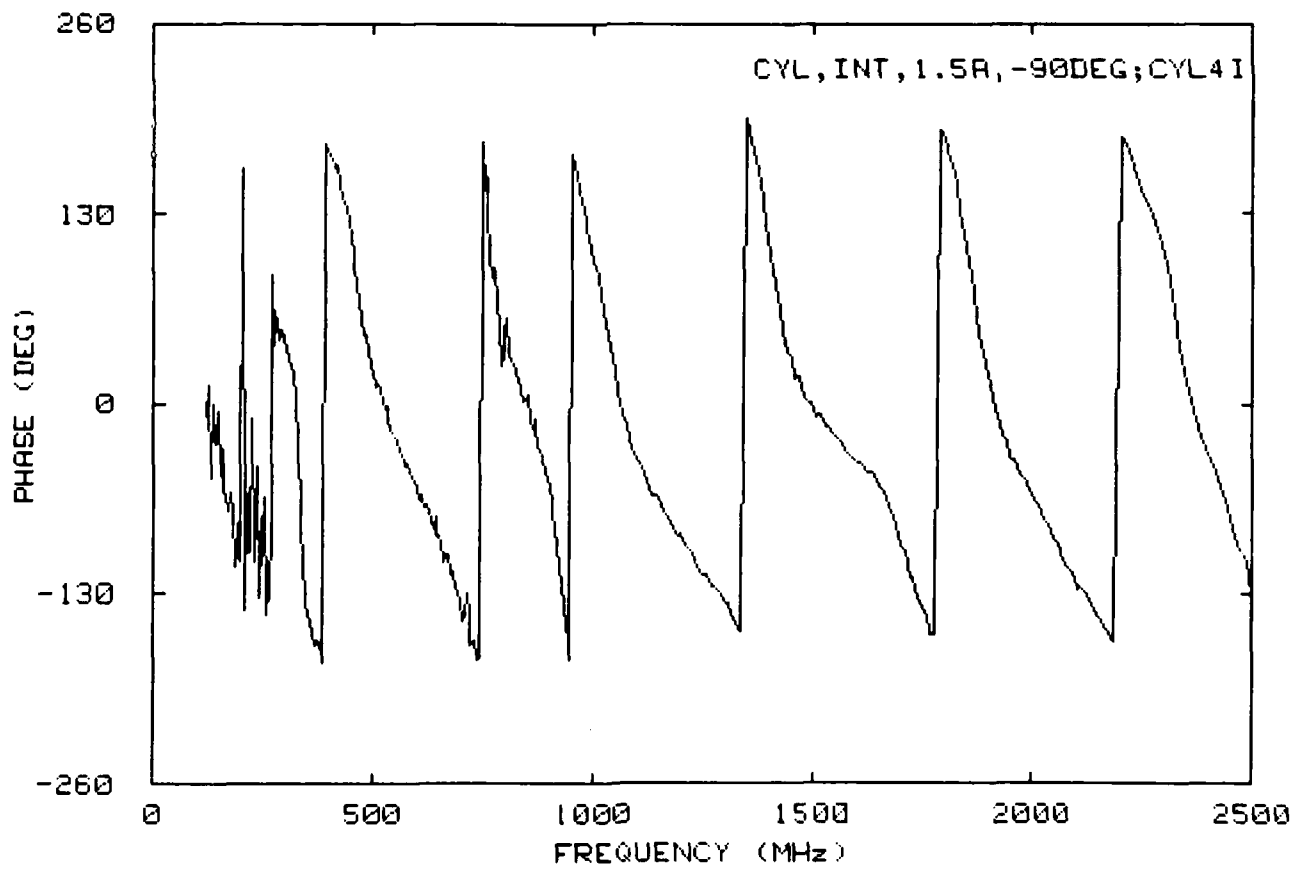
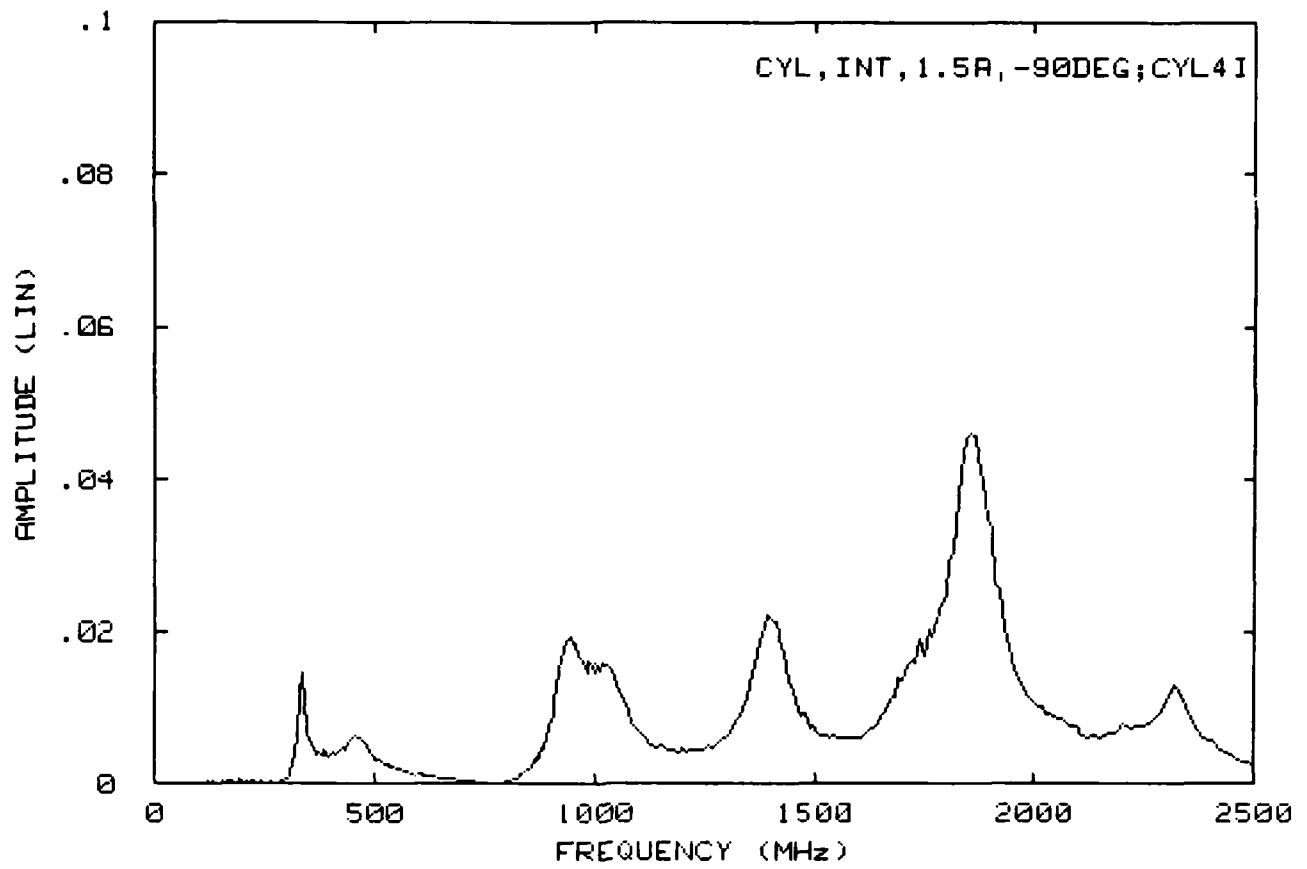


Figure 6.13. Interior coupled-field measurement at $\phi = 90^\circ$, $D = 1.5$ A.

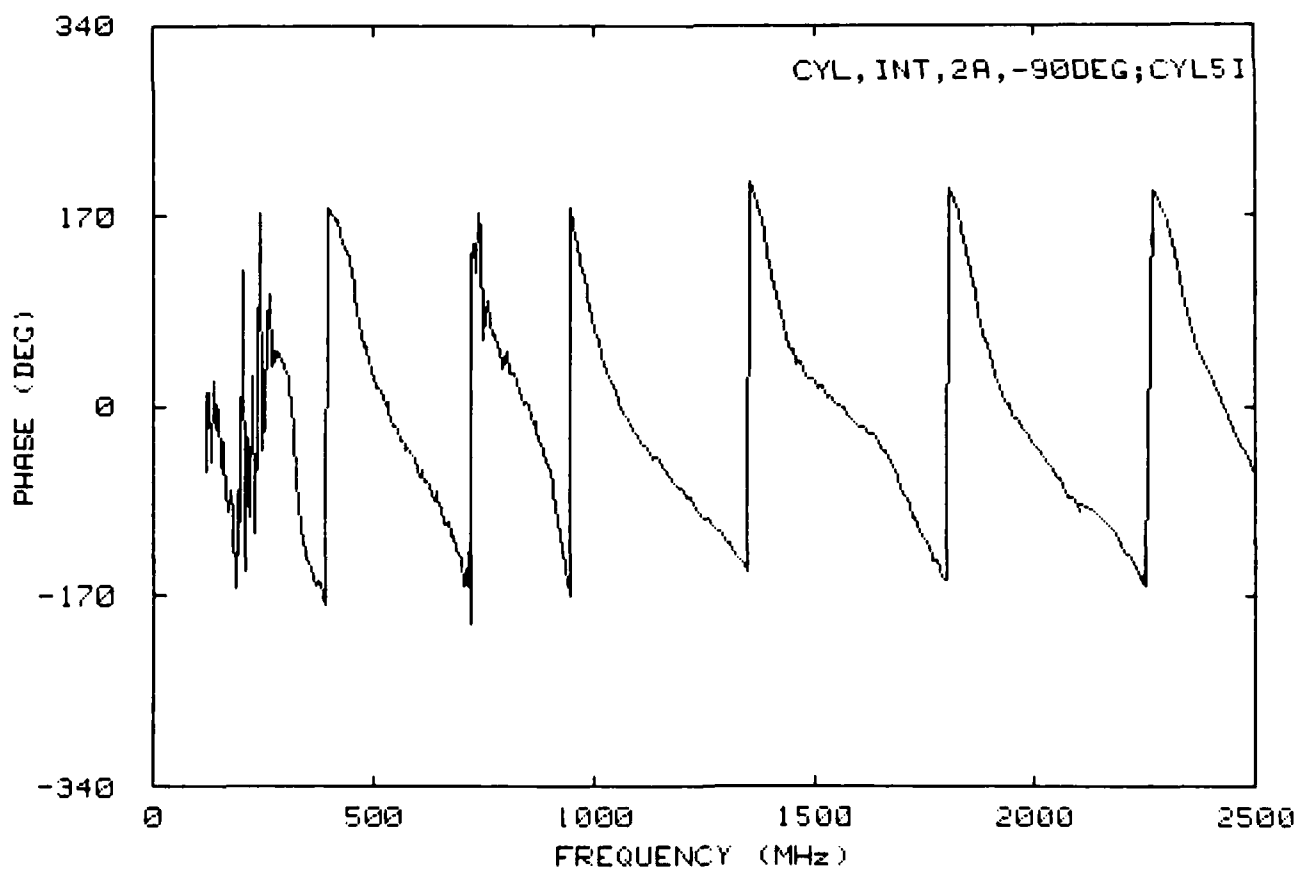
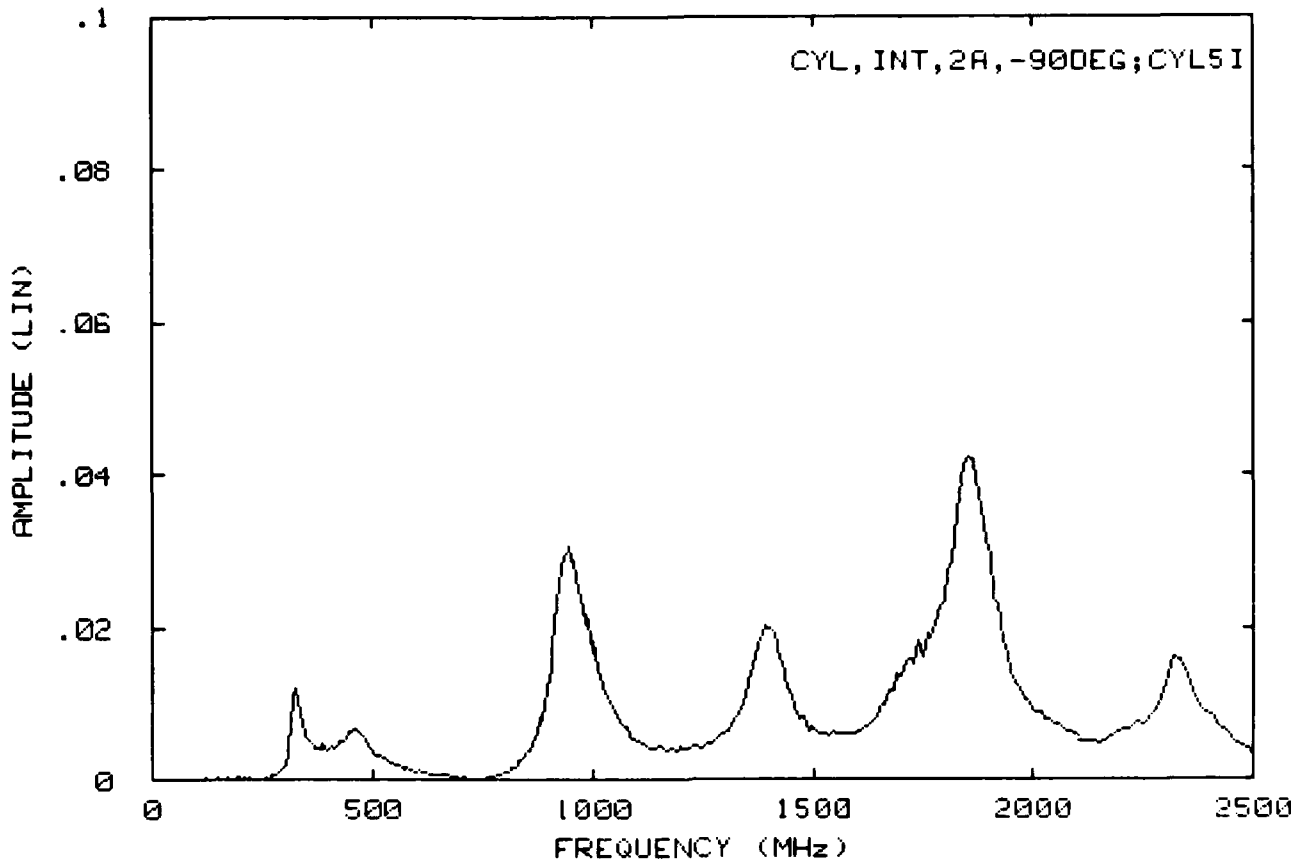


Figure 6.14. Interior coupled-field measurement at $\phi = 90^\circ$, $D = 2.0$ A.

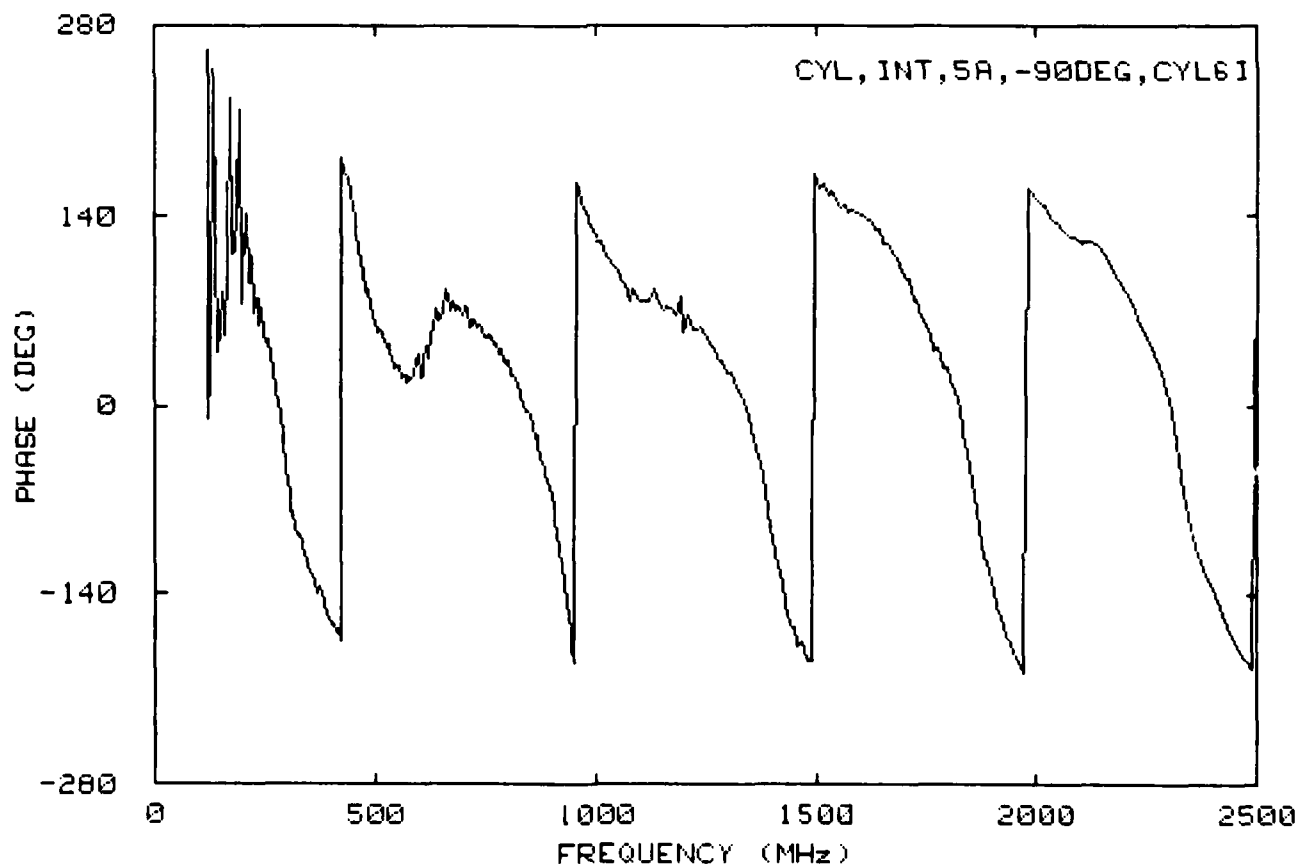
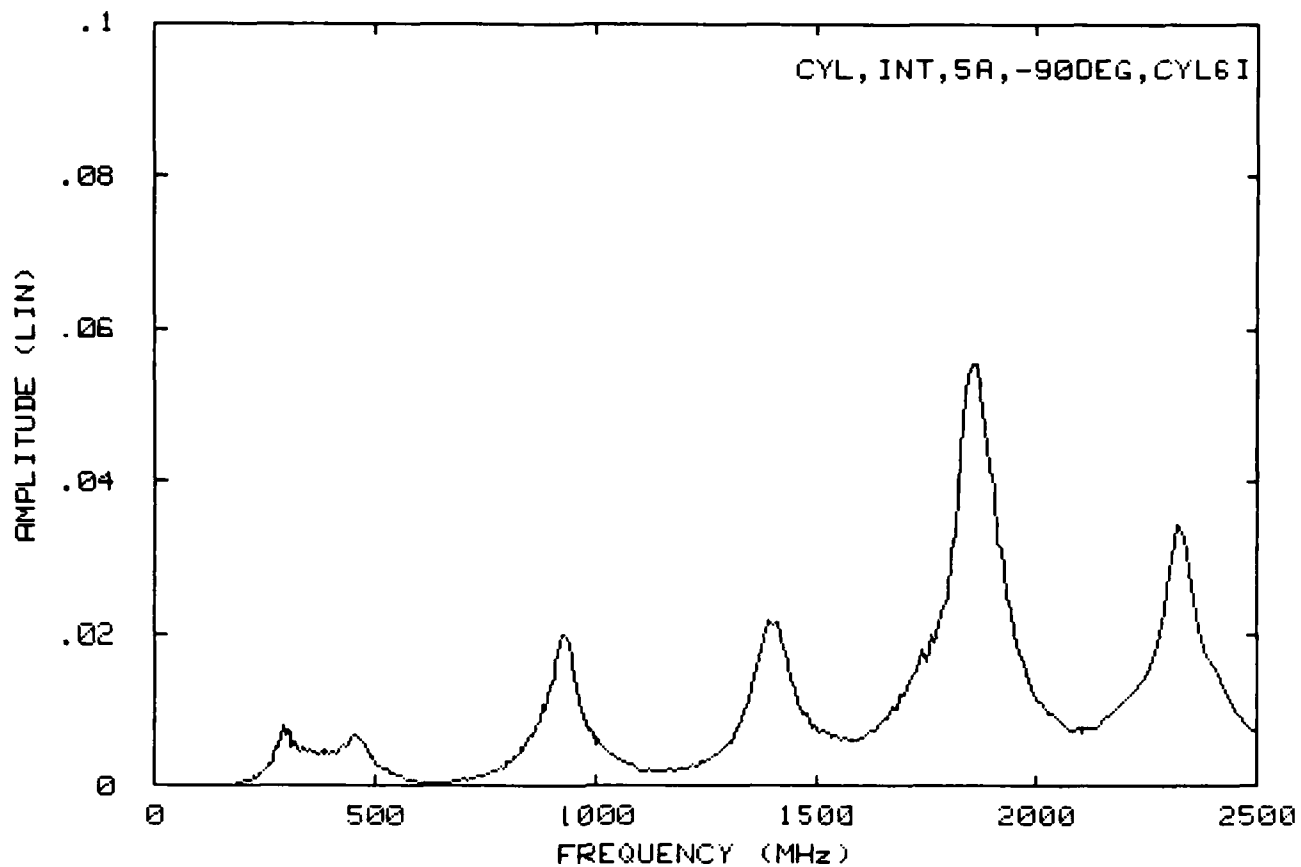


Figure 6.15. Interior coupled-field measurement at $\phi = 90^\circ$, $D = 5.0$ A.

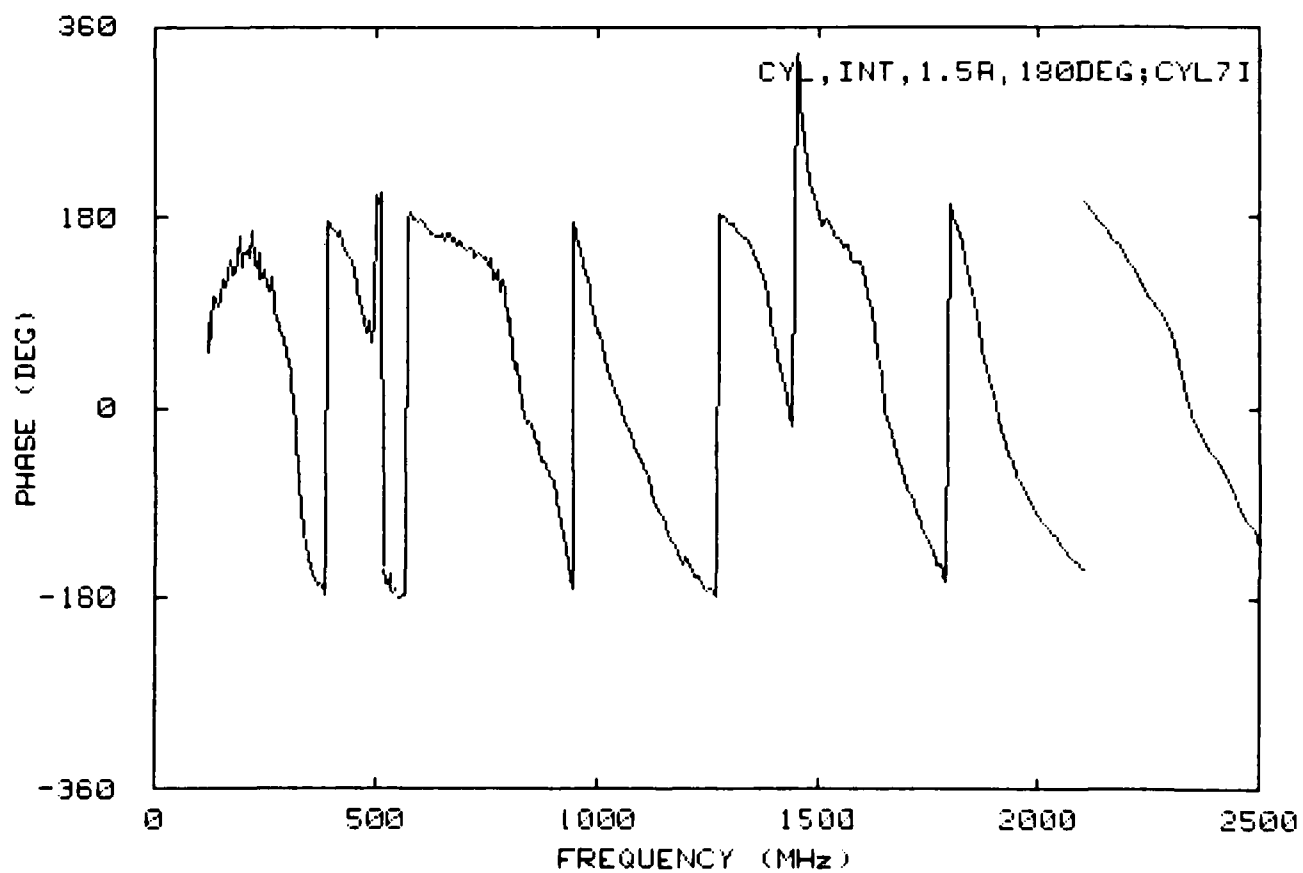
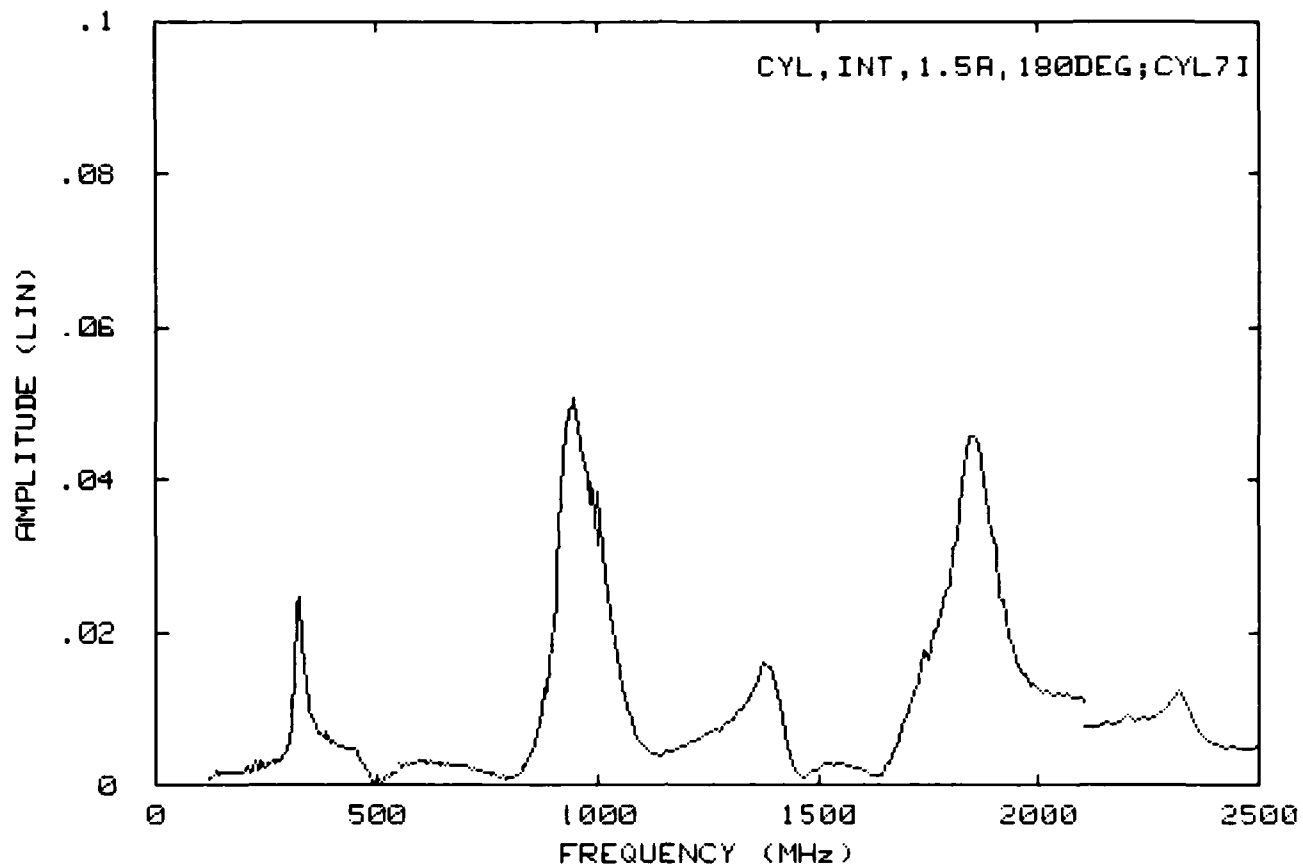


Figure 6.16. Interior coupled-field measurement at $\phi = 180^\circ$, $D = 1.5$ A.

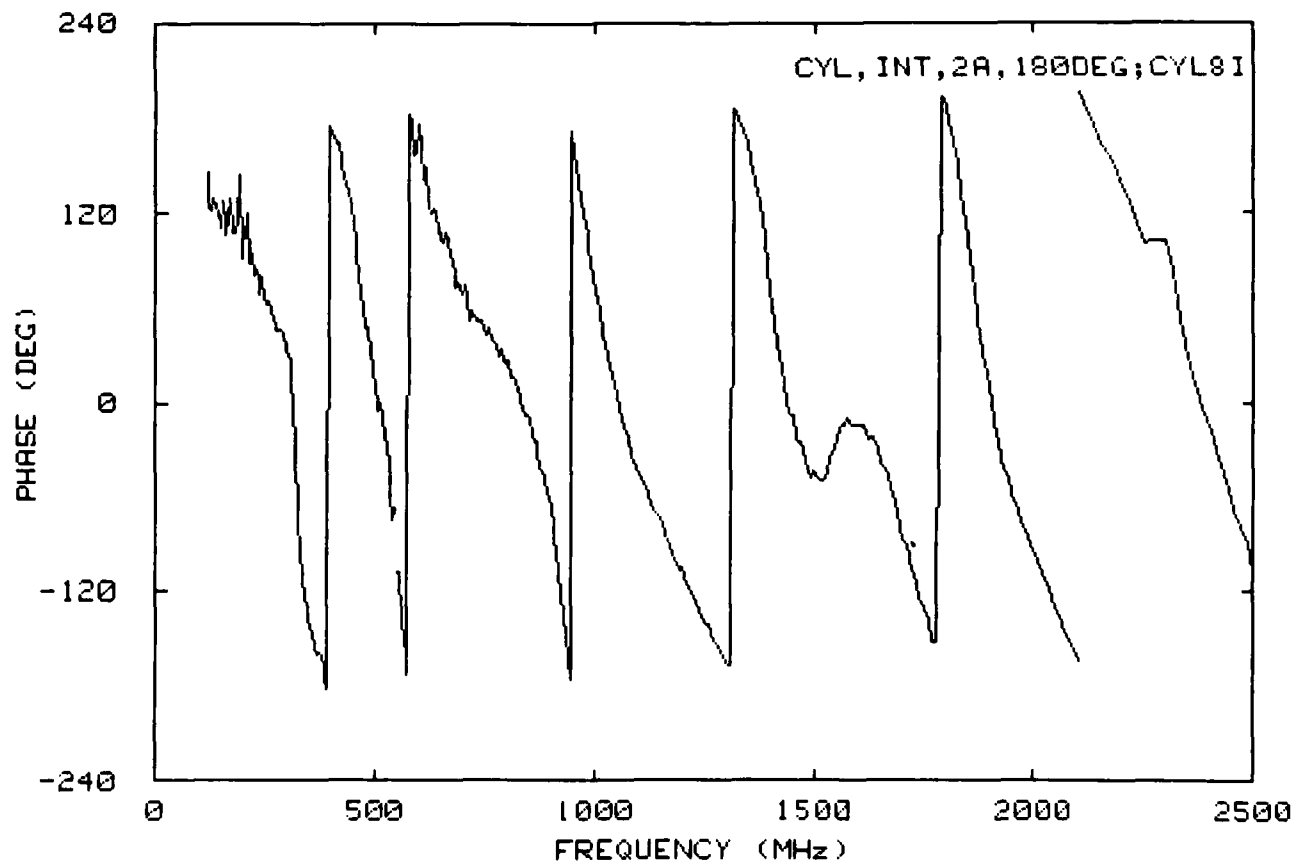
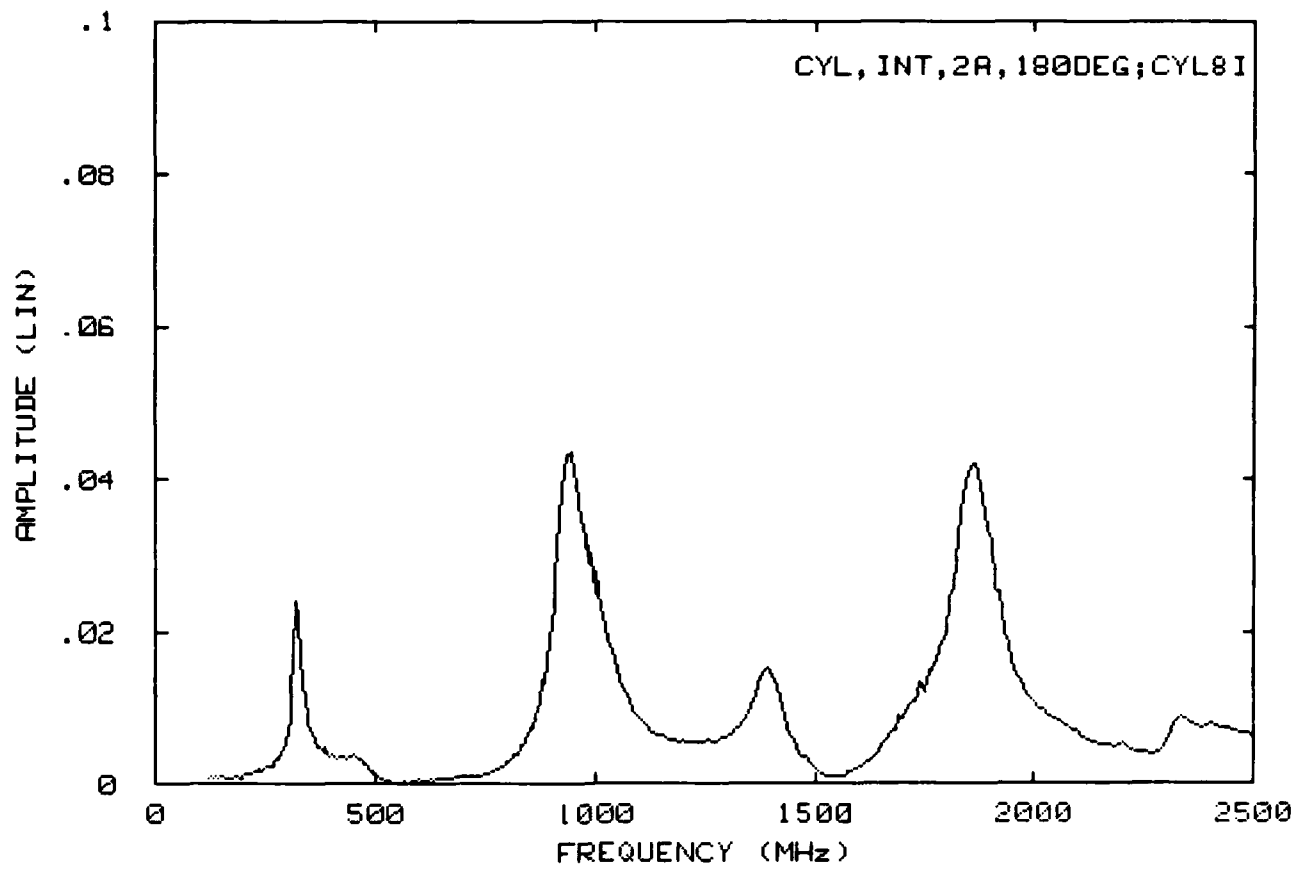


Figure 6.17. Interior coupled-field measurement at $\phi = 180^\circ$, $D = 2.0$ A.

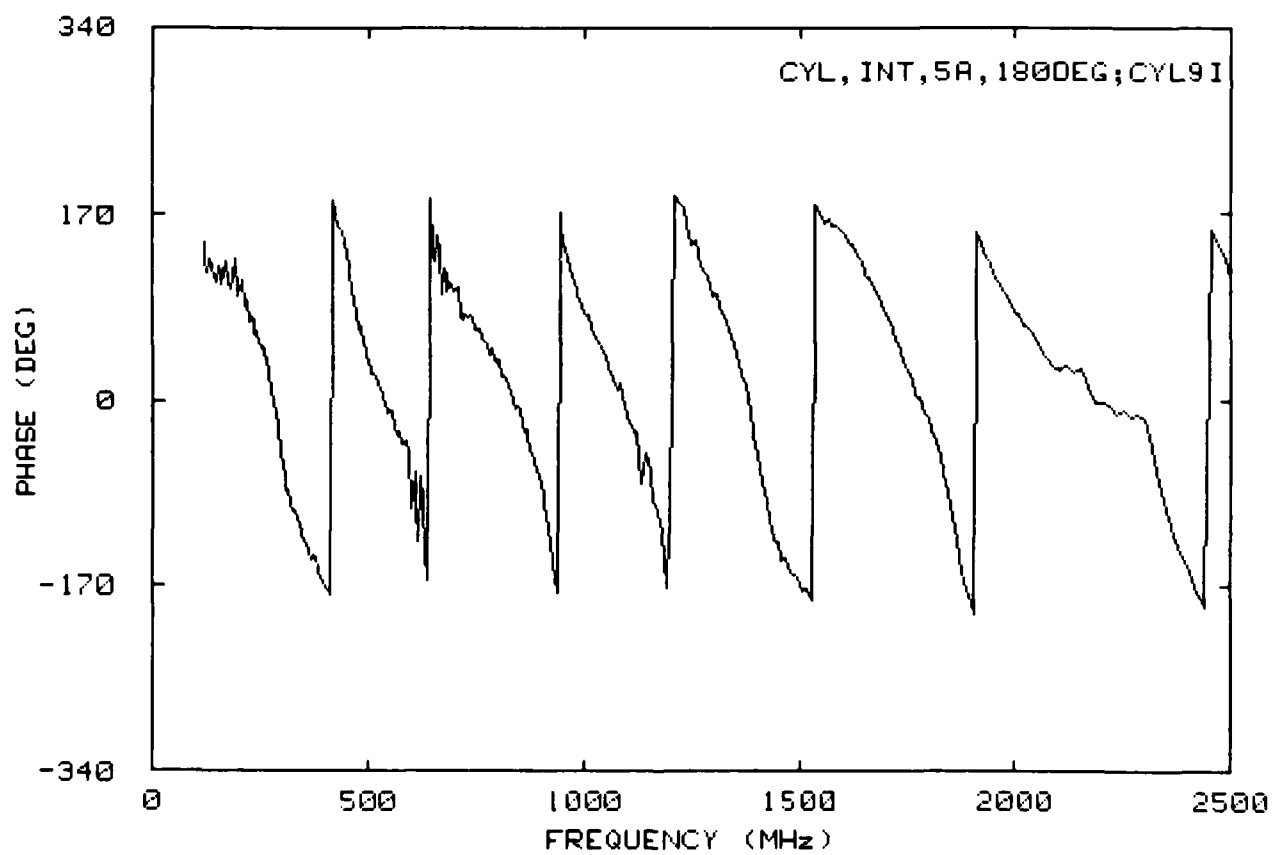
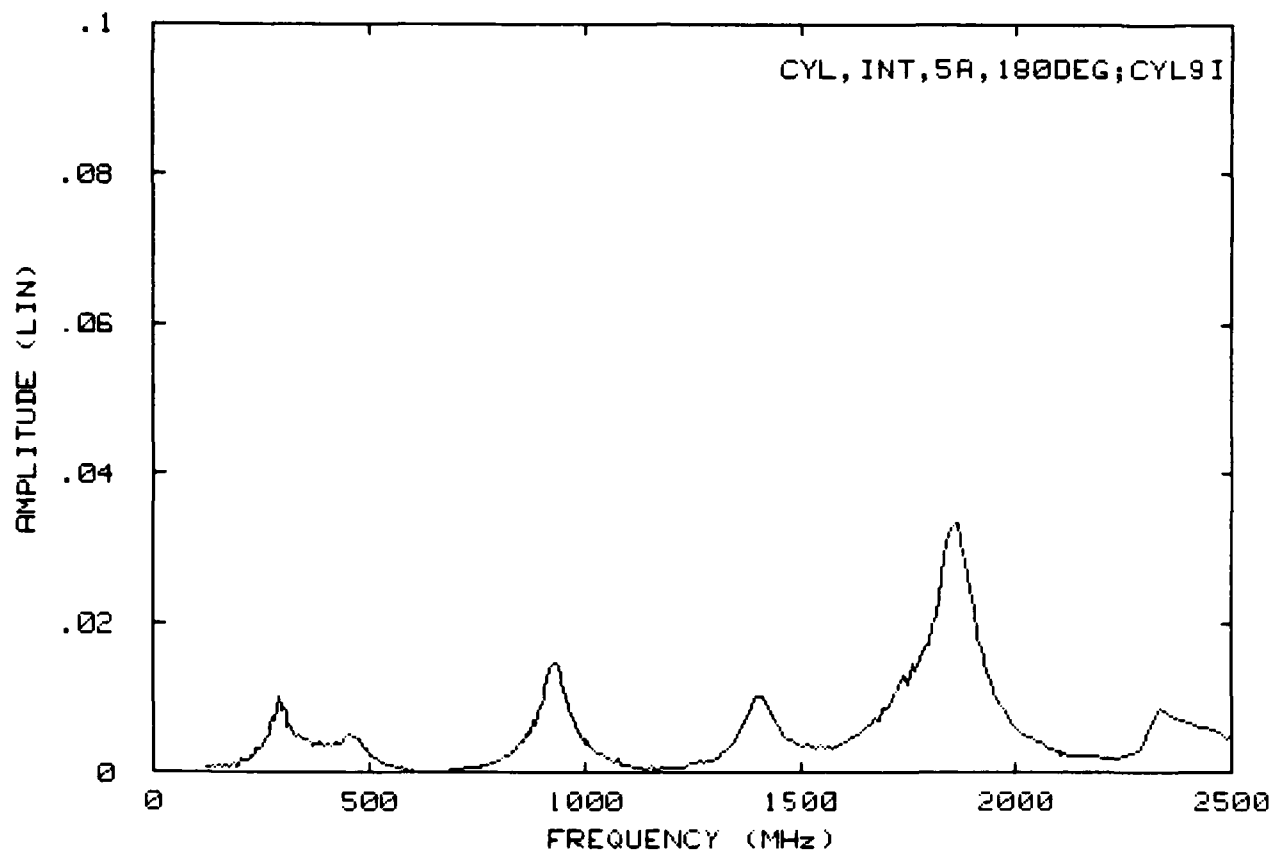


Figure 6.18. Interior coupled-field measurement at $\phi = 180^\circ$, $D = 5.0$ A.

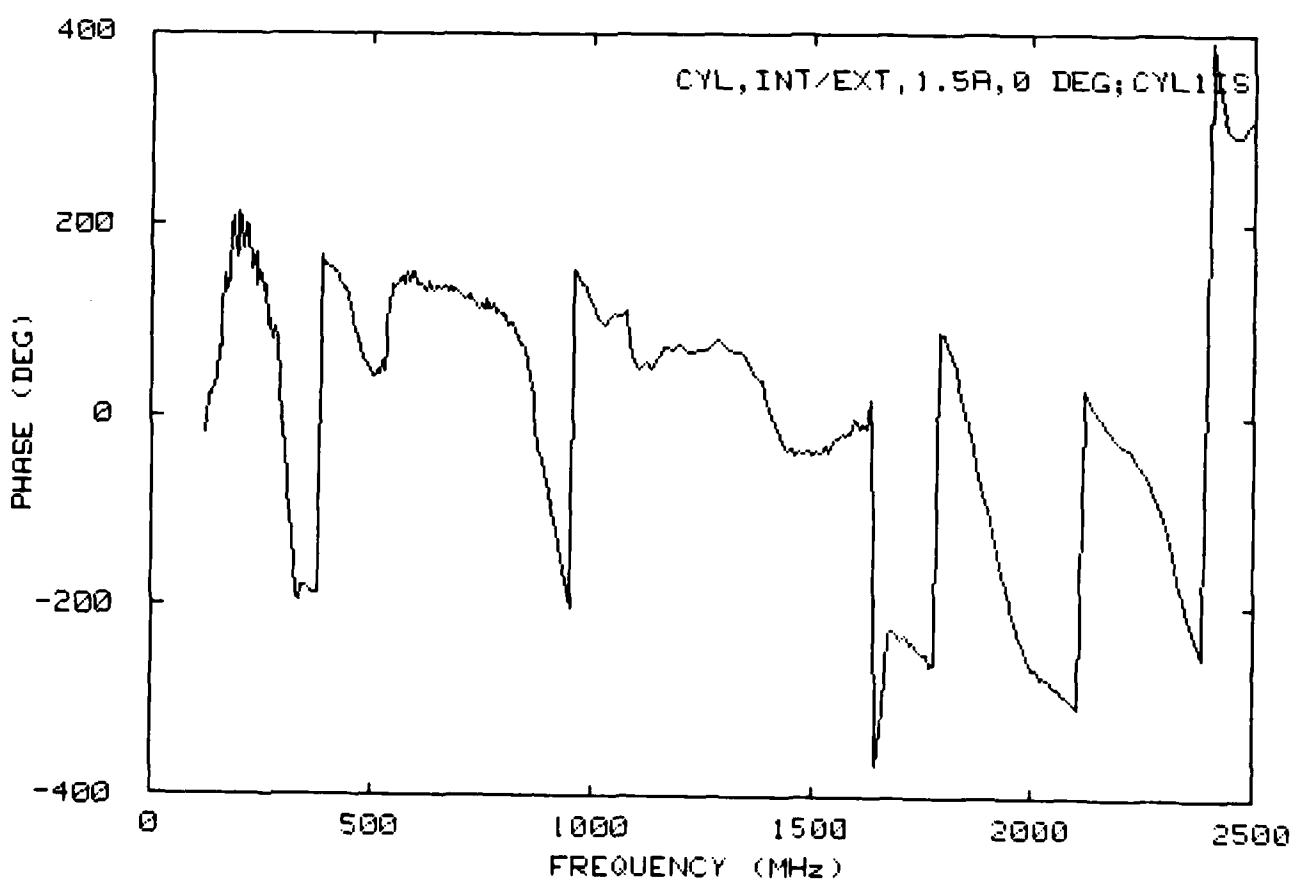
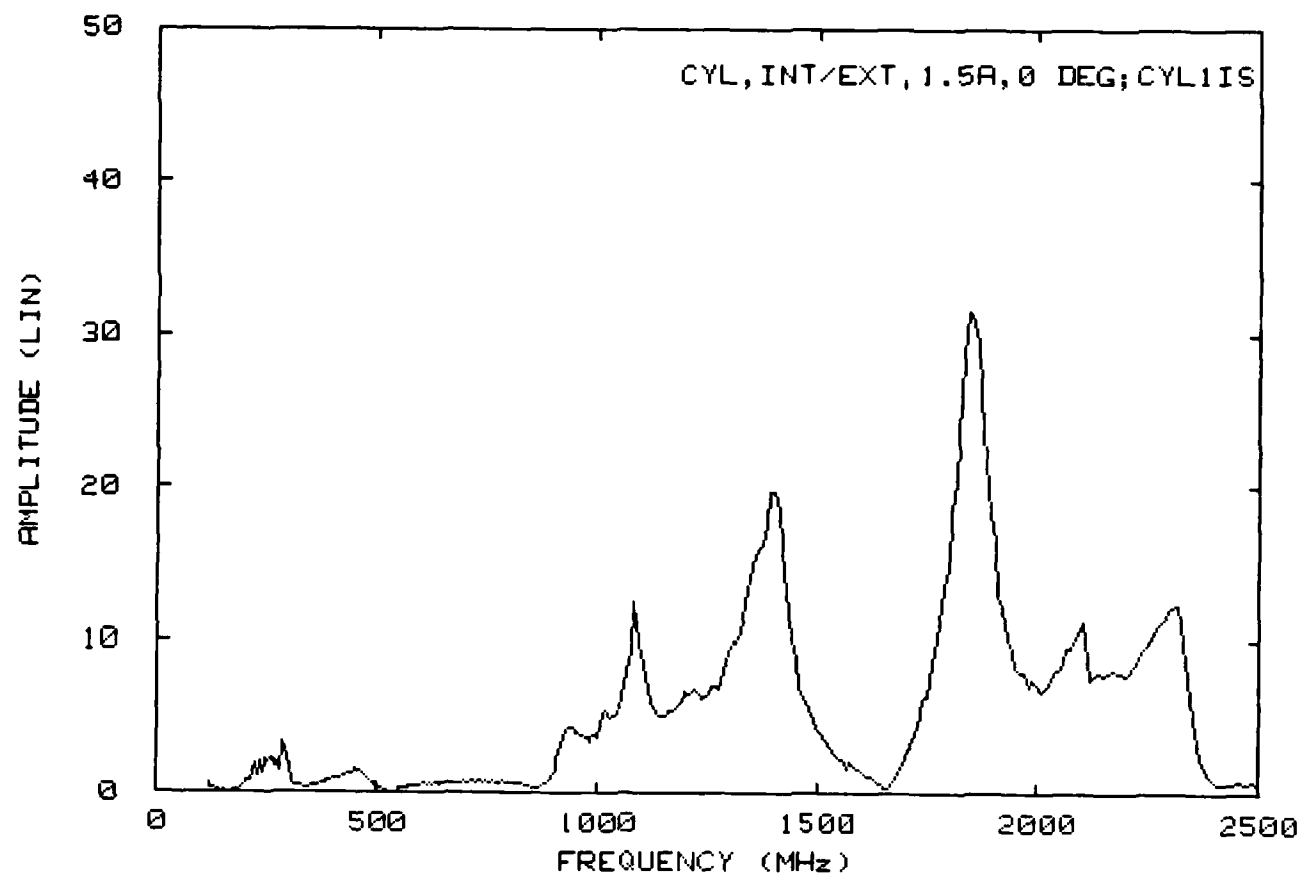


Figure 6.19. Transfer coefficients for $\phi = 0^\circ$, $D = 1.5$ A.

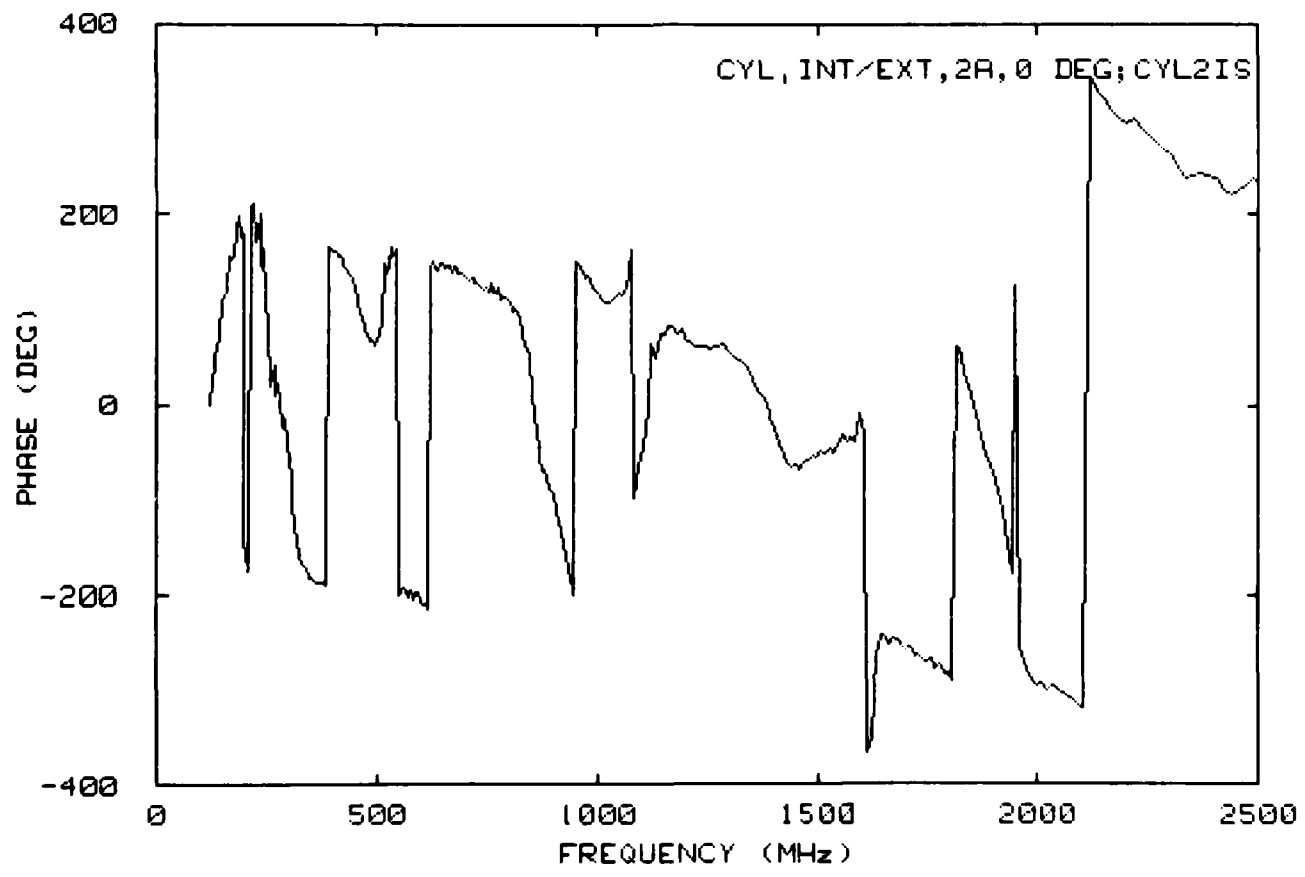
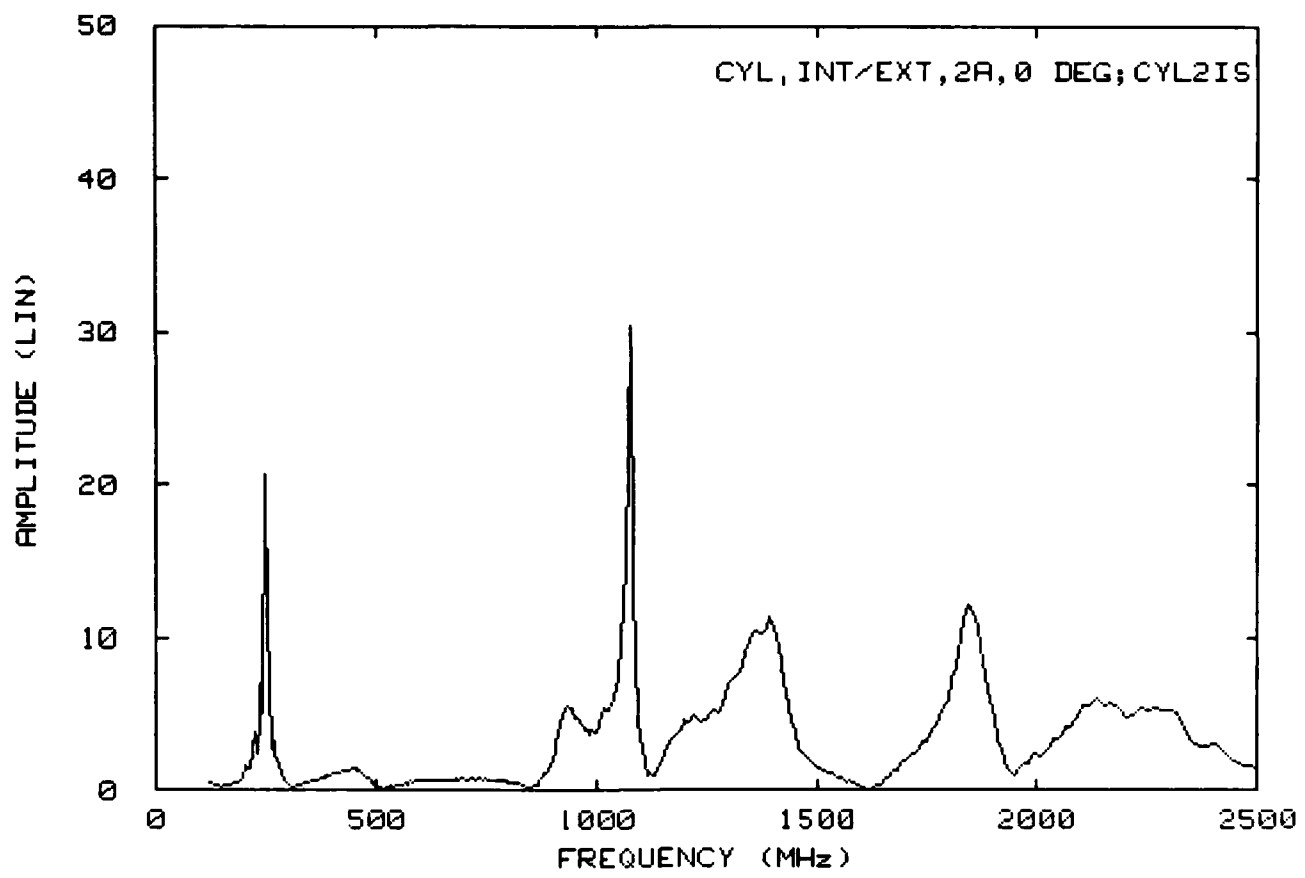


Figure 6.20. Transfer coefficients for $\phi = 0^\circ$, $D = 2.0$ A.

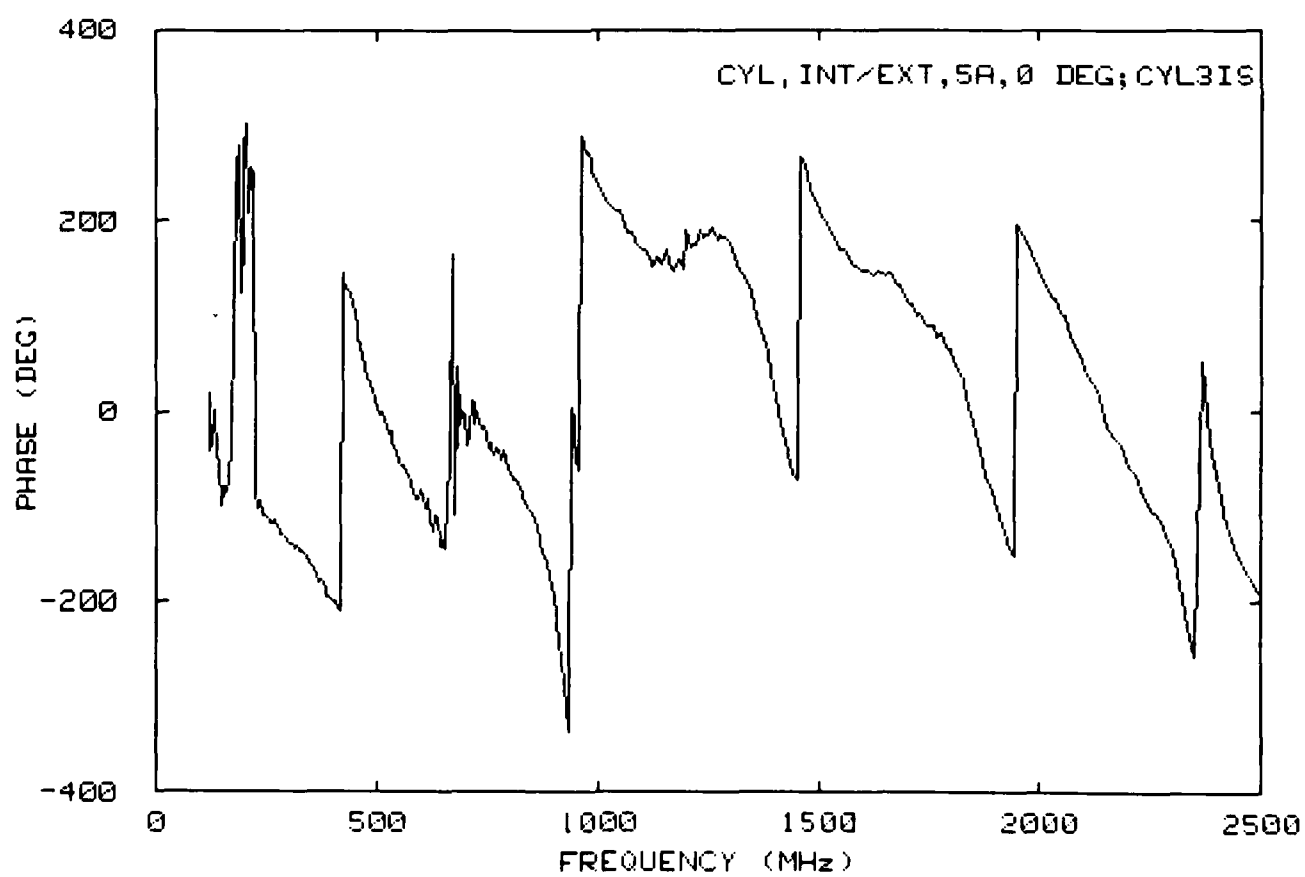
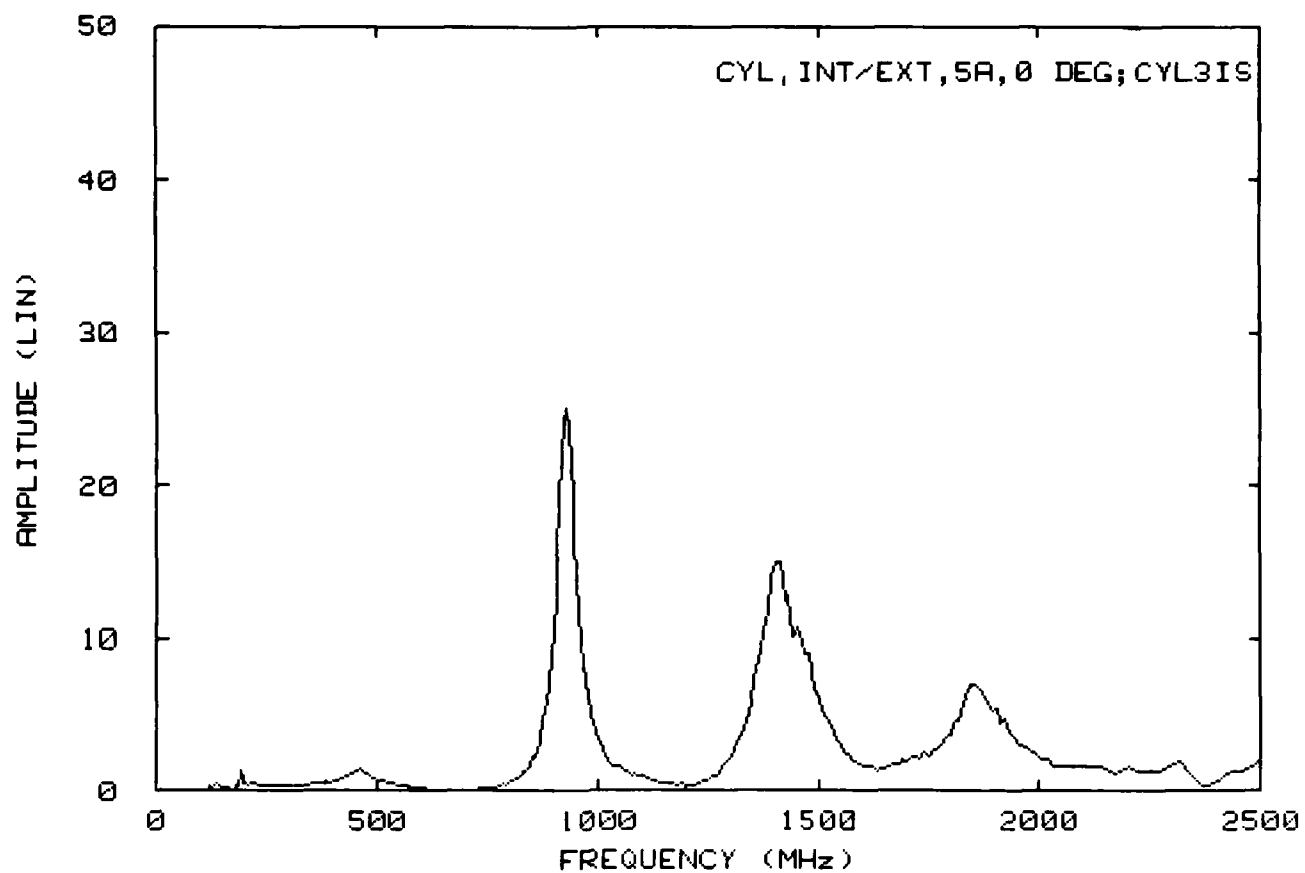


Figure 6.21. Transfer coefficients for $\phi = 0^\circ$, $D = 5.0$ A.

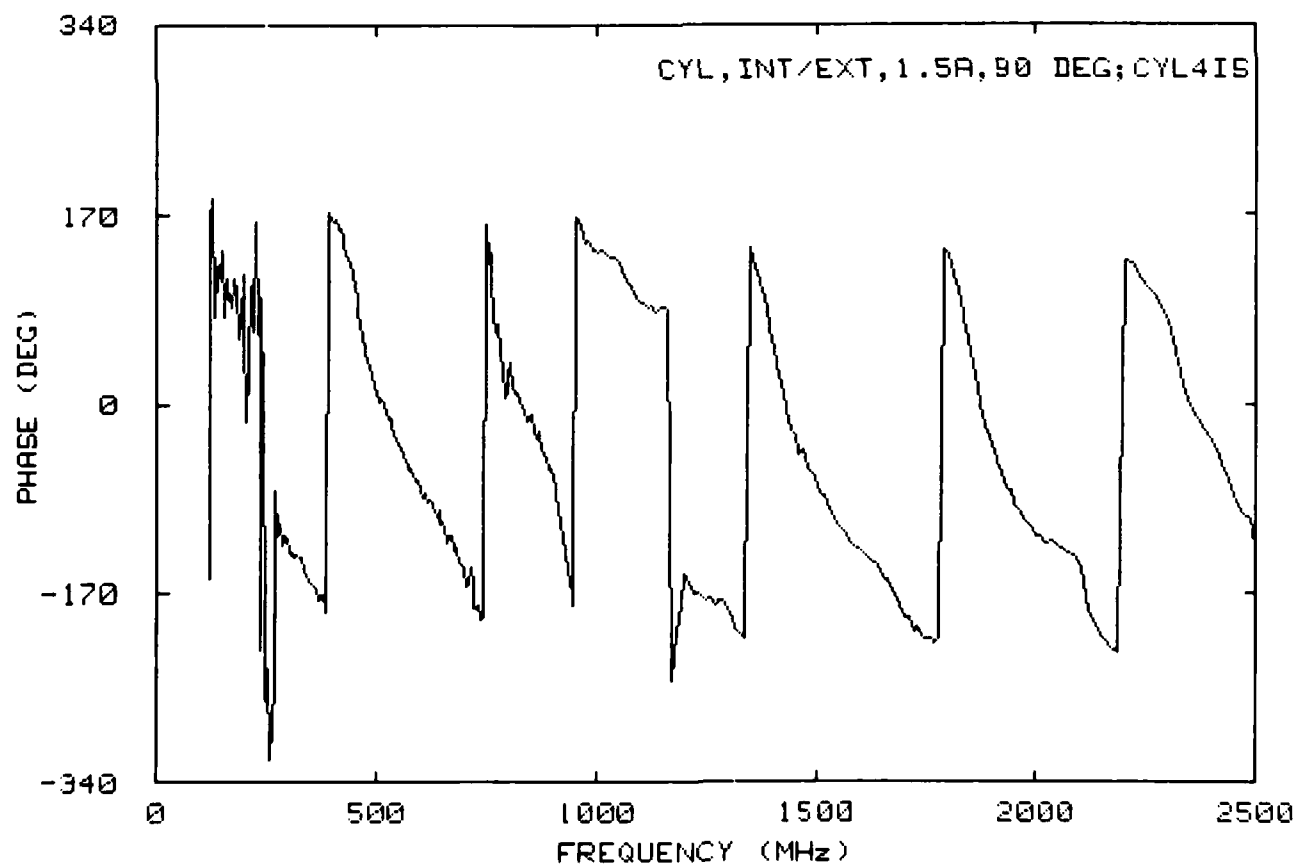
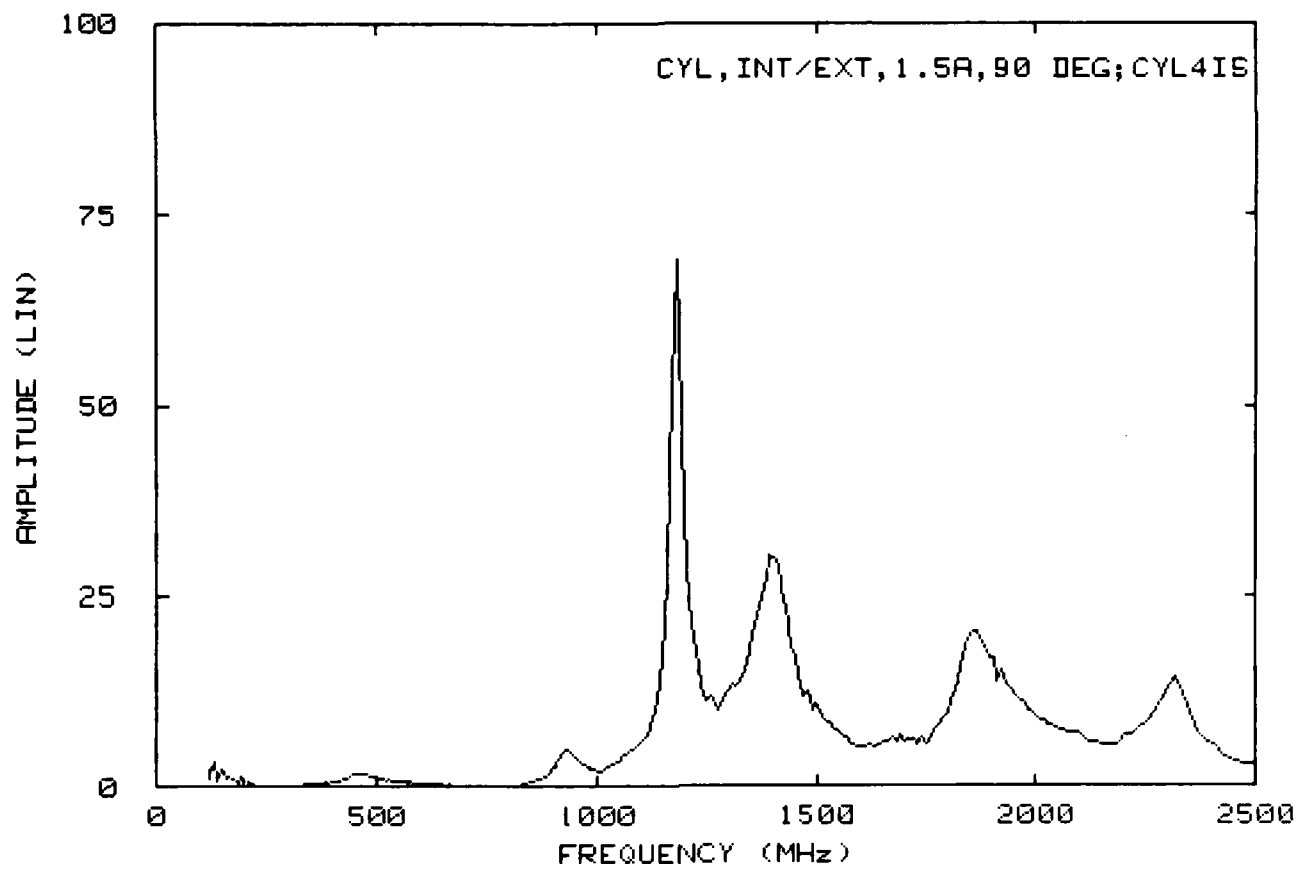


Figure 6.22. Transfer coefficients for $\phi = 90^\circ$, $D = 1.5$ A.

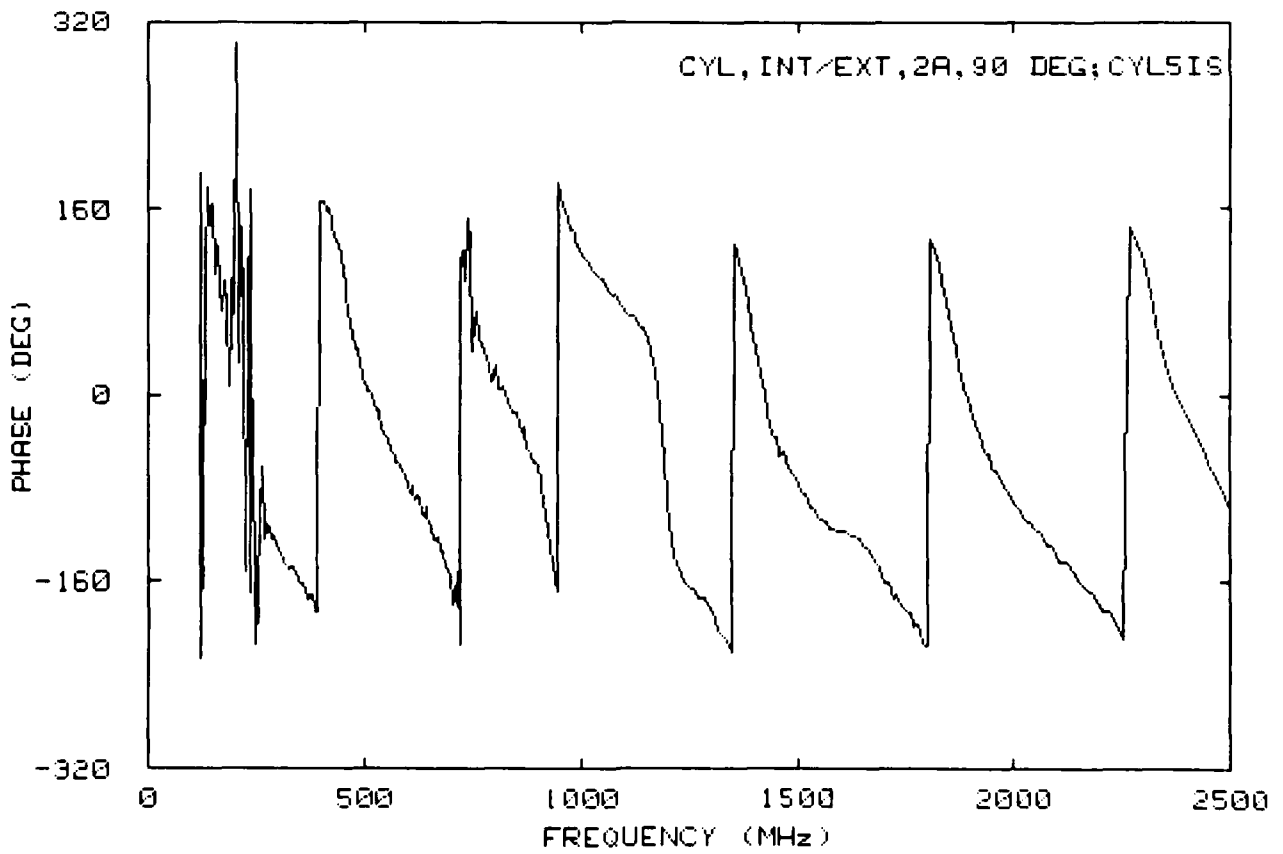
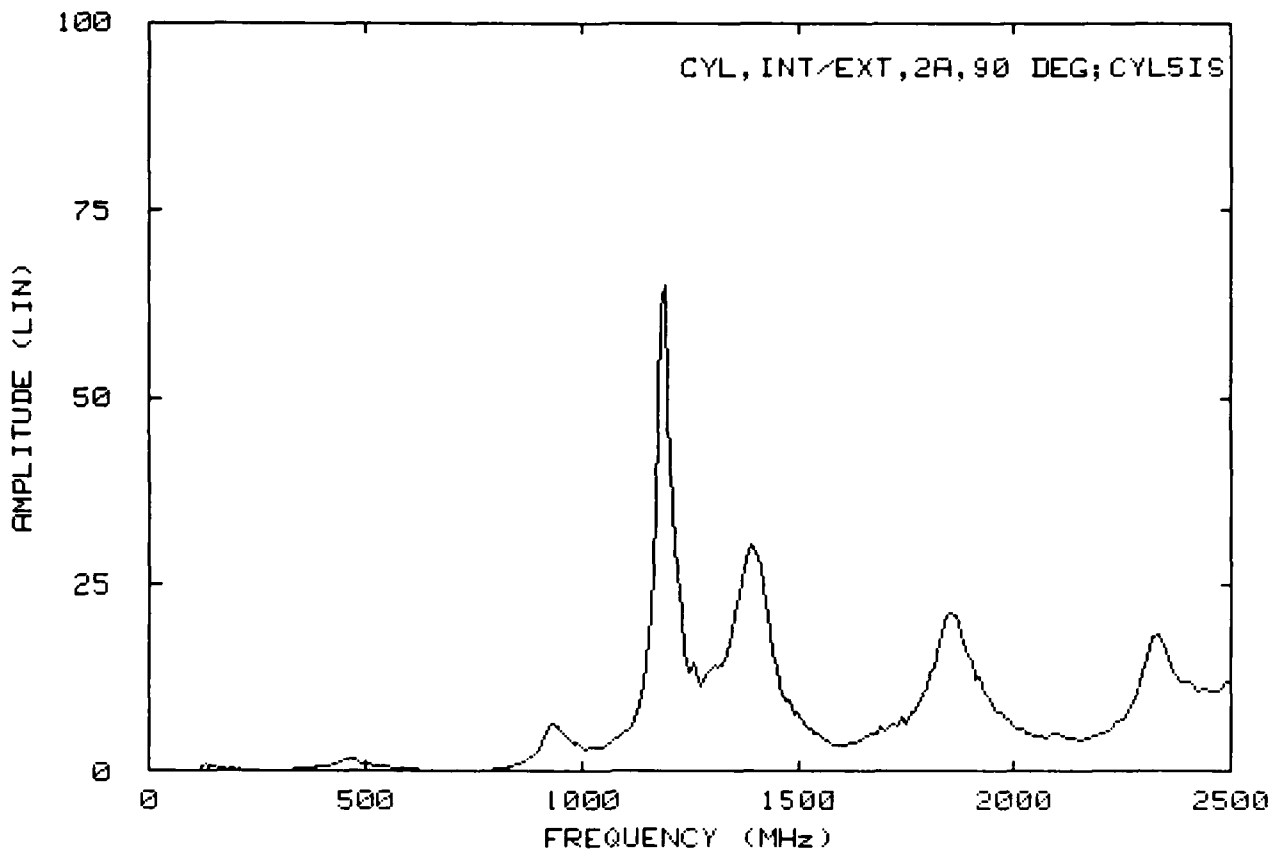


Figure 6.23. Transfer coefficients for $\phi = 90^\circ$, $D = 2.0$ A.

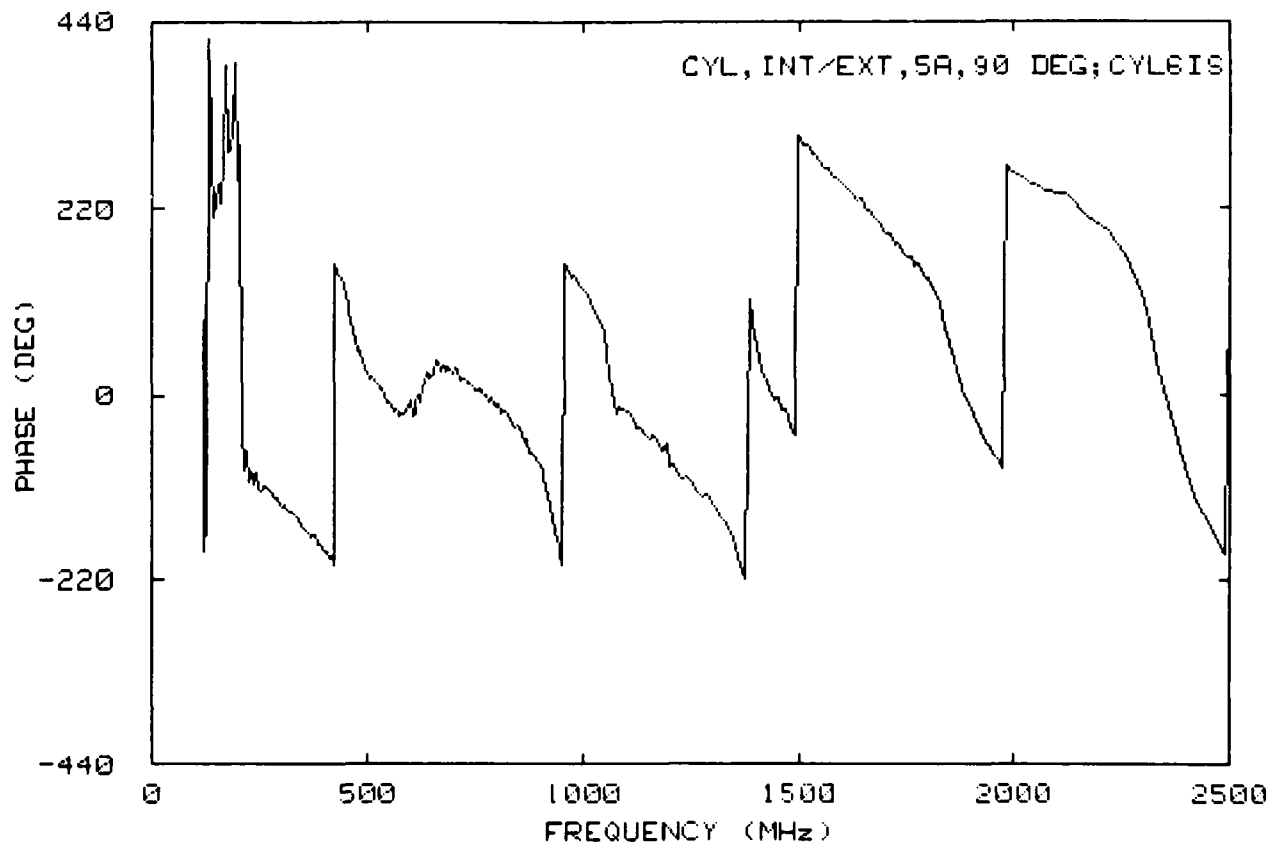
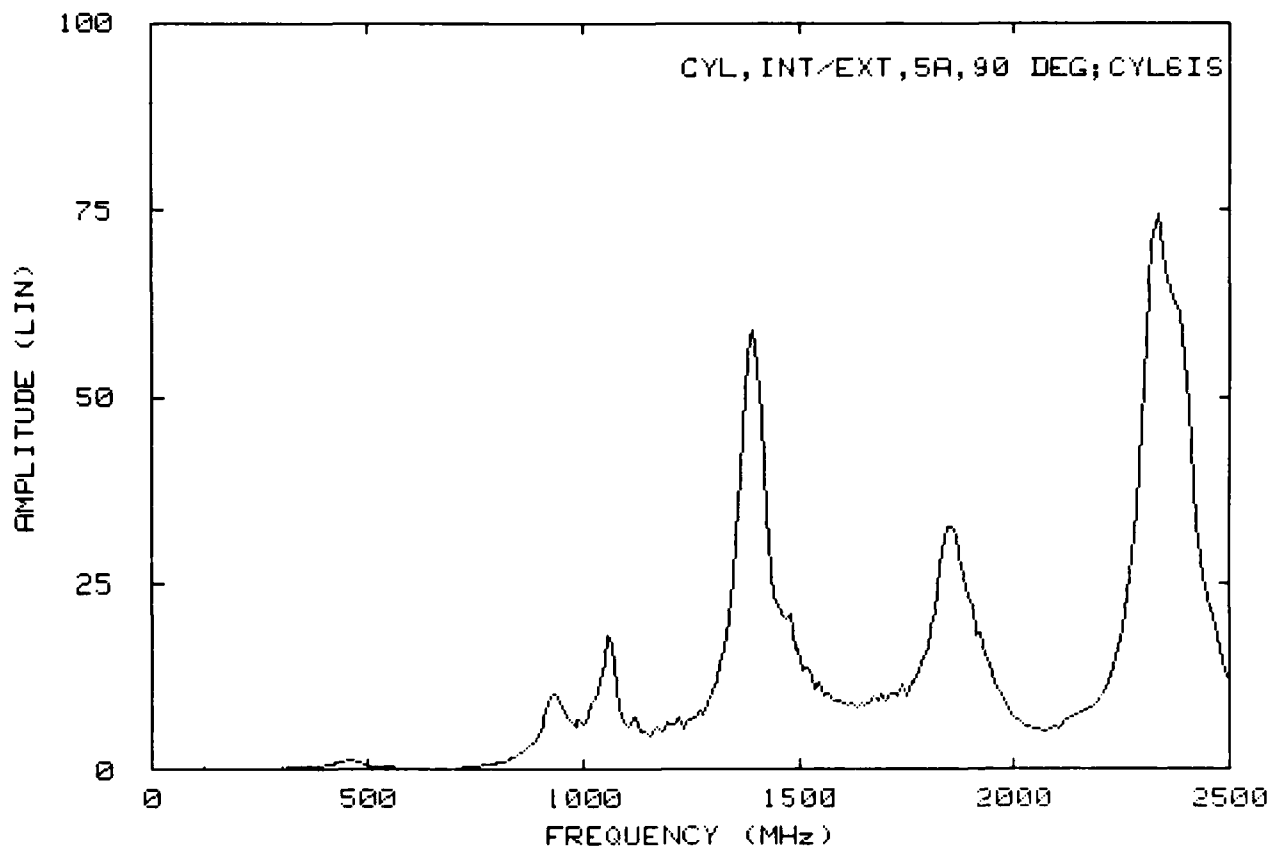


Figure 6.24. Transfer coefficients for $\phi = 90^\circ$, $D = 5.0$ A.

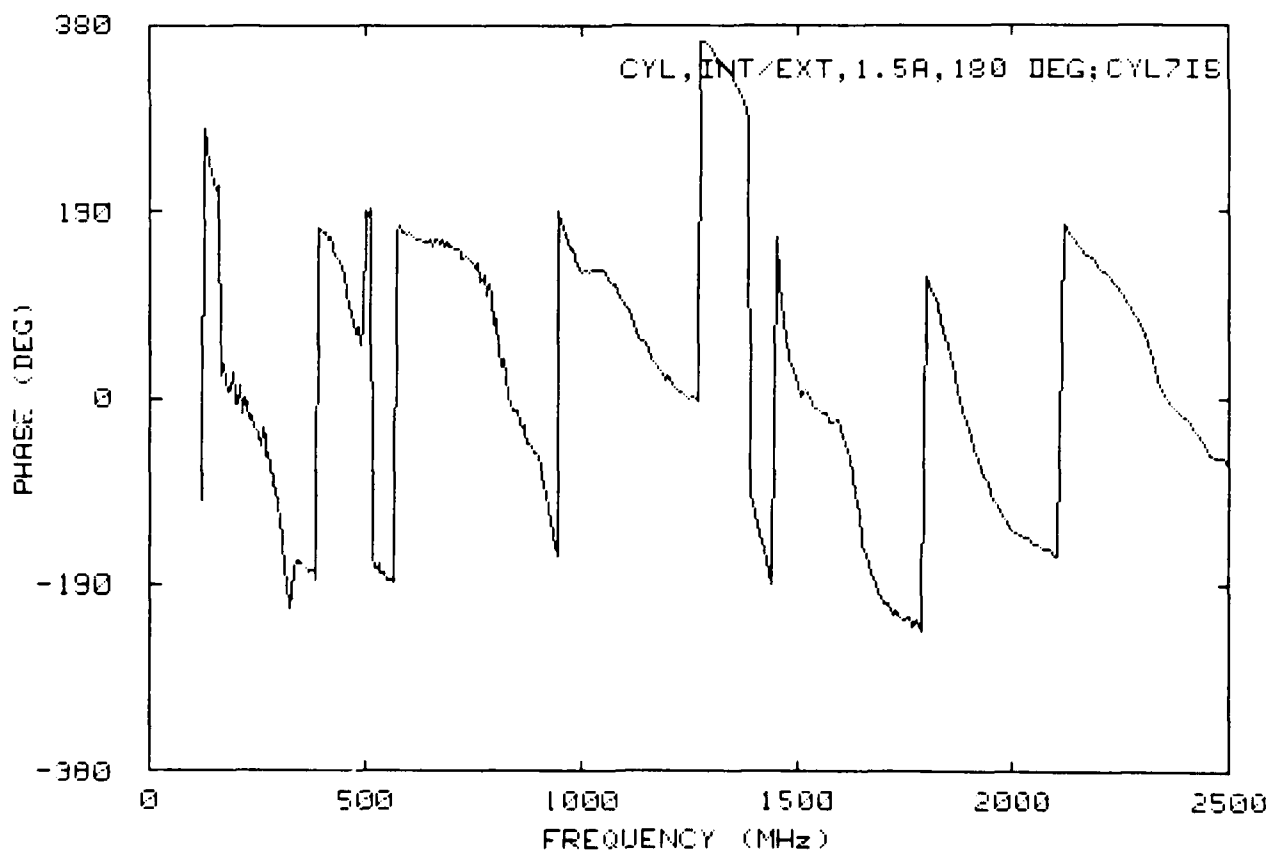
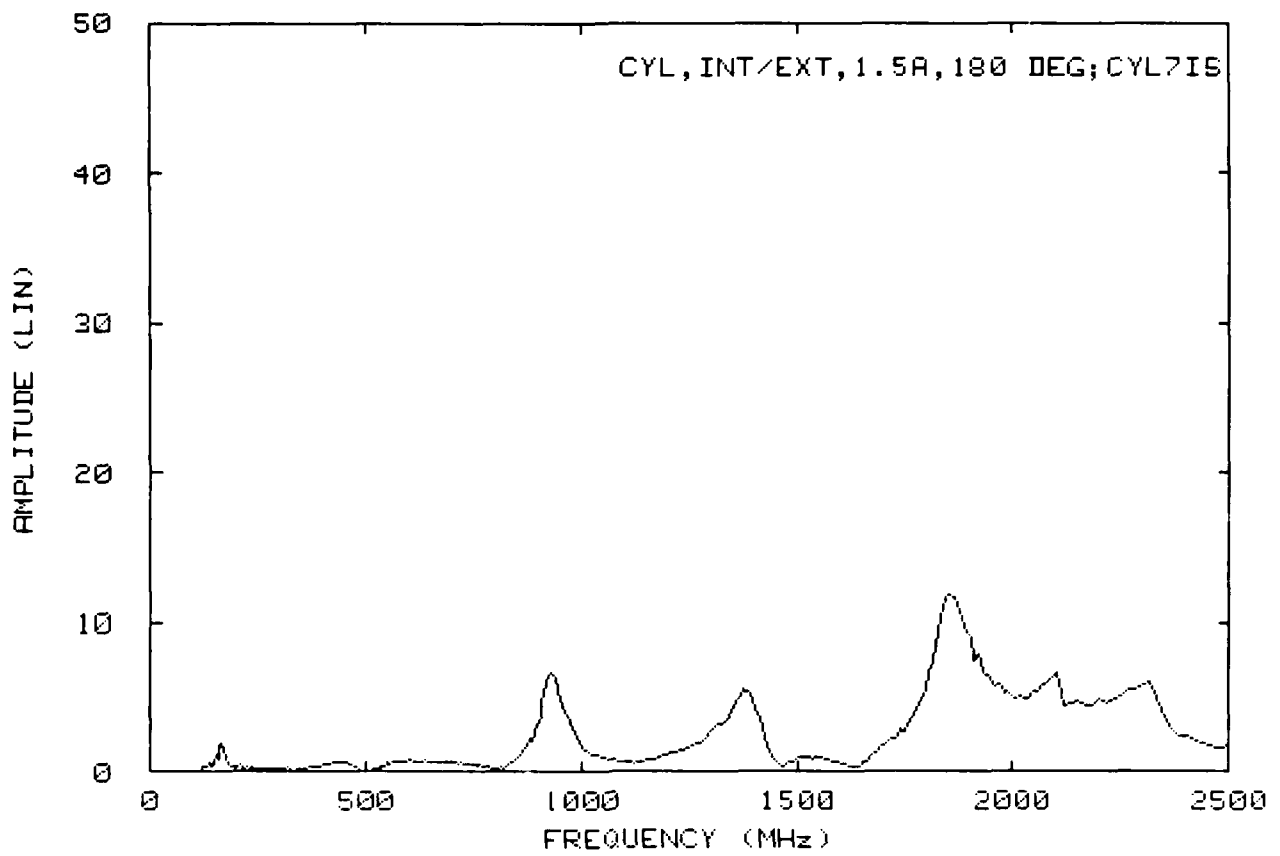


Figure 6.25. Transfer coefficients for $\phi = 180^\circ$, $D = 1.5$ A.

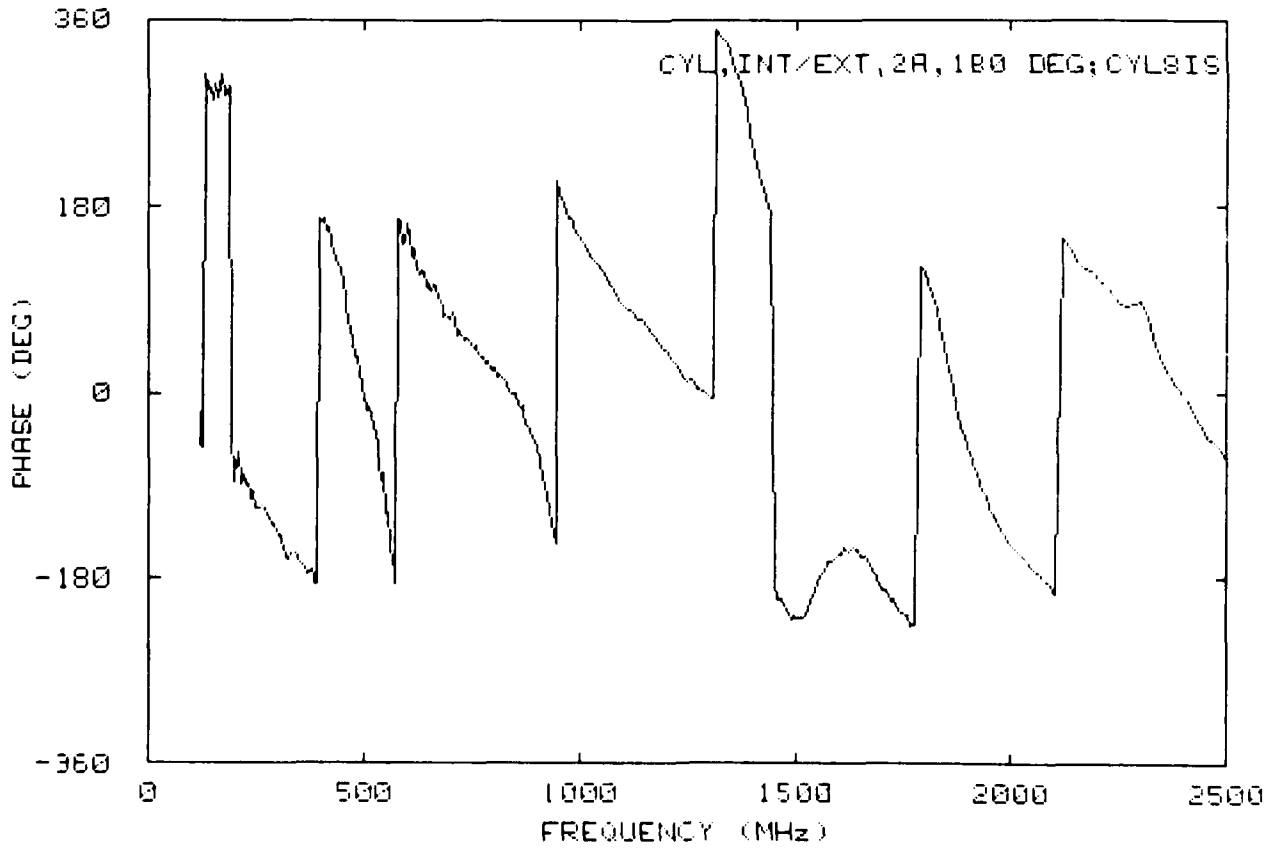
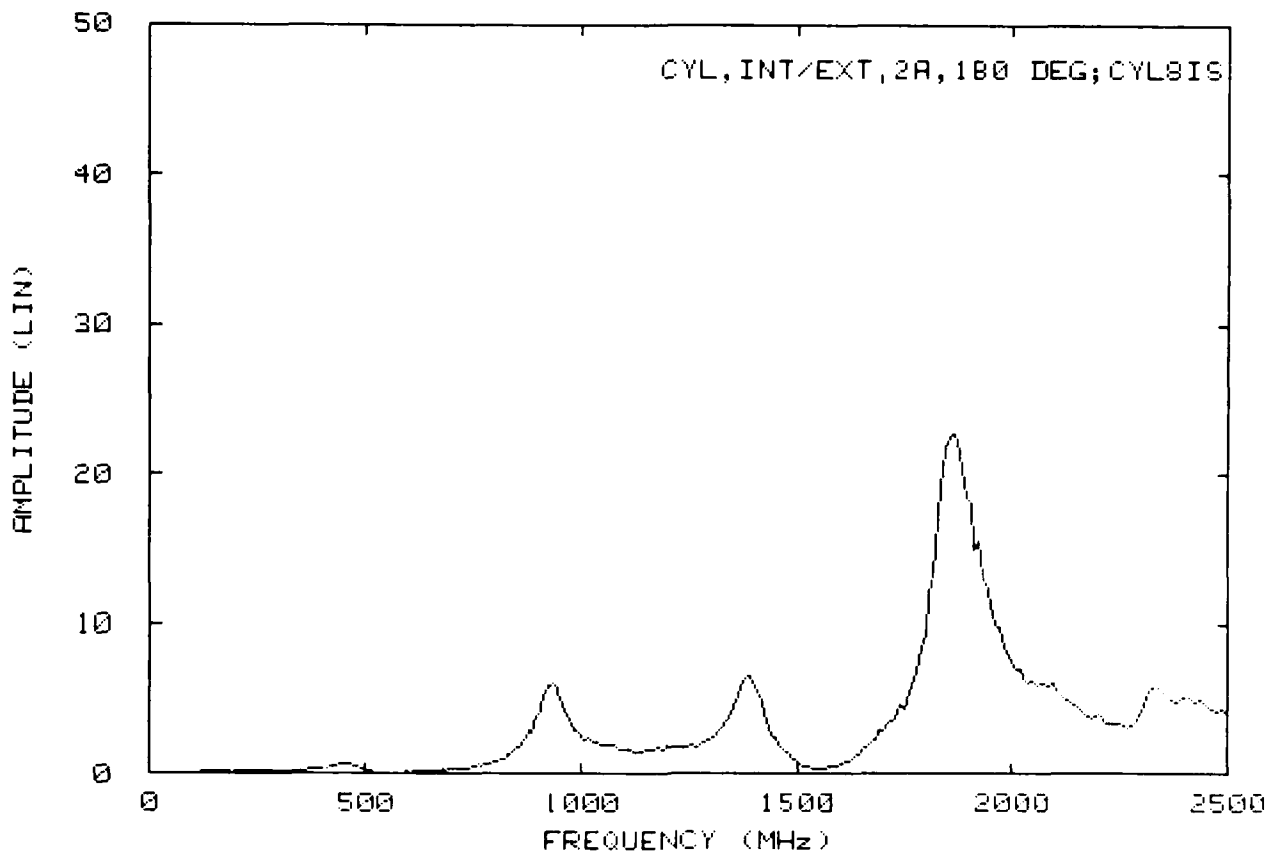


Figure 6.26. Transfer coefficients for $\delta = 180^\circ$, $D = 2.0$ A.

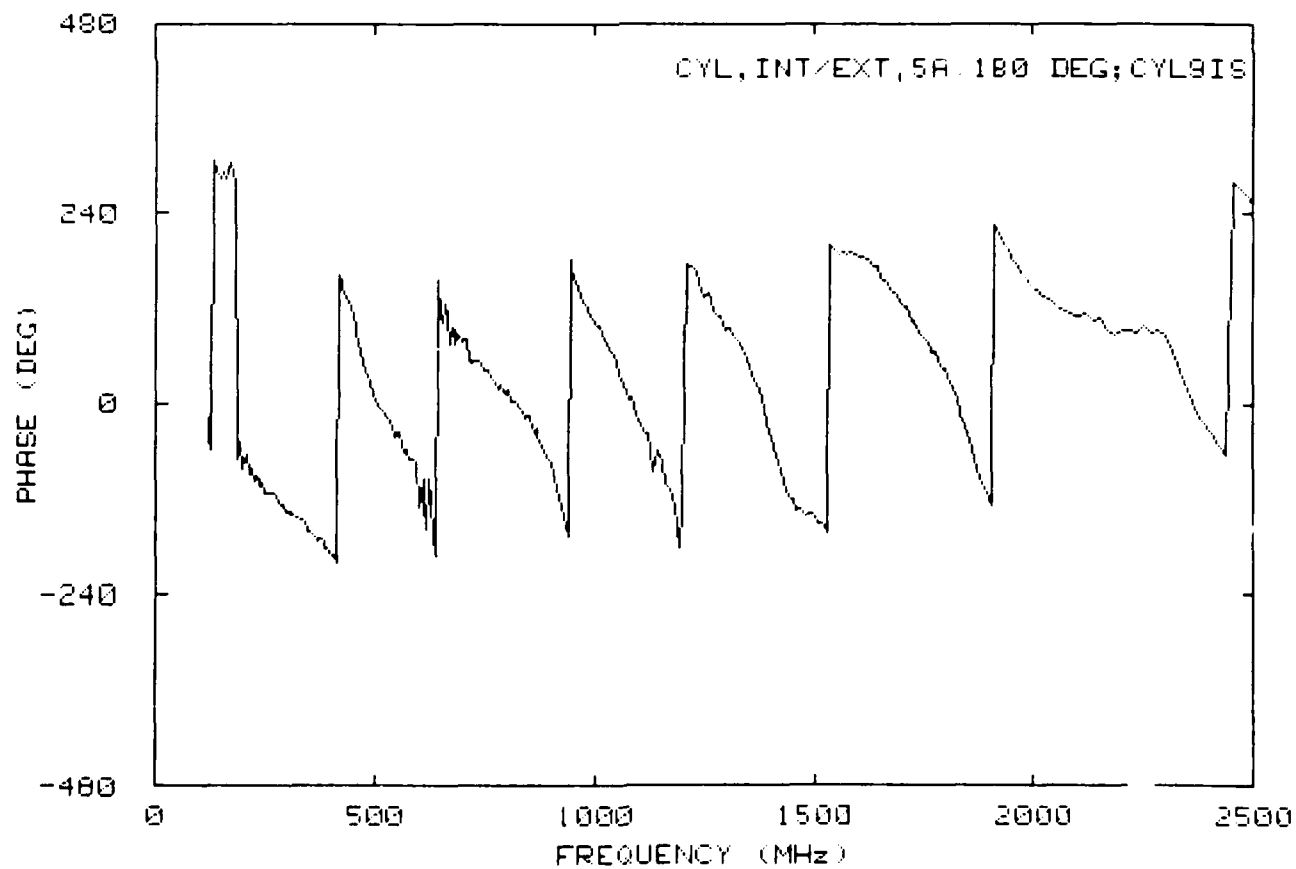
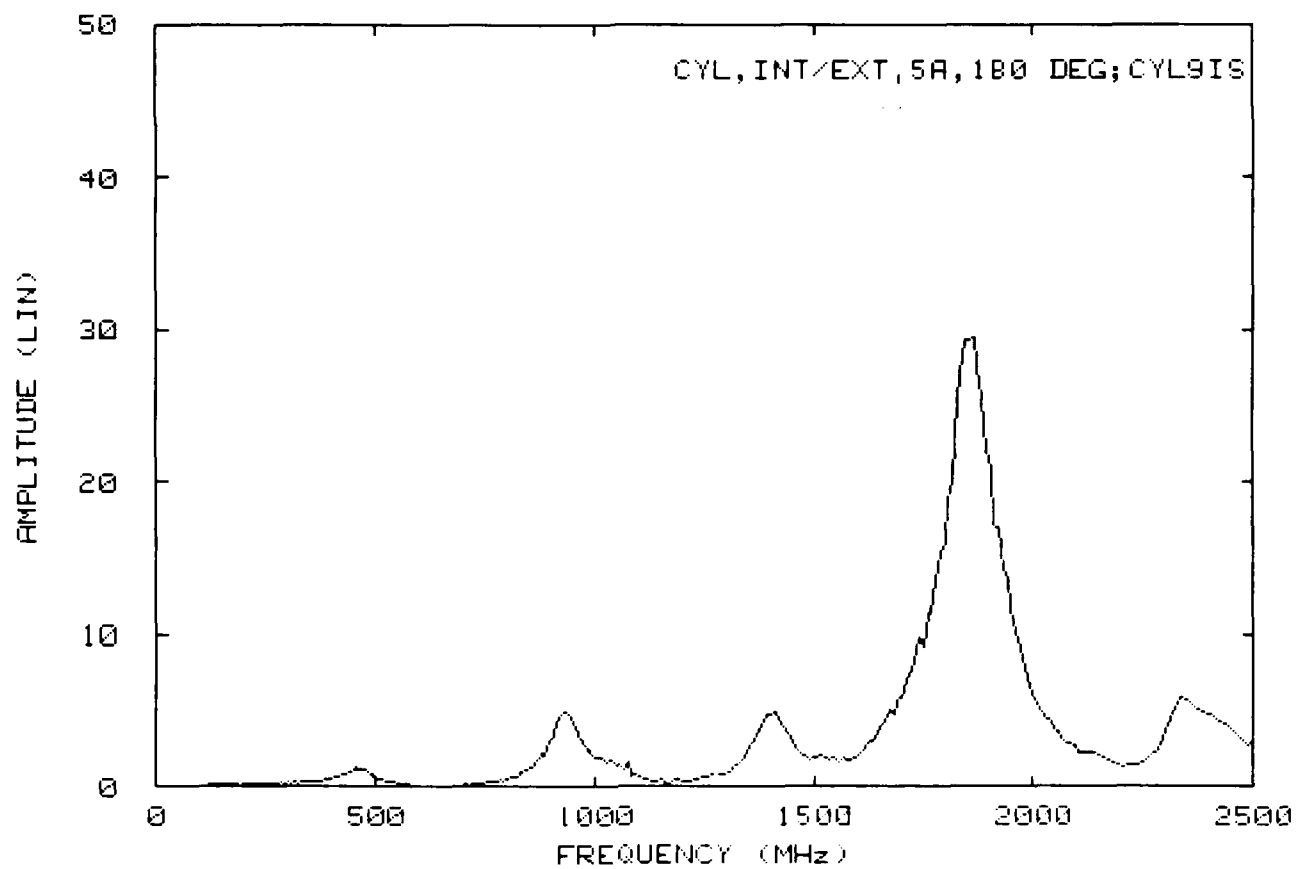


Figure 6.27. Transfer coefficients for $\phi = 180^\circ$, $D = 5.0 \text{ A}$.

SECTION 7
SOME AFTERTHOUGHTS

The study neither proved nor disproved the Sancer formulation [5], mainly because of noisy data. The noise in these types of measurements consist not only of thermal noise (due to low signal) but also is attributed to non-ideal plane wave illumination, unwanted interaction in the chamber and signal penetrations through cables and connectors. After the measurement program was completed and the data studied it became evident that the low level interior measurements (Section 6) were, indeed, contaminated by the leakage fields.

By recognizing and knowing the noise characteristics in the measured data one should be able to extract more meaningful results from those data than was obtained by Sancer or us. If measurements such as these, or similar ones, are repeated it is strongly suggested that an image plane approach be used whereby all the original leads can be routed below the image plane, thus minimizing the disturbance of the exterior fields and penetration of the exterior fields into signal leads.

LIST OF REFERENCES

- 1 R. W. Latham, "Small holes in cable shields," AFWL Interaction Note 118, September 1972.
- 2 K.S.H. Lee and C. E. Baum, "Application of modal analysis to braided-shield cables," AFWL Interaction Note 132, January 1973.
- 3 F. M. Tesche, "Topological concepts for internal EMP interaction," IEEE Trans. Antennas Propagat., Vol. AP-26, No. 1, January 1978.
- 4 C. E. Baum, "Extrapolation techniques for interpreting results of test in EMP simulators in terms of EMP criteria," Sensor and Simulation Note 222, March 1977.
- 5 Sancer, Maurice J., "Unified View of EMP Interaction, Threat, Extrapolation, and Alternate Simulation/Transfer Coefficients," Report No. RDA-TR-116002-003, R & D Associated, Marina del Rey, CA 90291, September 1981. (Draft)
- 6 Lee, K.S.H. (ed.), "EMP Interaction: Principles, Techniques and Reference Data," AFWL-TR-80-402, pp. 267-276, December 1980, EMP Interaction 2-1.
- 7 J. J. Bowman, T.B.A. Senior, and P.L.E. Uslenghi, "Electromagnetic and Acoustic Scattering by Simple Shapes," North-Holland Publishing Company-Amsterdam, 1969.
- 8 EG & G Standard EMP Instrumentation Catalog, Albuquerque, NM, 1980.
- 9 Marcuvitz, N., ed., Waveguide Handbook, McGraw-Hill, New York, 1951.
- 10 Roters, H. C., Electromagnetic Devices, J. Wiley and Sons.
- 11 Boast, W. B., Vector Fields, Harper and Row, New York, 1964.

APPENDIX

ESTIMATING THE JUNCTION CAPACITANCE BETWEEN TWO COAXIAL CABLES

A.1 Capacitances of Basic Configurations

A.1.1 Rectangular Parallelepiped Sections

If the magnitude of the electric-flux density in the field is D , the electric flux passing across the surface boundary S (see Figure A-1) for the uniform field is

$$\psi = D(s) = D(ab) .$$

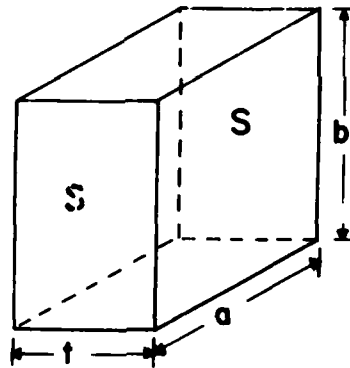


Figure A-1. Parallelepiped section.

The electric potential rise across the space, along the flux lines is

$$\phi = Et .$$

The capacitance of the space is

$$C = \frac{Q}{\phi} = \frac{\psi}{\phi} = \frac{Dab}{t} = \epsilon_0 \epsilon \frac{ab}{t} , \quad (4)$$

where W = the amount of charge at the surface S ,

ϵ_0 = the permittivity of free space ($= 8.81 \times 10^{-12}$ F/m) and

ϵ = the dielectric constant.

If there is a magnetic field in the same space, then

$$\psi_m = B(s) = B(ab)$$

$$\phi_m = Ht$$

and the permeability of this region is

$$\mu = \frac{\psi_m}{\phi_m} = \frac{Bab}{Ht} = \mu_0 \frac{ab}{t} \quad (5)$$

where μ_0 is the permeability of the free space ($= 12.56 \times 10^{-7}$ Hz/m).

Consider Eqs. (4) and (5), in which the length t is a mean length of the flux path and the area (ab) is obtained by dividing the volume of the region by the mean length of the flux path. Thus

$$C \text{ (or } P) = \epsilon_0 \epsilon \text{ (or } \mu_0) \left[\frac{\text{volume of region}}{(\text{mean length of path})^2} \right]. \quad (6)$$

A.1.2 Semicircular Cylindrical Regions

The fringing flux between two edges, $L-L'$, is determined as follows.

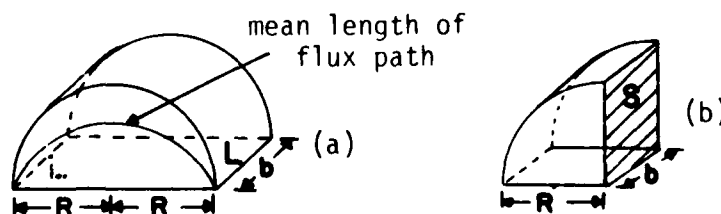


Figure A-2. Semicircular cylindrical sections.

The mean length of the flux path for this case can be considered to be equal to the length of a line drawn midway between the diameter and the semicircumference as shown in Figure A-2. The length of the mean flux path will equal to $(2.24 R)$ by graphical measurement. The volume of the region is $(\pi R^2 b/2)$. Hence, from Eq. (6), the capacitance of the semicircular cylindrical region is

$$C = \epsilon_0 \epsilon \frac{\frac{\pi R^2 b}{2}}{(2.24 R)^2} = 0.26 \epsilon_0 \epsilon b \quad (7)$$

If there is only one half of a semicircular cylinder as shown in Figure A-2(b), the flux passes between the line L and the surface S. Both the volume and the flux path are reduced by two. Because the length term is squared, the resulting capacitance is

$$C = 0.52 \epsilon_0 \epsilon b \quad (8)$$

A.1.3 Spherical Quadrants and Octants

The flux lines of the spherical quadrant as shown in Figure A-3(a) terminate at the points labeled P-P'. The mean length of the flux path is equal to $2.6 R$ by graphical measurement. Consequently, the capacitance of the space is approximately

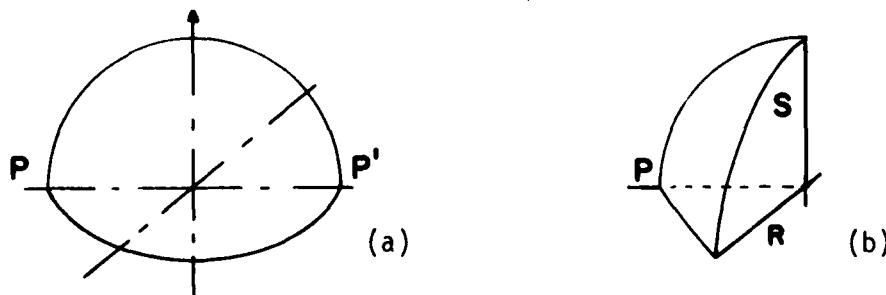


Figure A-3. Spherical quadrant sections.

$$C = \epsilon_0 \epsilon \frac{\frac{\pi R^3}{3}}{(2.6 R)^2} = 0.154 \epsilon_0 \epsilon R \quad (9)$$

If there is only one half; i.e., an octant, as shown in Figure A-3(b), the flux passes between the point P and the surface S, the capacitance will be twice that of Eq. (9) and is

$$C = 0.308 \epsilon_0 \epsilon R \quad (10)$$

A.1.4 Quadrants and Octants of a Spherical Shell

The flux line terminates at the lines labeled L-L'. The volume of the quadrant of the spherical shell is

$$\frac{\pi}{3} (R_2^3 - R_1^3) \quad (11)$$

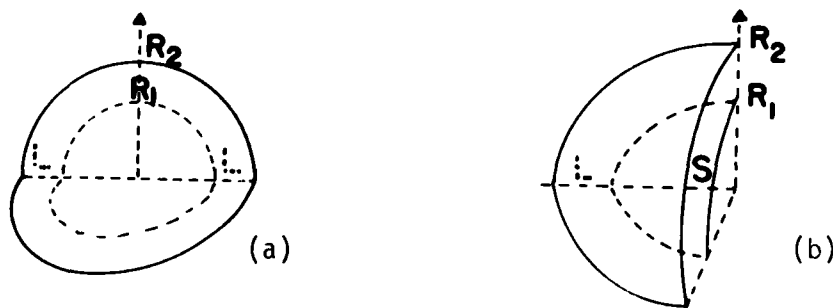


Figure A-4. Spherical shell sections.

The mean length of the flux path is

$$\frac{\pi}{2} (R_1 + R_2) \quad (12)$$

Thus, the capacitance is

$$C = \epsilon_0 \epsilon \left[\frac{\frac{\pi}{3} (R_2^3 - R_1^3)}{\frac{\pi^2}{4} (R_1 + R_2)^2} \right] = 0.42 \epsilon_0 \epsilon \left[\frac{R_2^3 - R_1^3}{(R_1 + R_2)^2} \right]. \quad (13)$$

If there is only one octant of the spherical shell, as shown in Figure A-4(b), the flux passes between the line L and the surface S. The capacitance will be twice that of Eq. (13); i.e.,

$$C = 0.84 \epsilon_0 \epsilon \left[\frac{R_2^3 - R_1^3}{(R_1 + R_2)^2} \right]. \quad (14)$$

A.1.5 A Sector of a Rectangular Toroid

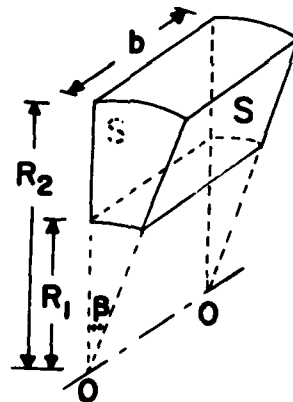


Figure A-5. Rectangular toroid sector.

Consider the region as shown in Figure A-5. Assume that the flux is concentric about the axis 0-0', and passes between the equipotential surface labeled S-S. If a current I is passes along the axis 0-0', the magnetic flux contained in the toroidal space is

$$\psi_m = \frac{\mu_0}{2\pi} I b \ln \frac{R_2}{R_1} \quad (15)$$

and the scalar magnetic potential is

$$\phi_m = \frac{\beta I}{2\pi} \quad (16)$$

The permeance of the sector of the rectangular toroidal space is

$$P = \frac{\psi_m}{\phi_m} = \frac{\frac{\mu_0}{2x} I b \ln \frac{R_2}{R_1}}{\frac{\beta I}{2\pi}} = \mu_0 \left[\frac{b \ln \frac{R_2}{R_1}}{\beta} \right] \quad (17)$$

and the capacitance of the region is

$$C = \epsilon_0 \epsilon \left[\frac{b \ln \frac{R_2}{R_1}}{\beta} \right] \quad (18)$$

Two special cases for the angle β are always encountered.

(1) If $\beta = \pi/2$ radians, as shown in Fig. 6(a)

$$C = \epsilon_0 \epsilon \left[\frac{2b \ln \frac{R_2}{R_1}}{\pi} \right], \quad (19)$$

(2) If $\beta = \pi$ radians, as shown in Fig. 6(b)

$$C = \epsilon_0 \epsilon \left[\frac{b \ln \frac{R_2}{R_1}}{\pi} \right] \quad (20)$$

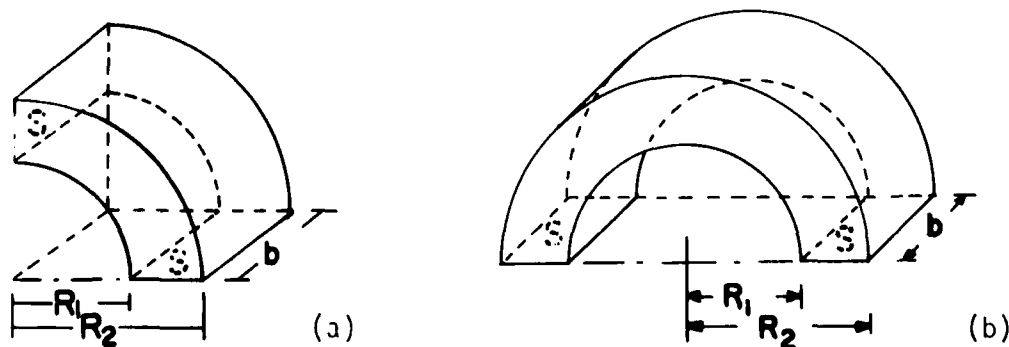


Figure A-6. Special cases of rectangular toroid.

A.2 Capacitance for the Junction Between Two Coaxial Cables

A junction of two coaxial cables of unequal inner and outer radii is shown in Figure A-7(b)

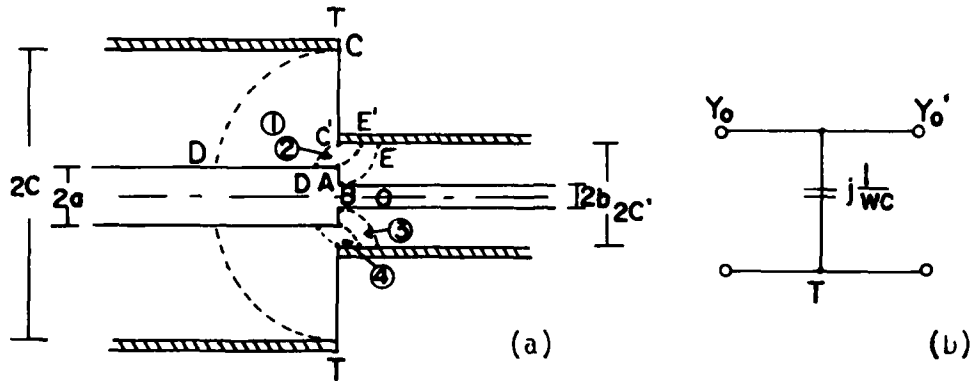


Figure A-7. Junction of dissimilar radii, $a > b$.

When only one of the radii of either the inner or the outer conductor is different, and the ratio C/a (or C'/a) ≤ 5 . The problem is easily solved with a set of formulas [see Ref. 9-11]. If the inner and outer radii are different, or the configuration in the junction is very complicated, the formulas will not serve, and an approximate estimate of the probable flux path is needed.

The distributive capacitance and the characteristic impedance for a uniform coaxial cable are

$$C = \frac{2\pi\epsilon\epsilon_0}{\ln \frac{R_2}{R_1}} \quad (\text{F/m})$$

and

$$Z_0 = \frac{1}{\sqrt{\epsilon}} \times 120 \ln \frac{R_2}{R_1} \quad (\Omega) \quad (21)$$

The regions that should be considered in the junction and its capacitance are:

(1) The circular toroid region between the toroidal terminal surface CC' of the outer conductor and the surface DD' of the inner conductor.

Assume that the flux lines of Path 1 are concentric circles having their center at Point A. The ratio of DD' to D'A (i.e., R_2/R_1) is usually large and formula (19) should be used to estimate the capacitance (when $\beta = \pi/2$)

$$C_1 = \epsilon\epsilon_0 \frac{2b_{eff}}{\pi} \ln \frac{R_2}{R_1}, \quad (22)$$

where b_{eff} should be the effective length of the path measured normally to the flux lines, b_{eff} can be taken as being equal to the circumference of a circle, the radius of which is equal to OA (i.e., R_1) plus the radius of the mean flux line. The radius of the mean flux line will be equal to the geometric mean between AC and AC'.

Thus

$$b_{eff} = 2\pi(OA + \sqrt{AC \cdot AC'}) = 2\pi[a + \sqrt{(c-a)(c'-a)}] . \quad (23)$$

Therefore the capacitance is

$$C_1 = 4\epsilon\epsilon_0 [a + \sqrt{(c-a)(c'-a)}] \ln \frac{c-a}{c'-a} . \quad (24)$$

(2) The region between the right-hand prism C' (a circle the radius of which is equal to OC') and the surface D'A (a cylinder) on the inner conductor.

AD-A166 414

TRANSFER COEFFICIENT MEASUREMENT STUDY(U) MICHIGAN UNIV
ANN ARBOR RADIATION LAB V V LIEPA 19 FEB 85 016301-1-F
DNA-TR-85-70 DNA001-78-C-0361

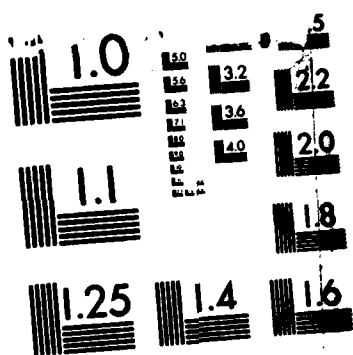
2/2

UNCLASSIFIED

F/G 20/14

NL





MICROCOPY RESOLUTION TEST CHART
NATIONAL BUREAU OF STANDARDS-1963-A

When AC' is close to OA , the mean length of the flux line may be taken as $1.22 R$. Using Eq. (6) the capacitance is:

$$\begin{aligned}
 C_2 &= \epsilon \epsilon_0 \frac{V}{(1.22 AC')^2} = \frac{\pi AC'^2}{4} \frac{b_{eff}}{(1.22 AC')^2} & (25) \\
 &= \frac{\pi(c' - a)^2}{4} \times \frac{2\pi[a + 0.5(c' - a)]}{1.22^2 (AC')^2} \\
 &= \epsilon \epsilon_0 \times 3.32[a + 0.5(c' - a)]
 \end{aligned}$$

where b_{eff} was taken as being equal to an arithmetic mean.

(3) The circular region between the toroidal terminal surface AB on the inner conductor and the surface EE' on the outer conductor.

The capacitance of this path is calculated in the same manner as Path 1. The radius of the mean flux line will be $\sqrt{cc' - b)(c' - a)}$, and b_{eff} becomes

$$b_{eff} = 2\pi [c' - \sqrt{(c' - b)(c' - a)}] \quad (26)$$

and the capacitance of the region is

$$\bar{C}_3 = \epsilon \epsilon_0 \times 4[c' - \sqrt{(c' - b)(c' - a)}] \ln \frac{c' - b}{c' - a} \quad (27)$$

(4) The region between the right-hand prism A (a circle the radius of which is equal to OA) and the surface $C'E'$ (a cylinder) on the outer conductor.

The capacitance of this path is calculated in the same manner as Path 2. The capacitance is

$$C_4 = \epsilon\epsilon_0 \times 3.32[a + 0.5(c' - a)] \quad . \quad (28)$$

Consider another junction as shown in Figure A-8, i.e., the radius of the inner conductor $a < b$. The formulae of Paths 3 and 4 are then

$$b_{\text{eff}_3} = 2\pi[c - \sqrt{(c - a)(c - b)}] \quad ,$$

$$b_{\text{eff}_4} = 2\pi[b + 0.5(c - b)] \quad ,$$

$$C_3 = \epsilon\epsilon_0 \times 4[c - \sqrt{(c - a)(c - b)}] \ln \frac{c - a}{c - b} \quad ,$$

$$C_4 = \epsilon\epsilon_0 \times 3.32[b + 0.5(c - b)] \quad .$$

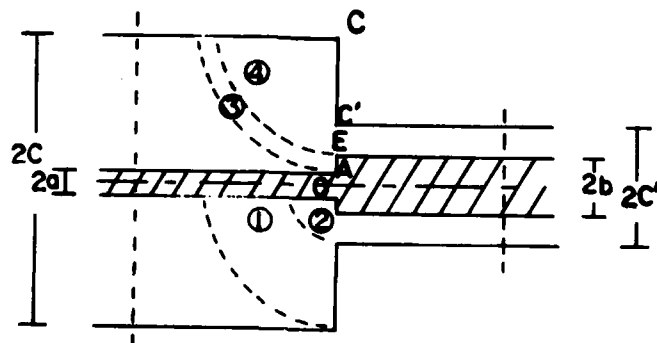


Figure A-8. Junction of dissimilar radii, $a < b$.

A.3 Example

Determine the capacitance between two coaxial cables that are connected in T-T as shown in Figure A-8. The sizes of the inner and outer conductors are:

$$\begin{aligned} a &= 0.038 \text{ cm (0.015") } , & b &= 0.05 \text{ cm (0.0201") } , \\ c &= 2.225 \text{ cm (0.876") } , & c' &= 0.168 \text{ cm (0.066") } . \end{aligned} \quad (29)$$

The four component capacitances are respectively:

$$\begin{aligned} C_1 &= \epsilon\epsilon_0 \times 4[a + \sqrt{(c-a)(c'-a)}] \ln \frac{c-a}{c'-a} \\ &= \epsilon\epsilon_0 \times 4[0.038 + \sqrt{(2.225 - 0.038)(0.168 - 0.038)}] \ln \frac{2.225 - 0.038}{0.168 - 0.038} \\ &= 0.0645 \epsilon\epsilon_0 , \end{aligned}$$

$$\begin{aligned} C_2 &= \epsilon\epsilon_0 \times 3.32[a + 0.5(c' - a)] \\ &= \epsilon\epsilon_0 \times 3.32[0.038 + 0.5(0.168 - 0.038)] \times 10^{-2} \\ &= 0.00342 \epsilon\epsilon_0 , \end{aligned}$$

$$\begin{aligned} C_3 &= \epsilon\epsilon_0 \times 4[c - \sqrt{(c-a)(c-b)}] \ln \frac{c-a}{c-b} \\ &= \epsilon\epsilon_0 \times 4[2.225 - \sqrt{(2.225 - 0.038)(2.225 - 0.05)}] \times 10^{-2} \\ &= 0.00001 \epsilon\epsilon_0 , \end{aligned}$$

$$\begin{aligned}
C_4 &= \epsilon\epsilon_0 \times 3.32[b + 0.5(c - b)] \\
&= \epsilon\epsilon_0 \times 3.32[0.05 + 0.5(2.225-0.05)] \times 10^{-2} \\
&= 0.0378 \epsilon\epsilon_0 .
\end{aligned}$$

The total capacitance for this junction is

$$\begin{aligned}
C &= C_1 + C_2 + C_3 + C_4 \\
&= 0.1057 \epsilon\epsilon_0 \\
&= 0.9358 \times 10^{-12} \text{ (F)} .
\end{aligned} \tag{30}$$

At the same time, the unit distributed capacitances of the two coaxial cables are

$$\begin{aligned}
\text{Cable 1: } C_{01} &= \frac{2\pi\epsilon\epsilon_0}{\ln \frac{R_2}{R_1}} = \frac{2\pi \times 8.85 \times 10^{-12} \times 1}{\ln \frac{2.225}{0.038}} \\
&= 13.666 \text{ pF/m} \\
&= 0.13666 \text{ pF/cm} .
\end{aligned} \tag{31}$$

$$\begin{aligned}
\text{Cable 2: } C_{02} &= \frac{2\pi \times 8.85 \times 10^{-12} \times 2.8}{\ln \frac{0.168}{0.05}} \\
&= 128.463 \text{ pF/m} \\
&= 1.28463 \text{ pF/cm} .
\end{aligned} \tag{32}$$

DISTRIBUTION LIST

DEPARTMENT OF DEFENSE

Assist to the Sec of Def, Atomic Energy
ATTN: Exec Assist

Defense Communications Engineer Ctr
ATTN: Code R123, Tech Lib
ATTN: Code R400
ATTN: Code R720, C. Stansberry

Defense Intell Agency
ATTN: DB 4C2, D. Spohn
ATTN: RTS-2A, Tech Lib
ATTN: RTS-2B

Defense Nuclear Agency
ATTN: RAEE
ATTN: RAEV
4 cys ATTN: STTI-CA

Defense Tech Info Ctr
12 cys ATTN: DD

Field Command, DNA, Det 2
Lawrence Livermore National Lab
ATTN: FC-1

Field Command, Defense Nuclear Agency
ATTN: FCLMC, F. Lehr
ATTN: FCPR
ATTN: FCTT
ATTN: FCTT, W. Summa
ATTN: FCTXE

Interservice Nuclear Weapons School
ATTN: TTV

Joint Chiefs of Staff
ATTN: J-3, Strat Opns Div

Joint Strat Tgt Planning Staff
ATTN: JLAA
ATTN: JLK, DNA Rep
ATTN: JLKS
ATTN: JPTM
2 cys ATTN: JPPFD

National Communications System
ATTN: NCS-TS

National Security Agency
ATTN: R-54, O. van Gunten

Under Sec of Def for Rsch & Engrg
ATTN: Strat & Space Sys (OS)

DEPARTMENT OF THE ARMY

BMD Systems Command
ATTN: BMDSC-AOLIB
ATTN: BMDSC-LEE, R. Webb

US Army Comm, Elect Command
ATTN: DRCPM-ATC
ATTN: DRDCO-SEI

DEPARTMENT OF THE ARMY (Continued)

Harry Diamond Laboratories
ATTN: DELHD-NW, J. Rosado, 20000
ATTN: DELHD-NW-E, 21000
ATTN: DELHD-NW-EA, 21100
ATTN: DELHD-NW-EB, 21200
ATTN: DELHD-NW-EC, 21300
ATTN: DELHD-NW-ED, 21400
ATTN: DELHD-NW-EE, 21500
ATTN: DELHD-R, 22000
ATTN: DELHD-TA-L, 81100, Tech Lib
ATTN: DELHD-TD, 00102
ATTN: DELHD-TF
ATTN: 00100, Commander/Tech Dir/Div Dir
ATTN: NWPO
2 cys ATTN: DELHD-NW-RC

US Army Armor Center
ATTN: Tech Lib

US Army Ballistic Research Lab
ATTN: DRDAR-BLB, W. van Antwerp
ATTN: DRDAR-BLE

US Army Comm-Elec Engrg Instal Agency
ATTN: CCC-CED-SES

US Army Communications Sys Agency
ATTN: CCM-AD-SV
ATTN: CCM-RD-T

US Army Electronics R&D Command
ATTN: DELSD-L, W. Werk

US Army Engineer Div, Huntsville
ATTN: HNDED-SR
ATTN: T. Bolt

US Army Info Systems Cmd
ATTN: AS-PLNS-S
ATTN: ATSI-CD-MD
ATTN: CC-OPS-OS

US Army Intel Threat Analysis Det
ATTN: Admin Officer

US Army Intell & Sec Cmd
ATTN: Tech Lib

US Army Materiel Sys Analysis Actvty
ATTN: DRXSY-PO

US Army Test & Eval Comd
ATTN: DRSTE-CM-F
ATTN: DRSTE-CT-C

US Army Training & Doctrine Comd
ATTN: ATCD-Z

US Army White Sands Missile Range
ATTN: STEWS-TE-N, K. Cummings

USA Missile Command
ATTN: Documents Section
ATTN: DRCPM-PE-EA, W. Wagner
ATTN: DRCPM-PE-EG, W. Johnson

DEPARTMENT OF THE NAVY

Naval Air Systems Command
ATTN: AIR 350F

Naval Ocean Systems Center
ATTN: Code C8, J. Rockway
ATTN: Code 54, C. Fletcher

Naval Ordnance Station
ATTN: Standardization Div

Naval Postgraduate School
ATTN: Code 1424, Library

Naval Research Laboratory
ATTN: Code 1434, E. Brancato
ATTN: Code 2627, D. Folen
ATTN: Code 4700, W. Ali
ATTN: Code 4701, I. Vitokovitsky
ATTN: Code 4760, R. Grieg
ATTN: Code 6623, R. Statler
ATTN: Code 6624

Naval Surface Weapons Center
ATTN: Code F30
ATTN: Code F32, E. Rathbun

Naval Surface Weapons Center
ATTN: Code F-56

Naval Weapons Center
ATTN: Code 343, FKA6A2, Tech Svcs

Naval Weapons Eval Facility
ATTN: Code AT-6

Ofc of Naval Research
ATTN: Code 427

Space & Naval Warfare Systems Cmd
ATTN: PME 117-21

Strategic Systems Programs
ATTN: NSP-2301, M. Meserole
ATTN: NSP-2342, R. Coleman
ATTN: NSP-2701
ATTN: NSP-27334
ATTN: NSP-43, Tech Lib

DEPARTMENT OF THE AIR FORCE

Aeronautical Systems Div
ATTN: ASD/ENSSA
ATTN: ASD/YYEF

Air Force Aeronautical Sys Div
ATTN: ASD/ENACE, J. Corbin

Air Force Institute of Technology
ATTN: ENA, G. Baker, D 58T

Air Force Weapons Laboratory
ATTN: NT
ATTN: NTAEE, C. Baum
ATTN: NTC, M. Schneider
ATTN: NTN
ATTN: NTYEP, W. Page
ATTN: SUL

DEPARTMENT OF THE AIR FORCE (Continued)

Air Logistics Command
ATTN: OO-ALC/MMEDO, L. Kidman
ATTN: OO-ALC/MMETH, P. Berthel

Air University Library
ATTN: AUL-LSE

Ballistic Missile Office/DAA
ATTN: ENSN
ATTN: ENSN, W. Clark
ATTN: ENSN, W. Wilson
ATTN: M. Stapanian

Electronic Systems Div
ATTN: SCS-1E

Foreign Technology Div
ATTN: NIIS, Library
ATTN: TQTD, B. Ballard

NORAD
ATTN: NORAD/J5YX

Rome Air Development Center
ATTN: TSLD

Sacramento Air Logistics Center
ATTN: MMCREB, F. Schrader
ATTN: MMIRA, J. Demes
ATTN: MMSREM, F. Spear

Space Division
ATTN: IND

Strategic Air Command
ATTN: DEMJE
ATTN: INAO
ATTN: NRI/STINFO
ATTN: XPFS
ATTN: XPQ

DEPARTMENT OF ENERGY

Department of Energy
Albuquerque Opns Office
ATTN: CTID
ATTN: WSSB

Emergency Electric Power Adm
US Dept of Energy
ATTN: L. O'Neill

University of California
Lawrence Livermore National Lab
ATTN: L-10, H. Kruger
ATTN: L-13, D. Meeker
ATTN: L-153, E. Miller
ATTN: L-156, H. Cabayan
ATTN: L-97, T. Donich
ATTN: Tech Info Dept Lib

Los Alamos National Laboratory
ATTN: B. Noel
ATTN: MS670, J. Malik

Sandia National Laboratories
ATTN: M. Morris
ATTN: Org 1231, C. Vittitoe
ATTN: Org 2322, E. Hartman

OTHER GOVERNMENT AGENCIES

Central Intell Agency
ATTN: OSWR/NED

Dept of Transportation, FAA
ATTN: Sec Div, ASE-300

Federal Emergency Management Agency
ATTN: OPIR, M. Murtha
ATTN: SL-EM, J. Hain

DEPARTMENT OF DEFENSE CONTRACTORS

Aerospace Corp
ATTN: I. Garfunkel
ATTN: J. Reinheimer
ATTN: Library

Agabian Associates
ATTN: Library

Allied Corp
ATTN: Dept 6401

Allied Corp
ATTN: M. Frank

Analytical Systems Engineering Corp
ATTN: M. Nucefora

AVCO Systems Division
ATTN: Library, A830

Battelle Memorial Institute
ATTN: E. Leach

BDM Corp
ATTN: Corp Lib
ATTN: S. Clark
ATTN: W. Sweeney

BDM Corp
ATTN: Library

Boeing Aerospace Co
ATTN: M. Anaya, M/S 2A-87

Boeing Co
ATTN: D. Kemle
ATTN: H. Wicklein
ATTN: J. Dicome, Org 2-3744, M/S 47-36
ATTN: Kent Tech Lib

Boeing Mil Airplane Co
ATTN: C. Sutter

Booz-Allen & Hamilton, Inc
ATTN: R. Chrisner
ATTN: Tech Lib

Calspan Corp
ATTN: R. Thompson

Calspan Corp
ATTN: Library

Charles Stark Draper Lab, Inc
ATTN: K. Fertig
ATTN: TIC, MS 74

DEPARTMENT OF DEFENSE CONTRACTORS (Continued)

Cincinnati Electronics Corp
ATTN: L. Hammond

Computer Sciences Corp
ATTN: A. Schiff

Dikewood Corp
ATTN: Tech Lib for C. Jones
ATTN: Tech Lib for D. Pirio
ATTN: Tech Lib

Dikewood Corp
ATTN: K. Lee

E-Systems, Inc
ATTN: J. Moore

Eaton Corp
ATTN: E. Karpen

EG&G Wash Analytical Svcs Ctr, Inc
ATTN: C. Giles

Electro-Magnetic Applications, Inc
ATTN: D. Merewether

Ford Aerospace & Communications Corp
ATTN: H. Linder

General Dynamics Corp
ATTN: Rsch Lib

General Dynamics Corp
ATTN: Rsch Lib

General Electric Co
ATTN: D. Nepveux
ATTN: J. Peden

General Electric Co
ATTN: C. Hewison

General Electric Co
ATTN: Tech Lib

General Research Corp
3 cys ATTN: Tech Info Ofc

Georgia Institute of Technology
ATTN: Res & Sec, Coord for H. Denny

Grumman Aerospace Corp
ATTN: L-01 35

GTE Communications Products Corp
ATTN: A. Novenski
ATTN: A. Murphy
ATTN: D. Flood
ATTN: J. Waldron
ATTN: M. Snow

GTE Government Systems Corp
ATTN: L. Lesinski

Harris Corp
ATTN: V Pres & Mgr Prgms Div

Hazeltine Corp
ATTN: J. O'Krent

DEPARTMENT OF DEFENSE CONTRACTORS (Continued)

Honeywell, Inc
ATTN: R. Johnson
ATTN: S&RC, Lib

Honeywell, Inc
ATTN: S. Graff
ATTN: W. Stewart

Horizons Technology, Inc
ATTN: R. Kruger

Hughes Aircraft Co
ATTN: CTDC 6/E110
ATTN: K. Walker

Hughes Aircraft Intl Svc Co
ATTN: A. Narevsky, S32/C332

IIT Research Institute
ATTN: Acoat

IIT Research Institute
ATTN: I. Mindel
ATTN: J. Bridges

Institute for Defense Analyses
ATTN: Tech Info Services

IRT Corp
ATTN: B. Williams
ATTN: N. Rudie

IRT Corp
ATTN: J. Klebers

JAYCOR
ATTN: D. Higgins

JAYCOR
ATTN: E. Wenaas
ATTN: R. Stahl

JAYCOR
ATTN: Library

Kaman Sciences Corp
ATTN: A. Bridges
ATTN: F. Shelton
ATTN: N. Beauchamp
ATTN: W. Rich

Kaman Sciences Corp
ATTN: E. Conrad

Kaman Tempo
ATTN: DASIAC
ATTN: R. Rutherford
ATTN: W. Hobbs, Jr
ATTN: W. McNamara

Kaman Tempo
ATTN: DASIAC

Litton Systems, Inc
ATTN: MS 64-61, E. Eustis

Litton Systems, Inc
ATTN: J. Skaggs

DEPARTMENT OF DEFENSE CONTRACTORS (Continued)

Lockheed Missiles & Space Co, Inc
ATTN: Tech Info Ctr

Lockheed Missiles & Space Co, Inc
ATTN: B. Kimura
ATTN: D. Nishida, Dept 85-76
ATTN: H. Thayn
ATTN: L. Rossi
ATTN: S. Taimuty, Dept 81-74/154

LuTech, Inc
ATTN: F. Tesche

Martin Marietta Corp
ATTN: J. Casalese
2 cys ATTN: M. Griffith

McDonnell Douglas Corp
ATTN: T. Ender

McDonnell Douglas Corp
ATTN: S. Schneider

McDonnell Douglas Corp
ATTN: M. Potter
ATTN: R. Twomey, MS/36-43

The University of Michigan
2 cys ATTN: Valdis Liepa

Mission Research Corp
ATTN: EMP Gp
ATTN: J. Gilbert
ATTN: W. Crevier
2 cys ATTN: C. Longmire

Mission Research Corp
ATTN: A. Chodorow
ATTN: D. Gardner
ATTN: M. Scales

Mission Research Corp
ATTN: J. Lubell
ATTN: R. Curry
ATTN: W. Stark
ATTN: W. Ware

Mission Research Corp, San Diego
ATTN: J. Erier
ATTN: V. van Lint

Mitre Corp
ATTN: M. Fitzgerald

Norden Systems, Inc
ATTN: Tech Lib

Northrop Corp
ATTN: RAD Effects Grp

Pacific-Sierra Research Corp
ATTN: H. Brode, Chairman SAGE
ATTN: L. Schlessinger

Physics International Co
ATTN: Doc Control

DEPARTMENT OF DEFENSE CONTRACTORS (Continued)

R&D Associates

ATTN: C. Knowles
ATTN: C. Mo
ATTN: Doc Control
ATTN: M. Grover
ATTN: W. Karzas

R&D Associates

ATTN: W. Graham

Rand Corp

ATTN: B. Bennett

Raytheon Co

ATTN: G. Joshi

Raytheon Co

ATTN: H. Flescher

RCA Corp

ATTN: G. Brucker

Rockwell International Corp

ATTN: D/277-060, 031-BB17
ATTN: J. Burson
ATTN: J. Erb

Rockwell International Corp

ATTN: B. White

Rockwell International Corp

ATTN: B-1 Div, TIC, EAOE

Rockwell International Corp

ATTN: F. Shaw

S-CUBED

ATTN: A. Wilson

Sanders Associates, Inc

ATTN: R. Despathy

Science & Engrg Associates, Inc

ATTN: V. Jones

DEPARTMENT OF DEFENSE CONTRACTORS (Continued)

Science Applications Intl Corp
ATTN: W. Chadsey

Singer Co

ATTN: Tech Info Ctr

Sperry Corp

ATTN: M. Cort

Sperry Corp

ATTN: Tech Lib

Sperry Corp

ATTN: D. Schow

SRI International

ATTN: A. Whitson
ATTN: E. Vance

Teledyne Brown Engineering

ATTN: F. Leopard
ATTN: J. Whitt

Texas Instruments, Inc

ATTN: D. Manus
ATTN: Tech Lib

Transients Limited Corp

ATTN: D. Clark

TRW Electronics & Defense Sector

ATTN: H. Holloway
ATTN: L. Magnolia
ATTN: O. Adams
ATTN: R. Plebuch
ATTN: W. Gargaro

United Technologies Corp

ATTN: Chief, Elec Design

END

Dtlic

5-86